SYNTHESIS OPTIMIZATION OF AURIVILLIUS PHASES

BY

MYLES S. PETERSON II

A THESIS
SUBMITTED TO THE FACULTY OF

ALFRED UNIVERSITY

IN PARTIAL FULFILLMENT OF THE REQUIREMENTS
FOR THE DEGREE OF

MASTER OF SCIENCE

IN

MATERIALS SCIENCE AND ENGINEERING

ALFRED, NEW YORK

APRIL, 2003

SYNTHESIS OPTIMIZATION OF AURIVILLIUS PHASES

BY

MYLES S. PETERSON II

B.S. ALFRED UNIVERSITY (2001)

B.A. ALFRED UNIVERSITY (2001)

SIGNATURE OF AUTHOR (Signature on file)

APPROVED BY (Signature on file)
SCOTT MISTURE, ADVISOR

(Signature on file)
WILLIAM M. CARTY, ADVISORY COMMITTEE

(Signature on file)
WALTER A. SCHULZE, ADVISORY COMMITTEE

(Signature on file)
ALASTAIR CORMACK, CHAIR, ORAL THESIS DEFENSE

ACCEPTED BY (Signature on file)
RONALD S. GORDON, DEAN,
SCHOOL OF CERAMIC ENGINEERING
AND MATERIALS SCIENCE

Acknowledgments

First, I would like to acknowledge Fran Williams, Slawomir (Swavek) Zdzieszynski, and Ward Votava for the answers to the innumerable questions that I have had. Next, I want to acknowledge Scott Misture and my thesis committee for valuable insight on this work. My research colleagues that deserve credit include: Scott Speakman, Mike Haluska, Chris Say, Viral Modi, Michael "Mick" Dolan, Brian Luisi, Yuandan Liu, Steve Harvey, and Justin Packard. Through our conversations about research and life, we've all learned a tremendous amount, and for that I'm grateful.

I would like to thank Chris Say and Mike Haluska for assistance with D-Optimal Design and Rietveld analysis respectively. A special thanks to Mike Haluska, Michael "Mick" Dolan, and Melissa Them for reading this thesis, and providing thoughtful and insightful feedback. Heidi Schulze deserves recognition for going far above the average in polishing samples and asking questions. I thank the riding crew for encouraging me to go harder and faster than I ever thought I could, on the bike, and in life. D. Mark DeLaitsch thanks for always giving me the artist's perspective on things- more engineers should listen to you.

I need to thank Eric Telfeyan and Melissa Them for always being my best friends. Finally, without the support of my family I would have never made it through this "long strange trip"-thank you, and I love you all…may the powder always be deep and the wind always be at your back.

Table of Contents

List of Tables

page

List of Figures

page

Abstract

The solid state processing, sintering behavior and conductivity of the $Bi_2Sr_2Nb_2TiO_{12}$ Aurivillius phase were studied. The solid-state processing steps were investigated using X-ray powder diffraction (XRD). The in-situ formation of $Bi_2Sr_2Nb_2TiO_{12}$ was measured using high temperature X-ray powder diffraction (HTXRD). $Bi_2Sr_2Nb_2TiO_{12}$, $SrTiO_3$, two and four-layer Aurivillius phases formed with this in-situ technique.

Rietveld refinement was used to characterize the Aurivillius unit cell, and to model four-layer Aurivillius impurities. A weighted residual of 0.14 and a χ^2 of 4.5 was obtained. The refined lattice parameters for $Bi_2Sr_2Nb_2TiO_{12}$ were a=3.8927(7) Å, and c=33.1960(9) Å for a body centered tetragonal unit cell with the I4/mmm space group. Rietveld refinement was used to confirm the unit cell of the δ-Bi_2O_3 present in certain samples. The refined lattice parameter for the δ-Bi_2O_3 was a = 5.5747(4) Å with a cubic crystal system and a space group of Fm-3m.

A designed statistical study on density and affect of the sintering accelerator Bi_2O_3 was completed. The model had an R^2 of 0.93 and a $S_{y.x}$ of 0.33, and suggested that an optimum sintering temperature was ~1060°C with approximately four weight percent Bi_2O_3 added to the Aurivillius phase. The scanning electron microscope (SEM) and energy dispersion spectroscopy (EDS) were used to investigate the microstructure and identify secondary phases when necessary. The conductivity of $Bi_2Sr_2Nb_2TiO_{12}$ and samples with Bi_2O_3 added to the Aurivillius phase were explored using impedance spectroscopy (IS). The addition of Bi_2O_3 greatly enhanced the conductivity values of the $Bi_2Sr_2Nb_2TiO_{12}$ to the magnitude of the current ionic conductor standard, yittria stabilized zirconia.

1. Introduction and Review

1.1 Research goals

Aurivillius phases possess great potential as electrically active materials for a variety of electrochemical and ferroelectric applications. High quality phase pure precursor powders are required for the development of internal circuits, ferroelectric thin films, and electrochemical membranes. The goal of this research was to understand the synthesis of the Aurivillius phase $Bi_2Sr_2Nb_2TiO_{12}$ in the broadest of terms. This body of work can be applied to other Aurivillius phases and families so that future researchers may avoid some of the potential pitfalls of working with this system.

The concept of synthesis can be divided into two categories. The first category includes the chemical evolution of the phase. How do the precursor powders chemically transform throughout the synthesis process to yield the Aurivillius phase? Is the phase actually pure, and can the solid-state kinetics be determined? The second category of synthesis is the sintering stage of the Aurivillius phase. In order to accurately assess the electrical properties of the material, a dense sample is needed. Yet, what variables promote densification? Can other materials be added to the phase to aid in sintering? How does densification affect conductivity?

This first chapter includes an introduction to the research, followed by the background and principles of fuel cells. Next, a detailed description of the Aurivillius phase and its processing techniques are shown. The tunable electrochemical nature of the Aurivillius phase will then be described, as well as the importance of sintering, and the use of sintering aids. The second chapter covers experimental details and the characterization tools utilized during this study. The third chapter addresses the results of the research, followed by reasons for abnormalities. The fourth chapter is a synopsis of the research and a review of its major findings. The final chapter includes areas of additional exploration, and concluding remarks.

1.2 Global Economic Prosperity and Energy

The subject of energy is one that is relevant in all of our lives. It is a critical factor in global economic prosperity and the well being of our society. The earth's fossil fuels, however, are slowly, yet consistently being depleted. The air is becoming laden with pollutants as a consequence of burning mass amounts of hydrocarbons. There has been a worldwide drive toward solving the future energy problem over the last few decades, which has enabled a market for a variety of electrochemical-energy conversion and storage devices. There are a number of options that come to the forefront of the energy discussion. Solar energy and wind-powered energy have been explored for years, but the amount of energy produced is inadequate. The future of the energy market includes high-energy secondary batteries and certain types of fuel cells.[1]

1.3 Fuel Cell Theory

This research focuses on the electrolyte material to be used within a fuel cell. It is important to understand how a fuel cell works to appreciate the level of complexity that scientists and engineers face in designing fuel cells. A fuel cell is an energy conversion device that produces electricity by an electrochemical combination.[2] There are three basic components of a fuel cell: an anode, a cathode, and an electrolyte (Figure 1.1). A fuel (e.g., hydrogen) is fed to the anode where it is oxidized, electrons are stripped off, and they are released to the circuit. Next, an oxidant (e.g., oxygen) is fed to the cathode where it is reduced, electrons are accepted from the external circuit, and direct-current electricity flows from the anode to the cathode.[2]

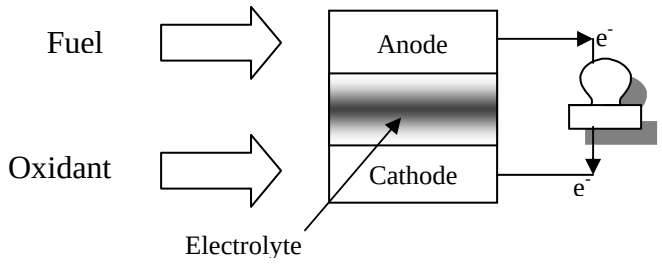

Figure 1.1 Schematic diagram of a fuel cell.

Since the inherent Carnot-cycle limitations associated with heat engines are absent, fuel cells can, in principle, convert chemical energy into electrical power very efficiently; but in practice the conversion rarely exceeds 55-60% unless pure hydrogen is used as a fuel.[1] Nonetheless, compared with conventional methods of power generation, fuel cells offer several advantages including high efficiency, reliability, modularity, fuel adaptability, and low levels of NO_x and SO_x emissions.[3]

1.3.1 Historical Perspective

In 1839, Sir William Grove reported the first operation of a basic fuel cell using sulphuric acid as the electrolyte.[4] Actual ceramic fuel cells did not come about until 1899 when Nernst reported solid-oxide electrolytes.[5] His research focused on ceramic oxide filaments for electric lamps, initially using oxides such as lime and magnesia, and then a mixture of yttria and zirconia. By 1937, Baur and Preis operated the first ceramic fuel cell, a tubular solid oxide fuel cell (SOFC) that operated at 1000°C.[6] Since then, research has investigated many different types of materials and their ability to conduct ions. The search for materials that have a large oxygen ion conductivity at low temperatures is an area of intense activity.[7] One of the most successful materials for an electrolyte is yttria-stabilized zirconia (YSZ). It has been used in multi-kilowatt fuel cells for thousands of hours, but must be operated near 1000°C.[8] The YSZ is a benchmark to which most current electrolytes are compared. There are some Aurivillius families that have "better" properties than YSZ, and they will be discussed shortly.

1.3.2 Types of Fuel Cells

There are five major families of fuel cells, including proton exchange membrane fuel cells, phosphoric acid fuel cells, solid oxide fuel cells, molten carbonate fuel cells, and alkaline fuel cells. Practically speaking, fuel cells cannot be operated as single units; rather they are connected in an electrical series to build voltage. This series of cells is referred to as a stack.[2] It is important to understand that some designs are better for certain applications than others. For example, solid oxide fuel cells operate at very high temperatures, and proton exchange membrane fuel cells utilize very expensive electrodes. Molten carbonate fuel cells and alkaline fuel cells will not be discussed here, but the interested reader is pointed towards several informative references.[9,10]

The proton exchange membrane fuel cell (PEFC) has a higher power density than any other fuel cell system. It uses a solid polymer electrolyte (with a fluorocarbon backbone) solving many problems that plague other fuel cells: it operates at a temperature of about 80°C (instant start-up and no thermal shielding), there is no corrosion, and fewer safety concerns. The membrane is actually an electronic insulator, yet it conducts hydrogen ions. Hydrogen is consumed at the anode, causing ions to enter the electrolyte. The cathode reaction consists of oxygen combining with the electrons from the cathode and the hydrogen ions creating water.

A second type of fuel cell is the phosphoric acid fuel cell (PAFC), which runs at temperatures of approximately 200°C. It uses liquid phosphoric acid as the electrolyte contained in a polytetrafluoroethylene bonded silicon carbide matrix. The fuel and oxidant are supplied to porous electrodes and conduct electrons from the anode to the cathode. The water by-product is removed from the cathode, typically in the form of steam.

The fuel cell of interest for this research is the solid oxide fuel cell (SOFC). There are a variety of different designs of the SOFC including planar and tubular geometries. These fuel cells use a ceramic solid electrolyte at elevated temperatures of approximately 1000°C. Yet, research by Doshi and Richards[11] suggests that some electrolytes, such as doped ceria electrolytes, can feasibly operate at 500°C. The major criterion for the electrolyte is that it must be an excellent conductor of negatively charged

oxygen ions at high temperatures. Electrolytes including fluorite-structured oxide materials such as YSZ, rare earth doped ceria, and rare earth doped bismuth oxide have been widely researched.[3] YSZ has been very successful because the yttrium oxide dopant stabilizes the high temperature cubic phase in zirconia and generates oxygen vacancies.

The anode of a SOFC is usually made out of nickel/zirconia cermet, and the cathode is magnesium-doped lanthanum manganate. The anode is stable in the reducing environment of the fuel, electronically conducting, and has sufficient porosity to allow the transport of the fuel and products away from the electrolyte/fuel electrode interface.[3] There are a number of different reactions that can occur depending upon the fuel[2,3]:

$$O^{2-}(s) + H_2(g) \rightarrow H_2O(g) + 2e^- \quad (1)$$

$$CO + O^{2-} \rightarrow CO_2 + 2e^- \quad (2)$$

At the anode, a gas such as hydrogen or carbon monoxide is reacted with oxide ions from the electrolyte to produce either H_2O or CO_2. The electrons from this reaction move from the anode to the electrical load. Next, the electrons go back to the cathode where oxygen from air is converted into ions, which go back into the electrolyte. The cathode, commonly called the air electrode, operates in an oxidizing environment. The oxygen in the gas phase is reduced to oxide ions per the following reaction:[3]

$$\tfrac{1}{2} O_2(g) + 2e^- \rightarrow O^{2-}(s) \quad (3)$$

The cathode also has a variety of parameters that it must meet. These include: electronic conductivity, stability, adequate thermal expansion, minimal reactivity, and sufficient porosity.[3] Figure 1.2 shows a schematic of all of the reactions that take place in a SOFC.

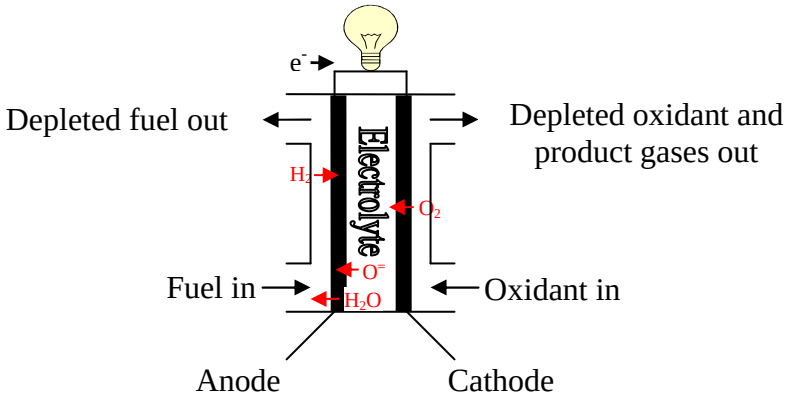

Figure 1.2 Schematic of a SOFC including chemical reactions.

1.3.3 Fuel Cell Comparison

It is important to realize that all fuel cells rely on the same operating principles. An input fuel is reacted in order to strip electrons, and these electrons create an electric current. In the electrode, ions recombine to create by-products such as water or CO_2. Table 1-I shows a comparison of some of the major types of fuel cells. It has been demonstrated that many different chemical reactions can occur depending upon the fuel used and the different materials used in the fuel cell. The inefficiency of fuel cells is caused by two major problems, (1) at low currents an over potential is necessary to drive the electrode reactions away from equilibrium, and (2) at high currents the effects of ionic and electronic resistance increases the mass transport limitations in the electrodes reduce the output voltage to zero.[12]

Table 1-I Comparison of Some of the Different Types of Fuel Cells[1]

Fuel Cell	PAFC	MCFC	SOFC	PEMFC
Electrolyte	Phosphoric Acid	Molten Carbonate	Ceramic	Polymer
Operating Temperature	200°C	650°C	900-1000°C	60-100°C
Fuels	H_2 / Reformate	H_2/CO/ Reformate	H_2/CO_2/CH_4 Reformate	H_2 / Reformate

1.4 The Aurivillius Phase

In 1949 and 1950, three groundbreaking papers were written by Bengt Aurivillius.[13-15] These papers explored the discovery of a group of metal oxides having

bismuth oxide layers alternating with perovskite structure layers with the general composition $Bi_2A_{n-1}B_nO_{3n+3}$ (where A=Ca, Sr, Ba, Pb, Bi, Na, K, and B=Ti, Nb, Ta, Mo, W, Fe). Here the "A" can be mono-, di-, or trivalent ions, or a mixture there of. These Aurivillius phases are composed of two structural elements, the $Bi_2O_2^{2+}$ sheets, which are interleaved by perovskite-type blocks $(A_{n-1}B_nO_{3n+1})^{2-}$ of variable thickness according to the integer of n (n = 0,1,2,3,4,5) leading to a typical "mica-like" structure.[16] Because of their ionic structural framework, Aurivillius phases exhibit a great variability with respect to metal cation substitution; therefore, these phases have high potential for systematic property control.[17] Originally, Aurivillius phases were of interest for their ferroelectric properties, but now Aurivillius phase materials are very important for several applications including: ferroelectric, piezoelectric, microelectromechanical (MEM) devices, and as tunable dielectric materials.[18] Also, a wide array of sensors such as: bulk conductivity, boundary conductivity, emf, and acceleration sensors can be utilized by fast ion conductors.[19]

1.4.1 Crystal Structure of the Aurivillius Phase

In order to understand the crystal structure of an Aurivillius phase, it is important to understand what a perovskite structure is. The perovskite structure is probably the simplest example of a structure containing two different cations (Figure 1.3).[20] The different ions are in the form ABO_3. The A and B atoms represent +2 and +4 ions, respectively, and the O atom is the oxygen ion. This structure can be thought of as a primitive cubic lattice. The A atoms are at the corners, the O atoms are on the faces, and the B atoms are at the center.

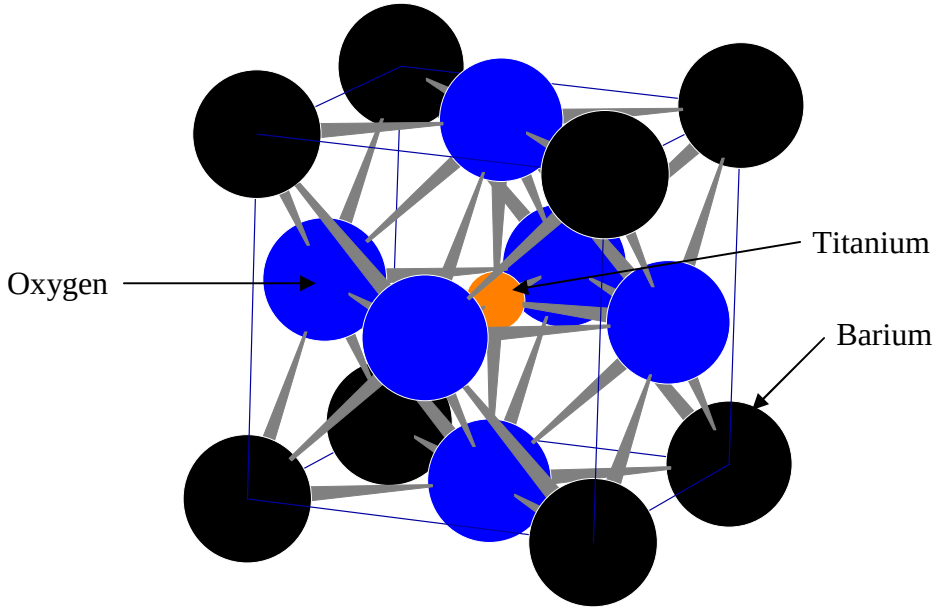

Figure 1.3 Idealized view of barium titanate ($BaTiO_3$) with its perovskite structure.

The Aurivillius phase contains multiples (one to five) of the perovskite structures in between blocks or layers of bismuth oxide $(Bi_2O_2)^{2+}$. Figure 1.4 illustrates an Aurivillius structure ($Bi_2Sr_2Nb_2TiO_{12}$) with three perovskite layers squeezed in between two bismuth-oxide layers. This structure can accommodate a wide range of cations. This is crucial when trying to introduce oxygen vacancies. In their pure form and at equilibrium conditions, many perovskite-derived materials contain ordered oxygen vacancies which lead to fast ion conduction.[21] But it is not only the creation of vacancies that is a challenge, it is also the temperature at which the conduction occurs. An oxide-ion electrolyte capable of supporting oxide–ion conductivities in excess of $10^{-2}\ \Omega^{-1}\ cm^{-1}$ at temperatures below 700 °C has remained a frustratingly elusive target of considerable commercial interest.[22] Thus far, there has been a general description of conductivity, and later there will be a more detailed description of oxygen ionic conductivity.

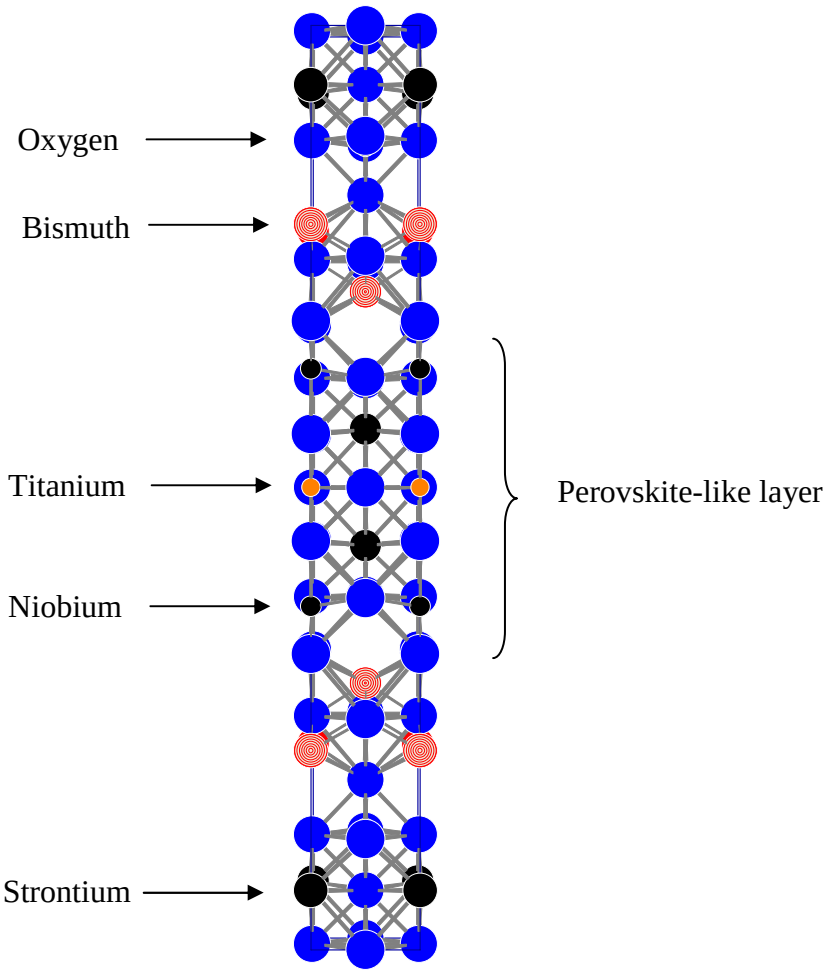

Figure 1.4 Illustration of $Bi_2Sr_2Nb_2TiO_{12}$.

1.4.2 Aurivillius Synthesis

There are multiple ways that Aurivillius phases can be synthesized. The first reaction entails a solid-state reaction. In solid-state synthesis, a stoichiometric mixture of oxides and carbonates are pressed into pellets and reacted at high temperatures. Next, the pellets are sintered at high temperatures for several days with frequent grinding and repressing to achieve phase purity. The phase purity is checked via X-ray diffraction techniques. A variety of milling techniques can be used before the synthesis in order to get full homogeneity. The proper choice of the experimental conditions applied, such as the isostatic pressure and the sintering temperature depend upon the system under study.

In order to choose the proper temperature for solid-state reaction synthesis two criteria should be taken into account: (1) the powders should completely react; (2) the process of the synthesis reaction should be separated from the process of sintering.[23] The synthesis reaction should take place at the highest temperature possible that is below the melting temperature. The pressure that is needed to form the pellets is one that creates green pellets of sufficient density. Research indicates that for BICUVOX ($Bi_2V_{0.90}Cu_{0.10}O_{5.35}$) systems, the final density of the sintered pellet does not depend on the pressure applied to the green material.[23] Rather, the pressure is important when the solid-state diffusion process dictates the sintering. If liquid phase sintering is taking place, then the density of the sintered material should not be strongly affected by the degree to which the powder was compacted during pressing.[23]

Another Aurivillius synthesis method that is becoming more popular is the Pechini[24] method. This method has several advantages over the typical preparation methods. First, stoichiometry can be adjusted very accurately, which is important when one is trying to achieve phase pure samples. Second, it creates very fine-grained powders that can be well-pressed. Third, mechanically stable samples are required for good diffusion to take place. Finally, and most importantly, the main advantage is the atomic distribution of cations in the whole product.[25] Interested readers are directed toward the literature of Schulz and Udawatte for a full detail of the chemistry and procedures that take place utilizing this method.[25,26] One of the major disadvantages of the Pechini method is that it is a complicated chemical synthesis, where careful monitoring of temperature is crucial for completion.

A third method to synthesize Aurivillius phases utilizes a combination of molten salts.[9] In this procedure the reagent oxides are mixed with NaCl and KCl. The mixture is washed, then heated into pellets at ~1100 °C, and subsequently ground and pressed for sintering. Another method entails the use of hydrothermal synthesis.[16] Here, various starting reagents are mixed with deionized water and stirred under high temperatures and pressures for 2 days. After cooling, the product is filtered, washed, and dried. A final method uses a polymerized complex. Here the basic idea is to reduce the segregation of different metal ions during precipitation, decomposition and pyrolysis, which can be achieved by forming stable metal-chelate complex followed by increasing

polymerization.[26] There has been some recent work that suggests that different synthetic approaches may give rise to particular properties due to possible variation of surface morphology.[16] In reality, there is no correct synthesis route, but rather a balance of facilities, time, supply, etcetera.

1.4.2.1 Phase relationships

To date there has been no research on the phase relationships of the Aurivillius phase $Bi_2Sr_2Nb_2TiO_{12}$. This is due to the multiple precursor materials and the complicated solid state chemistry that yields $Bi_2Sr_2Nb_2TiO_{12}$. Portions of the solid state chemistry can be exposed using binary phase diagrams. The results will show some of the basic phase transformations and begin to map out the formation of $Bi_2Sr_2Nb_2TiO_{12}$ using high temperature X-ray diffraction (HTXRD).

The high T_c superconductivity community has done some research on various phases in an effort to better understand the processing. One example is the monoclinic perovskite $Sr_{3.94}Ca_{1.31}Bi_{2.70}O_{12}$.[27] Also, there has been considerable thin film work in the area of ferroelectric random-access memories (FeRAMs) of strontium bismuth tantalite. Phase diagrams were determined as a function of the crystallization temperature for varying Sr or Bi contents.[28] In order to study the crystallization process of metalorganic chemical vapor deposition (MOCVD) thin films, and to identify the optimum film compositions for low fabrication temperatures, the phase diagrams are crucial. For further phase investigation of the Aurivillius phase, this also holds true.

1.4.3 Oxygen-Ion Conduction

The ideal electrolyte in SOFC conducts ions at relatively low temperatures. In solid-state oxide ion conduction, vacancy hopping is the most common transport mechanism, and consequently, most materials studied contain oxygen vacancies.[29] There are really two classes of ionic conductivity. The first contains intrinsic oxygen vacancies (e.g. $Bi_2VO_{5.5}$), and the second are those containing extrinsic oxygen vacancies (e.g.,

$Bi_2Sr_2Nb_2AlO_{11.5}$) that are introduced by doping into either the perovskite or bismuth oxide layer.[8]

There are a variety of different materials that have been researched for oxygen vacancies. One such class of material is the bismuth vanadium system (BIMEVOX).[23,30] These compounds are characterized by the formula $Bi_2V_{1-x}Me_xO_{5.5-3x/2}$ ($0 \leq x \leq 1$), where Me is a metal such as Cu, Ni, etc. The BIMEVOX systems have had some of the highest ionic conductivities reported.[8] Another material system that has had a lot of attention is the bismuth titanates ($Bi_4Ti_3O_{12}$).[31-33] These have had extensive study because of their piezoelectric properties.

The following is a mathematical description of what is needed for a good O^{2-}-ion conductor. First, it ideally has a transport number of

$$t_o = \sigma_o / \sigma_t \approx 1 \tag{4}$$

where σ_o is the O^{2-} ion conductivity, and σ_t is the total conductivity, including any electronic conductivity. The ionic conductivity σ_o varies sensitively with temperature as

$$\sigma_o = \left(\frac{A}{T}\right)\exp(-E_a / kT) \tag{5}$$

where A and E_a are the pre-exponential factor and the activation energy respectively.[34] One of the goals in making a highly conductive oxide-ion material is to maintain a high pre-exponential factor A, while minimizing the activation energy. In equation (6), ΔH_m is the motional enthalpy and ΔH_t is the attractive enthalpy between the dopant and the mobile ionic species.

$$E_a = \Delta H_m + \frac{1}{2}\Delta H_t \tag{6}$$

Goodenough and colleagues have developed a successful strategy for the design of a fast O^{2-} ion electrolytes:[34]

- Selection of a structure that permits a low motional enthalpy
- A doping mechanism (if needed) that creates mobile vacancies or interstitials, minimizing the attractive enthalpy between the dopant and the mobile ionic species.

The general target of SOFC electrolytes is a material with an ionic conductivity of σ_o>0.1 S cm^{-1} with electronic transference number <10^{-3}.[21] It is clear from wide potential uses of these oxygen ion conductors that materials that conduct oxygen ions, and materials that sustain mixed electronic and ionic conduction, will provide an integral link to the future of some electrochemical devices. In summary, Table 1-II shows the conductivity of various Aurivillius phases. An inherent weakness of the conductivity data of Aurivillius phases in the literature is that there is often no compensation for density. A simple plot can be made showing an exponential increase in conductivity as density is increased. This research will address the density problem and normalize results so that they can be compared.

Table 1-II Conductivity Data* for Various Aurivillius Phases[35]

	Conductivity (S/cm)		Activation Energy	Density
Aurivillius Phase	900°C	800°C	(eV)	(% theoretical)
$Bi_2Sr_2Nb_2AlO_{11.5}$	$2.3*10^{-2}$	$1.2*10^{-2}$	1.26	87
$Bi_2Sr_2Nb_2GaO_{11.5}$	$3.6*10^{-2}$	$2.0*10^{-2}$	1.28	93
$Bi_2Sr_2Nb_2TiO_{12}$	$1.4*10^{-4}$	$2.5*10^{-5}$	1.91	70
$Bi_2Sr_2Ta_2AlO_{11.5}$	$9.2*10^{-4}$	$4.8*10^{-4}$	1.42	68
$Bi_2Sr_2Ta_2GaO_{11.5}$	$1.3*10^{-2}$	$9.3*10^{-3}$	1.23	88
$Bi_2Sr_2Ta_2TiO_{12}$	$1.8*10^{-5}$	$3.0*10^{-6}$	1.94	62

*Conductivity, activation energy, and percent of theoretical density of $Bi_2Sr_2M'_2M''O_{11.5}$ and $Bi_2Sr_2M'_2TiO_{12}$ (M'=Nb, Ta, and M"=Al, Ga). Activation energy values for oxygen-deficient materials were calculated using the linear portion of Arrhenius plots at low temperatures.

1.5 Conductivity Measurement

1.5.1 Impedance Spectroscopy

Electrochemical impedance spectroscopy (EIS or IS) is a very powerful non-destructive method employed to measure the electrical properties of a variety of systems. These systems can vary from ceramics to polymers; the only necessary trait is that the system of interest must be able to conduct current. It may be used to investigate the dynamics of bound or mobile charge in the bulk or interfacial regions of any kind of solid or liquid material: ionic, semiconducting, mixed electronic-ionic, and even insulators (dielectrics).[36] A particular advantage of EIS is that it can give very detailed information about individual reactions that are taking place in a system. The power of the technique lies in its ability to differentiate between effects which are due to solution resistance, electrodes, contact resistance, charge transfer impedance, and diffusional effects.[37] This is of particular interest when there is an advantage to resolving the electrical responses of various microstructural regions (e.g. electrode, grain boundaries, bulk).[38] Determining which element of the microstructure corresponds to certain EIS features is the challenge. Yet, the identification of the most appropriate equivalent circuit to represent the electrical properties of a material is absolutely essential as a step toward a proper understanding of its properties.[39]

The general EIS experiment involves applying an electrical stimulus (a known voltage or current) to the electrodes and observing the response (the resulting current or voltage).[36] The most common and standard approach measures impedance directly in the frequency domain. A single-frequency voltage is applied to the sample, and the phase shift and amplitude are measured, essentially measuring the real and imaginary parts of the resulting current at that frequency. The signal and the resulting current can be found in Equations 7 and 8. Equation 9 shows the single frequency.

$$v(t) = V_m \sin(\omega t) \tag{7}$$

$$i(t) = I_m \sin(\omega t + \theta) \tag{8}$$

$$\nu \equiv \frac{\omega}{2\pi} \tag{9}$$

Where ω is frequency, v is voltage, V_m is maximum voltage, t is time, i is current, I_m is maximum current, and θ is the phase difference between the voltage and the current. When the frequency is zero, it has purely resistive behavior. Conventional impedance can be found in Equation 10, and the magnitude or modulus is Equation 11. The phase angle is $\theta(\omega)$.[36] The real and imaginary components in the right-hand coordinate vector system ($Z = a + jb$ or $Z(\omega) = Z' + jZ''$) determine the magnitude and direction of the impedance.[36] When impedance is plotted with rectangular coordinates the values can be found in Equation 12 and 13. The phase angle is shown in Equation 14. Finally, the modulus can be written as Equation 15.[36] Figure 1.5 shows impedance $|Z|$ plotted as a planar vector.

$$Z(\omega) \equiv v(t)/i(t) \tag{10}$$

$$|Z(\omega)| = \frac{V_m}{I_m(\omega)} \tag{11}$$

$$Z' = |Z|\cos(\theta) \tag{12}$$

$$Z'' = |Z|\sin(\theta) \tag{13}$$

$$\theta = \tan^{-1}\left(\frac{Z''}{Z'}\right) \tag{14}$$

$$|Z| = \left[(Z')^2 + (Z'')^2\right]^{1/2} \tag{15}$$

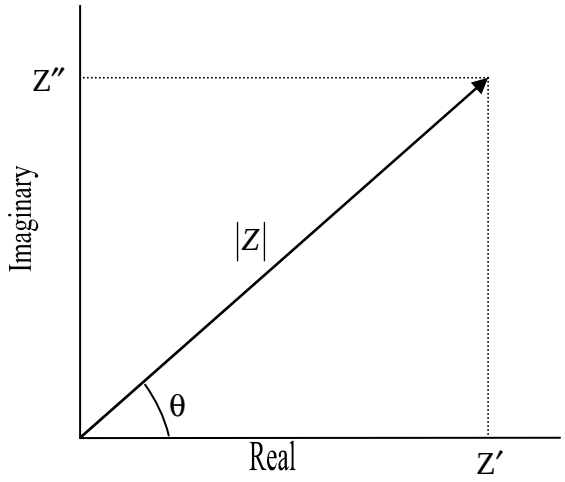

Figure 1.5 The impedance |Z| plotted as a planar vector. (From MacDonald[36])

In order to analyze and interpret experimental data, it is essential to have an equivalent circuit model. This model is chosen by the following: (1) intuition regarding the kind of impedances which are expected to be present in the sample, and whether they are connected in series or parallel; (2) examination of the experimental data to see whether the response is consistent with the proposed circuit; and (3) inspection of the resistance and capacitance values that are obtained to determine whether they are realistic and whether there is a temperature dependence.[40] For each data set there is the potential for multiple equivalent circuits, but, typically, only one makes sense for the electrical makeup of the sample. An example of a typical equivalent circuit representing the bulk sample and the grain boundary can be found in Figure 1.6, where R_1 and R_2 are resistors and C_1 and C_2 are capacitors.

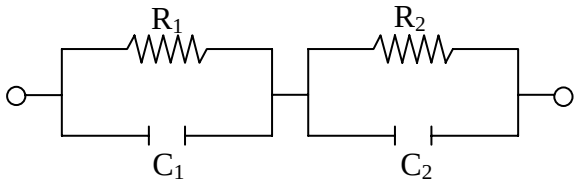

Figure 1.6 Typical equivalent circuit representing the bulk and the grain boundary.

Figure 1.7 shows an idealized impedance complex plane plot showing two semicircular arcs and a circuit. The circuit consists of a series connection of two sub-circuits, one represents grains and the other represents the grain boundary phase.[41]

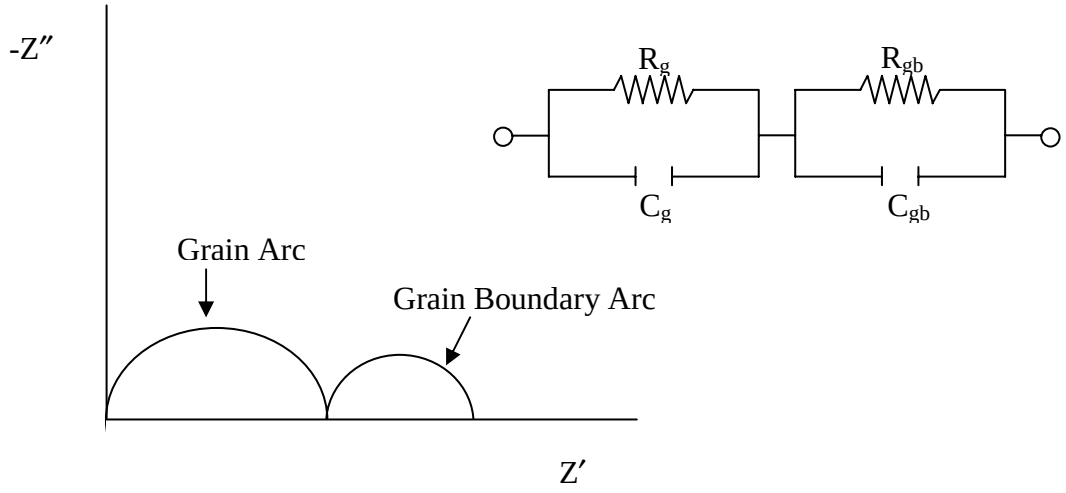

Figure 1.7 Idealized impedance plot showing two arcs and its equivalent circuit.

The impedance of the equivalent circuit can be described by both the real part (Z′) and the imaginary part (Z″):[40]

$$Z' = \frac{R_g}{1+(\omega R_g C_g)^2} + \frac{R_{gb}}{1+(\omega R_{gb} C_{gb})^2} \tag{16}$$

$$Z'' = R_g\left(\frac{\omega R_g C_g}{1+(\omega R_g C_g)^2}\right) + R_{gb}\left(\frac{\omega R_{gb} C_{gb}}{1+(\omega R_{gb} C_{gb})^2}\right) \tag{17}$$

where $\omega=2\pi f$ is the angular frequency and C_g, R_g, C_{gb}, R_{gb} are the capacitance and resistance of grains and grain boundaries respectively.[40,41] The resultant graph of Z′ versus Z″ can be read to find the resistance of both the grain and the grain boundary.

Figure 1.7 shows an idealized system, which is often not the case. Experimental data tends to show pieces of arcs which must be extrapolated to the Z′-axis to ensure accurate data collection. Computer software is available that can fit the equivalent circuit to the experimental data.[42] If data is collected over a variety of temperatures, the conductivity can be found, and an Arrhenius plot can be made. The most common format is 1000/T (Kelvin) versus Log_{10}(Conductivity (S/cm)) so that activation energy can be calculated if necessary.

1.5.2 DC Conductivity

Measurement of accurate conductivity values can be difficult when polycrystalline materials are involved. Ideally, the direct current (DC) conductivity should be measured, to ensure that the values pertain to long range ion migration and not to dielectric losses such as those associated with limited or localized rattling of ions within cages.[43] DC conductivity is done by taking a fixed voltage, measuring the current, and obtaining the resistance. By taking the dimensions of the sample and the resistance, the conductivity can be determined. One of the major difficulties of DC measurements is finding a suitable electrode material to prevent polarization effects at the electrode-solid electrolyte interface.[43]

1.6 Sintering

There are effectively two steps when ceramics are fabricated from powders. The first step is the processing that occurs prior to the firing of the green body, and the second step includes the processes that occur during firing. There has been considerable discussion of the powder processing of Aurivillius phases[44], yet there has been little interest in the literature of the crucial second step in Aurivillius processing- densification. Changes that occur during the firing process are related to (1) changes in grain size and shape, (2) changes in pore shape, and (3) changes in pore size.[45] Figure 1.8 displays a flow chart for the production of polycrystalline ceramics.

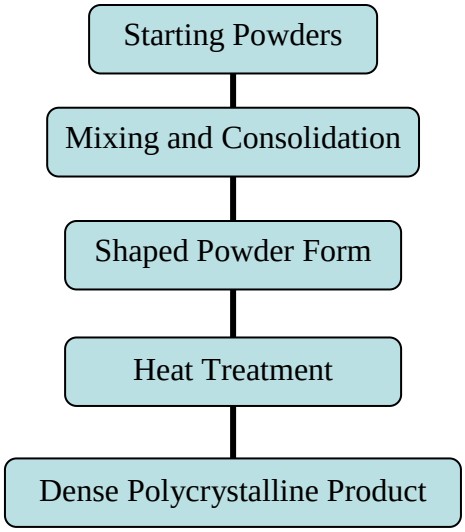

Figure 1.8 Basic flow chart for the production of polycrystalline ceramics. (From Rahaman[46])

Densification occurs through the firing stage of the production process. Here, the shaped powder form is heated to produce the desired microstructure. Effectively, the powders have joined together into an aggregate that has strength.[47] The driving force for sintering is the reduction in surface free energy of the system consisting of the mass of consolidated particles.[46] The various microstructural stages of sintering are shown in Table I-III. The densification rate is enhanced by smaller particle size, higher sintering temperature, and high external pressure.[46]

Table I-III Microstructural Changes Observed in the Initial, Intermediate, and Final Stages of Solid-State Sintering (Powder Compact). (From Reed[47])

Stage	Observations
Initial	Surface of particles begin to smooth
	Grain boundaries form and necks grow
	Rounding of pores
	Diffusion of dopants
	Porosity decreases <12%
Intermediate	Shrinkage of open pores intersecting grain boundaries
	Mean porosity decreases significantly
	Slow grain growth
Final (1)	Closed pores containing kiln gas form when density is ~92% (>85% in heterogeneous materials)
	Closed pores intersect grain boundaries
	Pores shrink to a limited size or disappear
	Pores larger than grains shrink slowly
Final (2)	Grains of much larger size appear rapidly
	Pores within larger grains shrink

1.6.1 Sintering Accelerators

A sintering accelerator is a material added to the precursor powders that accelerates sintering and/or decreases sintering temperatures. A significant proportion of ceramic products used in low-temperature applications are predominately crystalline materials containing a minor amount of a glassy phase distributed in the grain boundaries including alumina substrates, spark plug insulators, and grinding media.[47] Usually less than one volume percent liquid phase is sufficient to coat the grains if the liquid is distributed uniformly in a material with a nominal one micron grain size.[47] Sintering accelerators have been explored for some Aurivillius phases, but it has been limited to the O_9 family.[48,49] Bismuth oxide has been shown to substantially improve the sintering of $SrBi_2Ta_2O_9$, as well as markedly enhance the preferred orientation at the surface of the sintered specimens.[49]

1.7 Statistical Design and Analysis

Designed experiments have a number of goals, but the most important of them is that the experiments are sufficient in number so that important effects are detected, trivial variables are eliminated, and they are distributed in a design space that yields the maximum amount of information possible.[50] One of the most efficient types of designs is called a D-optimal design. A D-optimal design is usually done by specifying a model, determining the region of interest, selecting the number of runs to make, specifying the optimality criterion, and then choosing the design points from a set of candidate points that the experimenter would consider using.[51] This research incorporated a statistical design software package, including Experimental Design Optimizer (EDO, version 1, Nextbridge Software, San Diego, 1999) for the experimental design, and Multiple Correlation Analysis (MCA, Nextbridge Software, San Diego, 1999) for the analysis.

1.8 Rietveld Analysis

The Rietveld method is a powerful and relatively new method for extracting detailed crystal structural information from X-ray and neutron powder diffraction data.[52] It works by using least squares refinements in a systematic fashion until a best fit is obtained between the entire observed powder diffraction pattern and a calculated pattern. The calculated pattern is based on refined crystal structure(s), diffraction optics effects, instrumental factors, and other specimen characteristics (e.g. lattice parameters).[52] An example of a Rietveld refinement plot is shown in Figure 1.9.

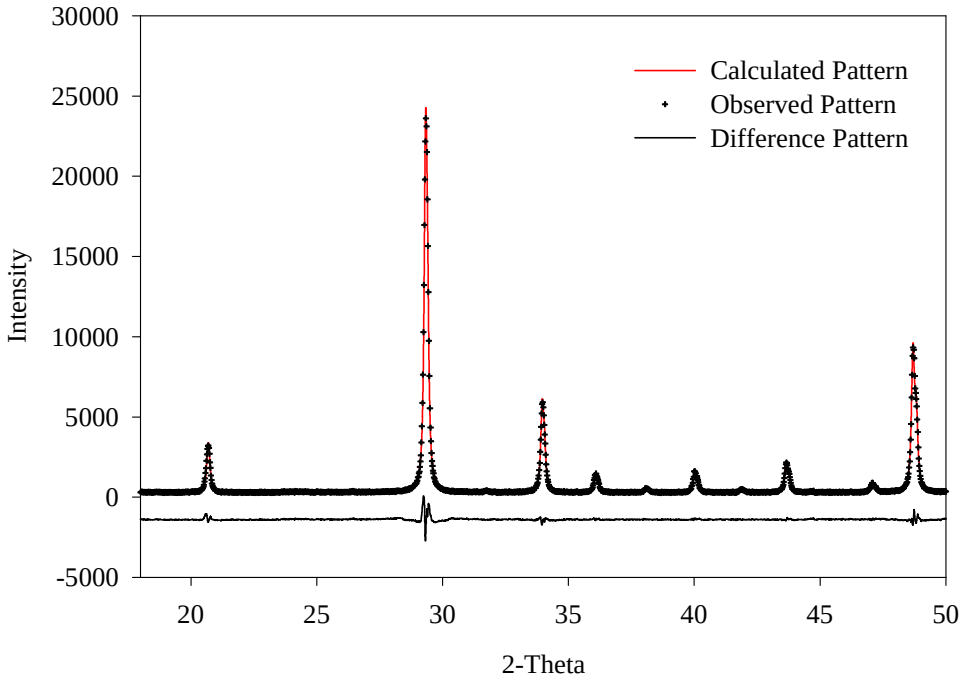

Figure 1.9 An example of a Rietveld refinement plot.

Rietveld analysis is done using computer programs. Common programs for Rietveld include GSAS (A.C. Larson and R.B.V. Dreele, "GSAS: General Structure Analysis System." Los Alamos National Laboratory, 1985-2000) which was developed in the mid-eighties, and TOPAS ("TOPAS: General Profile Structure and Analysis Software for Powder Diffraction Data." Bruker AXS, 2000). For an up-to-date list of Rietveld refinement programs see the Commission on Powder Diffraction (CPD) web pages or the International Union of Crystallography (IUCr) web pages.[53] Figure 1.10 shows a schematic of the Rietveld analysis process (see McCusker and Von Dreele[53] for a detailed analysis).

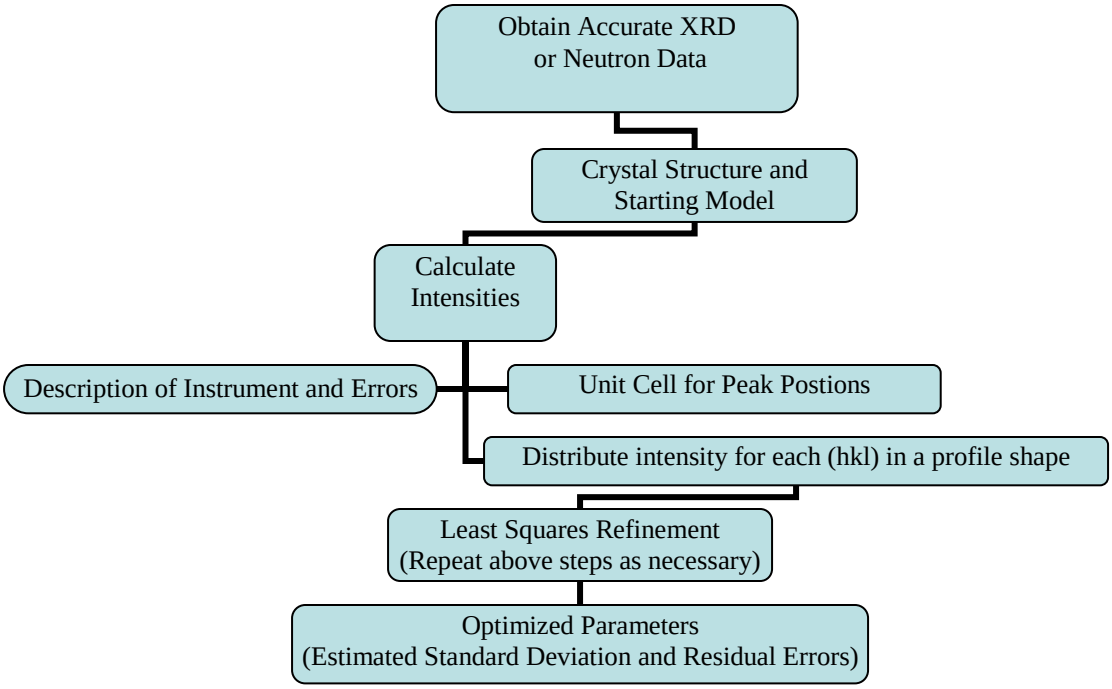

Figure 1.10 Flow diagram of Rietveld analysis. Each step, or combination of steps, may need to be repeated multiple times. (From Misture[54])

The Rietveld method has an overwhelming number of advantages, some which are listed below:

- Differences between experimental standards and unknown phases are minimized.
- Phase-pure standards are not needed for the analysis.
- Overlapped lines and heavily overlapped patterns may be used with no difficulty.
- Lattice parameters for each phase are automatically produced.
- The entire pattern is used, rather than a few selected lines, producing an accuracy and precision that is significantly better than traditional methods.
- Preferred orientation is averaged out, and simple orientation may be modeled during the refinement.[55]

2. Experimental Work

2.1 Solid-state Synthesis

2.1.1 Precursor Powder Purity and Size

The first step in this research was to ensure that the precursor powders for the formation of $Bi_2Sr_2Nb_2TiO_{12}$ were pure, as any impurities introduced initially would make it difficult to obtain a phase pure product. The four precursor powders, supplied by Alfa Aesar[Ψ], were checked via X-ray powder diffraction (XRD) to guarantee phase purity. According to the supplier, the initial reagents had the following purities: Bi_2O_3, 99.975% pure; $SrCO_3$, 97.5% pure; Nb_2O_5, 99.9% pure; and TiO_2, 99.9% pure.

One of the initial questions was whether or not the particle size of the powders would have any effect on the speed of formation of the $Bi_2Sr_2Nb_2TiO_{12}$ phase. The sizes of the precursor powders were characterized using two techniques. The first was an Amray 1810 scanning electron microscope (SEM) and the second was a HORIBA[φ] LA-920 laser scattering particle size analyzer. The SEM sample preparation consisted of ultrasonicating the sample in acetone and placing it onto a sample holder, and was then coated[*] with a palladium/gold coating. The powder was ultrasonicated so that it could be accurately compared to the laser scattering results. The accelerating voltage for the SEM was 20 kV, with a working distance of less than 25 mm, and secondary electron images were obtained.

The HORIBA was outfitted with a Pb/W laser with a sensitivity range of 0.1 μm to 300 μm. HORIBA software, version 3.06, was used to process the data. The samples were diluted to ~1 wt% suspension in de-ionized water, stirred for two minutes, and then ultrasonicated for two minutes. An intrinsic weakness of the technique is that an index of refraction must be known to accurately determine the size of the powders. The index of refraction for anatase (TiO_2) and niobium oxide (Nb_2O_3) in water were known, 1.92 and

[Ψ] Alfa Aesar, 30 Bond Street, Ward Hill, MA. 01835 USA
[φ] HORIBA Instruments Inc., 17671 Armstrong Avenue, Irvine, CA, 92614, USA
[*] Coating done using a Mini-Coater, Film-Vac Inc., 1060 T Elm St. Ridgefield, NJ 07657, USA

2.12, respectively, but the other powders refractive indices in water could only be estimated.

2.1.2 Calcination

The first step in the solid state synthesis process was intimately mixing stoichiometric amounts of precursor powders including: Bi_2O_3, $SrCO_3$, Nb_2O_5, and TiO_2 (purities can be found in 2.1.1). A sample batch is shown in Table 2-I. These powders were weighed to the nearest 0.001g using a Mettler Toledo[Φ] AG204 DeltaRange balance, and ground (dry) together using a Diamonite® mortar and pestle. Next, they were put into suspension with acetone (~15 ml) and stirred every five minutes. The acetone was allowed to evaporate and the powders were put into an uncovered alumina crucible. The crucible was then weighed and placed in a furnace. The furnace[*] was ramped at 300°C per hour to 815°C in air. This temperature was chosen because it is slightly below the 817°C melting temperature of Bi_2O_3[56], yet is high enough to drive off any organic impurities. The dwell time was 10 hours and the furnace was cooled at 300°C per hour. All of the furnaces were calibrated using a digital strip chart recorder[ξ] and the fluctuation of the dwell temperature was ±3°C at elevated temperatures. After cooling, the crucible was immediately weighed. This process, referred to as calcining, is the elimination of the carbonate to form oxide. Also, for this system, it reacts the bismuth oxide to prevent melting.[35] The powders were then ground and X-ray powder diffraction was used (discussed later) to determine if the carbonate was removed.

[Φ] Mettler Toledo, Inc., 1900 Polaris Parkway, Columbus, OH 43240 USA
[*] Barnstead/Thermolyne Corporation, 2555 Kerper Boulevard, P.O. Box 797, Dubuque, Iowa 52004 USA
[ξ] Omega RD 850 Solid State Paperless Data Recorder, OMEGA, One Omega Drive, Box 4047, Stamford, CT 06907

Table 2-I Stoichiometric Amounts of Precursor Powders Used to Form $Bi_2Sr_2Nb_2TiO_{12}$

Precursor Powder	Mass (g)
Bi_2O_3	11.417
$SrCO_3$	7.234
Nb_2O_5	6.513
TiO_2	1.957

2.1.3 X-ray Powder Diffraction

After each solid state synthesis step, the powders were ground and then checked with XRD. Either a Phillips[¥] XRG 3100 or a Siemens D-500 was used. The Phillips diffractometer used a side-drifted holder, while the Siemens used a rotating top loaded sample holder. Both diffractometers utilized copper K_α radiation and were run at 30mA/40 kV. The step size was 0.02° with a count time from three to ten seconds depending on the application.

2.1.4 Subsequent Heat Treatments

Once the powders were calcined, three more heat treatments were necessary to form phase pure $Bi_2Sr_2Nb_2TiO_{12}$ (Table 2-II). At each step, the following process was done to the powders. First, the powder was ground in a Diamonite® mortar and pestle. The powder was then placed into a beaker with approximately 15 ml of acetone. The suspension was stirred regularly by hand and the acetone was allowed to evaporate. The powder, once dried, was re-ground and pressed into a pellet using a steel die and oleic acid as a lubricant. The pellet was 1.9 cm in diameter and was pressed to 91.9 MPa (13,300 psi).

[¥] PHILIPS XRG 3100, Norelco goniometer, (PANalytical Inc., 12 Michigan Drive, Natick, MA 01760)

Table 2-II $Bi_2Sr_2Nb_2TiO_{12}$ Firing Schedule

Heating Time (hours)	Temperature (°C)
10	815
12	1095
12	1095
24	1095

After being pressed, the pellet was weighed, placed in a magnesium oxide crucible and buried in a sacrificial powder bed. The powder bed was the same composition as the pellet. The crucible was then covered with a fitted lid and the entire crucible (pellet, lid, and sacrificial powder) were weighed. The crucible was placed in a furnace and ramped at 300°C per hour to 1095°C in air and held there for either 12 or 24 hours depending on the step (see Table 2-II). The crucible was then cooled at 300°C per hour to room temperature. Next, the crucible was removed and weighed. The pellet was then removed from the crucible and weighed. The pellet was broken apart and ground (dry) with a Diamonite® mortar and pestle. The subsequent powder was checked with XRD for phase purity.

2.1.5 Phase Purity

There are no current Powder Diffraction Files (PDF) for $Bi_2Sr_2Nb_2TiO_{12}$, just isostructural phases such as $SrBi_3NbTiO_{12}$ (PDF#49-1589) so comparisons must be made. Furthermore, there are a number of impurity phases that can potentially form. Two techniques were utilized to determine if $Bi_2Sr_2Nb_2TiO_{12}$ was phase pure, including SEM and XRD. The most common impurity phase was the Aurivillius phase, $SrBi_4TiO_{15}$, which can only be discerned with XRD, long measurement times (>10 seconds) and small step sizes (0.02°). Rietveld analysis was done using GSAS[57] to confirm purity and model any impurities. Data was obtained with a Siemens D-500 X-ray diffractometer, utilizing Cu K_α radiation with 0.3° divergence slits. Measurements were from 2° to 140° 2θ with a 0.02° step size and a 10 second count time. The sample was evenly dispersed on a quartz zero background holder to a thickness of approximately

1 mm. The sample was spun to average out any preferred orientation that the powder may have had.

2.2 In-situ Formation of $Bi_2Sr_2Nb_2TiO_{12}$

In order to study the in-situ formation of $Bi_2Sr_2Nb_2TiO_{12}$, a custom high temperature X-ray diffractometer (HTXRD) was used. The HTXRD is shown in Figure 2.1 with the major components highlighted. Figure 2.2 shows the heating element with the specimen holder. Stoichiometric mixtures of precursor powders (Bi_2O_3; $SrCO_3$; Nb_2O_5; TiO_2) (purity and source can be found in Section 2.1.1) were mixed in a Diamonite® mortar and pestle. The mixture then was placed on the sample stage shown in Figure 2.2 and heated from 25°C to 1300°C at a ramp rate of 30°C/min. The mass of the sample stage was taken before and after to monitor mass loss. Data were collected at room temperature, and then from 650°C to 1300°C in 50°C increments to monitor phase transformations. $Cu_{K\alpha}$ radiation was used. Phase identification in the synthesis evolution was done using JADE®[58] software.

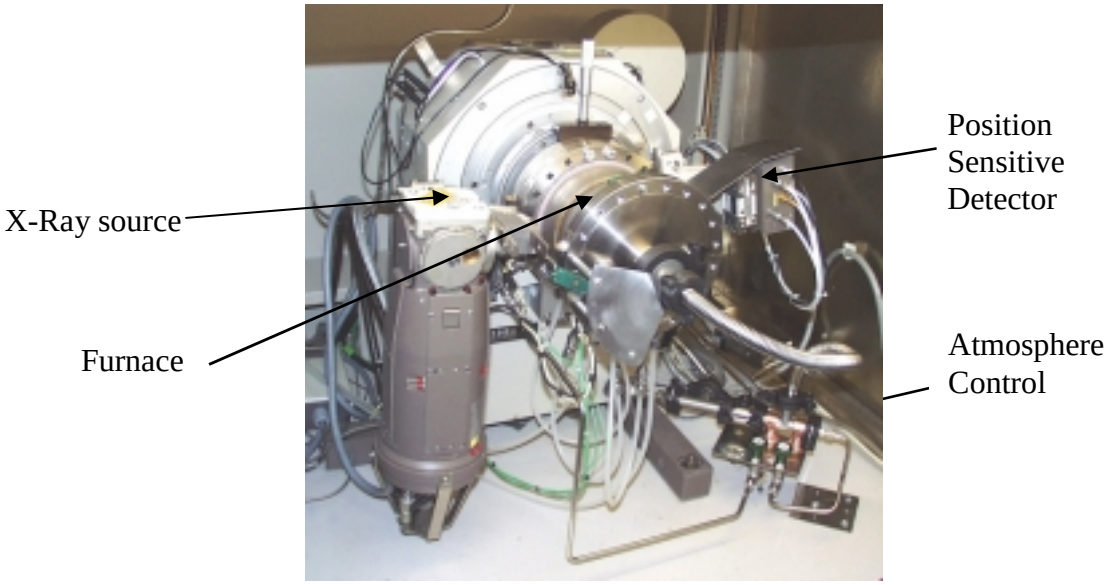

Figure 2.1 Custom HTXRD utilized for in-situ reactions under varying temperatures and atmospheres.

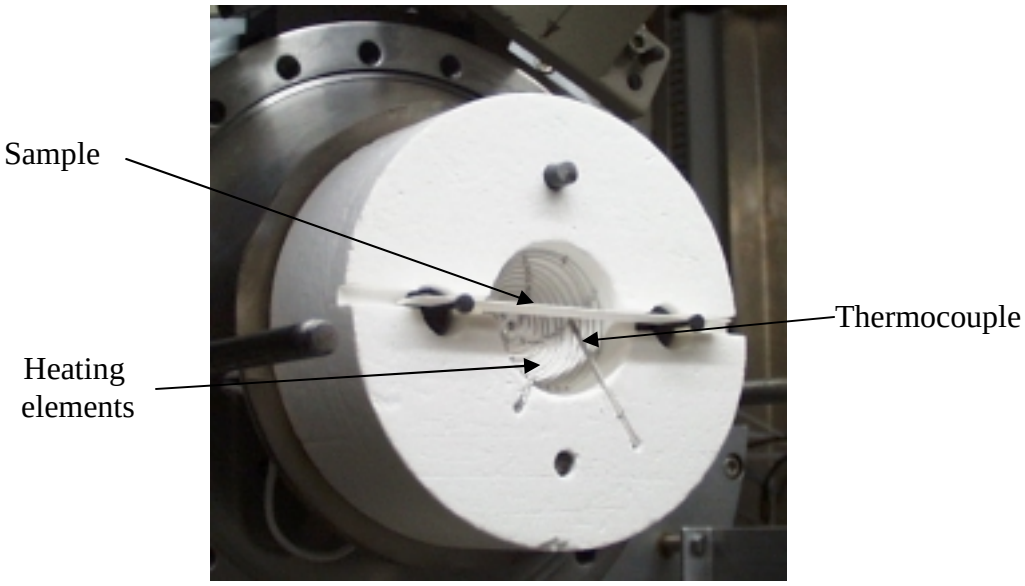

Figure 2.2 Heating element with specimen holder for the HTXRD.

2.3 Critical Phase Information

2.3.1 Bi_2O_3 Melting Temperature

The loss of Bi_2O_3 throughout the formation of $Bi_2Sr_2Nb_2TiO_{12}$ was explored with the HTXRD. Any pertinent phase changes at temperatures just below the 817°C melting temperature of Bi_2O_3 were explored. The mixture of ground stoichiometric powders were placed on the alumina specimen holder. The powders and the holder were dried in a drying oven at a temperature of 110°C for 20 minutes. The specimen holder/powders were weighed before and after the experiment to monitor mass loss. Measurements were made from 10° to 80° 2θ at a scan rate of 3° 2θ per minute. The heating rate was 30°C per minute to 810°C, where it was held for approximately six hours. $Co_{K\alpha}$ radiation was used. The resultant patterns were analyzed using JADE®[58] to determine the loss of Bi_2O_3 during in-situ phase evolution.

2.4 Forming $Bi_2Sr_2Nb_2TiO_{12}$: A Two Step Synthesis

2.4.1 Formation of $Bi_2Sr_2Nb_2TiO_{12}$ from $Bi_2SrNb_2O_9$

As previously described, one of the major impurities of the $Bi_2Sr_2Nb_2TiO_{12}$ phase is $SrBi_4Ti_4O_{15}$. In order to completely avoid this impurity, a novel synthesis technique was employed to form phase pure $Bi_2Sr_2Nb_2TiO_{12}$. This is an innovative technique because pure $Bi_2Sr_2Nb_2TiO_{12}$ can be formed without the four-layer Aurivillius impurity. The chemical equation of this reaction can be found in Equation 18.

$$Bi_2SrNb_2O_9 + SrCO_3 + TiO_2 \rightarrow Bi_2Sr_2Nb_2TiO_{12} + CO_2(\uparrow) \quad (18)$$

The first step was to form the $Bi_2SrNb_2O_9$ phase pure. This was done using solid state synthesis in a similar manner as the $Bi_2Sr_2Nb_2TiO_{12}$. Stoichiometric amounts of precursor powders (Table 2-III) were intimately mixed in a Diamonite® mortar and pestle to form a mixture that was calcined at 810°C for ten hours. The mass of the sample was taken before and after the heat treatment to find mass loss, which was correlated to carbonate loss. Furthermore, Fourier transform infared spectroscopy (FTIR) and XRD were utilized to ensure that the carbonate was gone.

Table 2-III Stoichiometric Amounts of Precursor Powders Used to Form $Bi_2SrNb_2O_9$

Precursor Powder	Mass (g)
Bi_2O_3	5.590
$SrCO_3$	1.770
Nb_2O_5	3.190

Next, the sample was pressed into a pellet 1.9 cm in diameter at 91.9 MPa (13,300 psi). The pellet was put into a magnesium oxide crucible and buried in a sacrificial powder of the same composition. The sample was heated at 300°C per hour to 1095°C and held for 12 hours, then cooled at 300°C per hour to room temperature. The sample was checked with XRD to monitor phase evolution. This process was repeated

and a phase pure sample of $Bi_2SrNb_2O_9$ was obtained, which was checked with XRD. Stoichiometric amounts of powders were then mixed with $Bi_2SrNb_2O_9$ following Table 2-IV. The powders were then calcined at 815°C for ten hours. The mass before and after the heat treatment was taken to ensure that the carbonate had been driven off. The powders were then ground and pressed into a pellet per the procedure outlined previously. Again, the pellet was put into a sacrificial powder bed within a magnesium oxide crucible. The sample was heated to 1095°C at a ramp rate of 300°C per hour and held at temperature for 12 hours. After cooling, the pellet was ground and checked with XRD. This sample was measured on the Siemens D-500 diffractometer from 5 to 140° 2θ with a step size of 0.02° and a count time ten seconds. JADE®[58] was used for phase identification, and Rietveld analysis was done (with GSAS[57]) of this sample to see if there were any impurities, and if so, to model them.

Table 2-IV Stoichiometric Amounts of Precursor Powders Used to Form $Bi_2Sr_2Nb_2TiO_{12}$

Precursor Powder	Mass (g)
$Bi_2SrNb_2O_9$	2.460
$SrCO_3$	0.434
TiO_2	0.235

2.4.2 Fourier Transform Infrared Spectroscopy (FTIR)

To ensure that the carbonate was completely removed Fourier transform infrared spectroscopy (FTIR) was done. A Bruker[α] Vector 22 Bench system was used with a MCT (mercury/cadmium/telluride) detector (sensitivity of $5*10^9$ cm^{-1}/W/Hz). A PIKE Technologies diamond ATR accessory was used (Figure 2.3). Before the measurement was done, a 55ml/minute N_2 purge was run for five minutes. Throughout the measurements, a 25 ml/minute flow rate of N_2 was used to ensure no atmospheric CO_2.

[α] BRUKER Optics Inc., 19 Fortune Drive, Manning Park, Billerica, MA 01821

The spectrum was taken and normalized using the normalization function in OPUS NT (3.0). The normalization was done from 1948 to 1776 cm^{-1}. This put the results on the same scale for easy comparison. Two samples were measured. The first sample was $SrCO_3$ (97.5% pure) obtained from Alfa Aesar and the second sample was the precursor powders after they had been calcined.

Figure 2.3 Image of a Bruker FTIR and a PIKE technologies diamond ATR accessory.

2.5 Sintering Study

2.5.1 Designed Experiments

In an effort to better understand the meaningful variables during sintering of $Bi_2Sr_2Nb_2TiO_{12}$, a sintering study was designed using D-optimal experimental design. A D-optimal experimental design models linear, non-linear, interaction effects, and any experimental constraints. There were three independent variables chosen, including sintering temperature, sintering duration, and the amount of a sintering accelerator (Bi_2O_3) added. Values for the independent variables were chosen based on literature values. The dependant variable was the density of the pellets. A design is said to be D-optimal if Equation 19 is minimized, where $(X' X)^{-1}$ is a matrix of the design:

$$\left|(X'X)^{-1}\right| \tag{19}$$

Therefore, a D-optimal design minimizes the volume of the joint confidence region on the vector of regression coefficients.[51]

The error of prediction (EOP) ratio for a single experiment is (Equation 20):

$$\frac{EOP}{S_{y.x}} = \sqrt{x'_o(X'X)^{-1}x_o} \tag{20}$$

The EOP is the regression model prediction error for experiment x_o. The overall standard error is $S_{y.x}$. The vector of one experiment in the whole design space is x_o, and X is the experimental design matrix. It is estimated that effects greater than or equal to the experimental error (assumed to be $S_{y.x}$) can be quantified if the average EOP/$S_{y.x}$ is approximately 1.0 for the whole design space.[59] The minimum number of experiments required to achieve an average EOP close to 1.0 for the variable levels are determined by computer software.

The statistical significance of each regression coefficient was determined using the t-test (Equation 21):

$$t_o = \frac{\beta_j}{\sqrt{se\beta_j}} \tag{21}$$

where t_o is the test statistic, β_j is the regression coefficient, and $se\beta_j$ is the standard error of βj. If t_o values are high, then the effects of the experiment are large. Based on the number of experiments and variables investigated in this study, if $|t_o| \geq 2.0$ there is at least a 90% confidence level ($\alpha \leq 0.10$) that β_j is significant.[60]

A statistical model (Table 2-V) was made to quantify the relationships between the independent variables (temperature, time, and %Bi_2O_3 added) and the dependent variable (density). The R^2 (coefficient of multiple determination) and the $S_{y.x}$ (standard

error) were determined. The plots of standardized residuals (d_i), residuals versus predicted values, and externally studentized residuals (t_i) were investigated to ensure the experiments were adequately scattered. A confirmation experiment was done to check the models' validity.

Table 2-V Independent Variables and Dependent Variables for Designed Experiment and Confirmation Experiments

Designed Experiments			
Experiment Number	Temperature (^oC)	Time	Wt.% Bi_2O_3 Added
1	1100	40	0
2	1100	40	2.5
3	1100	40	5
4	950	70	5
5	1100	10	5
6	950	10	5
7	1100	70	5
8	950	70	0
9	1025	40	5
10	950	10	0
11	1025	70	2.5
12	1100	10	0
13	1100	70	0
14	950	10	2.5
15	1025	10	0
Confirmation Experiments			
16	950	10	0

The experiments were made by taking approximately 1.5 grams of $Bi_2Sr_2Nb_2TiO_{12}$ and intimately mixing it with the specified amount of Bi_2O_3 per Table 2-V (or Table 2-VI). After being mixed, pellets (1.9 cm in diameter) were pressed to 91.9 MPa (13,300 psi). The pellets and sacrificial powder were placed into magnesium oxide crucibles and fired according to the schedule found in Table 2-V.

2.5.2 Density Measurement with Archimedes' Immersion Technique

ASTM standard C 20-97[61] was modified to find the density of the sintered pellets. This standard measures the apparent porosity, water absorption, apparent specific gravity, and bulk density. One of the limitations of this standard is that samples are weighed to 0.1g, therefore the procedure was modified so that the pellets were weighed to 0.0001g. The pellets were weighed after being removed from the furnace. The drying procedure was omitted because the test specimens were known to be dry. The pellets were placed in water, and boiled for two hours. During the boiling period, the pellets were completely submerged in water and remained in the water for 12 hours. The pellets were then transferred immediately to the weighing tank where the suspended weight (S) was found with an OHAUS Analytical Plus balance. Next, the saturated weight (W) was found by lightly blotting the pellet with a cotton cloth and weighing. Equation 22 shows the bulk density in grams per cubic centimeter. This assumes that $1cm^3$ of water weighs 1 gram.

$$Bulk\ Density = \frac{Dry\ Mass(g)}{W - S} \tag{22}$$

2.5.3 Additional Bi_2O_3: Beyond the Designed Experiments

Three additional experiments were conducted to investigate the effect of large amounts of Bi_2O_3 added to $Bi_2Sr_2Nb_2TiO_{12}$. The conductivity of the resulting composite, the location of the Bi_2O_3 within the sample, and the polymorph(s) of Bi_2O_3 were studied. Three samples of $Bi_2Sr_2Nb_2TiO_{12}$ were made, and 10, 20, and 30 weight percent Bi_2O_3 was added to each sample. The samples were pressed into 1.9 cm diameter pellets with a 91.9 MPa (13,300 psi). The pellets were put into a magnesium oxide crucible with sacrificial powder and fired at 1060°C for ten hours. The temperature of 1060°C was chosen because the experimental model indicated this was the optimum temperature (see Figure 3.14). The pellet density was measured using the modified ASTM standard described in 2.5.2, and the pellets were cut in half. Half of the sample was mounted in a

conventional epoxy sample mount for SEM analysis, and the remainder was ground for XRD analysis. The SEM samples were polished and coated with palladium/gold coating. Energy dispersion spectroscopy (EDS), backscattered electrons, and secondary electrons were used to determine the Bi_2O_3 distribution throughout the Aurivillius specimens. Rietveld analysis was done on the sample with 30 wt% Bi_2O_3 added in an effort to confirm which polymorph of Bi_2O_3 was present in the sample. A comparison was made with conductivity data because the conductivities of the different polymorphs of Bi_2O_3 are well documented.[62]

A differential scanning calorimeter (DSC) was used to find the transformation temperatures of the Bi_2O_3. Differential scanning calorimetry is a thermal technique where differences in heat flow into a substance and a reference are measured as a function of sample temperature while the two are subjected to a controlled-temperature program.[63] A Netzsch[χ] simultaneous TG-DTA/DSC Apparatus STA 449 C/1/4/G Jupiter® was used with a high temperature furnace (25-1550°C capability). Stainless steel sealable sample pans with gold lids and foils were used to prevent Bi_2O_3 from escaping and adhering to the furnace. The furnace was evacuated and purged with high purity dry nitrogen. Throughout the measurement, a nitrogen purge of 70 ml/minute was purged through the furnace. Also, a 20 ml/minute purge through the balance was done. The sample consisted of 80 mg $Bi_2Sr_2Nb_2TiO_{12}$ which was doped with 30 weight percent Bi_2O_3. Backgrounds were measured to ensure the oxidation of the pans did not interfere with the results.

2.5.4 Ceramic Density Calculations

In order to compensate for the porosity in the ceramic pellets, the theoretical density of the pellets was obtained. This was further complicated by the addition of Bi_2O_3 which affects the final density. The density can be calculated from the unit cell data as follows in Equation 23:

[χ] Netzsch Instruments Inc., 37 North Ave., Burlington, MA 01803

$$\rho = \frac{n'(\sum A_c + \sum A_A)}{V_c N_A} \tag{23}$$

where n′= the number of formula units within the unit cell; ΣA_c = the sum of the atomic weights of all cations in the formula unit; ΣA_A = the sum of the atomic weights of all anions in the formula unit; V_c = the unit cell volume; N_A = Avogadro's number ($6.023*10^{23}$ formula units/mol).[64]

The addition of Bi_2O_3 to the $Bi_2Sr_2Nb_2TiO_{12}$ effectively creates a ceramic composite. In order to calculate the theoretical density of a composite, the volume fractions need to be found following Equations 24 and 25:

$$V_\alpha = \frac{\frac{W_\alpha}{\rho_\alpha}}{\frac{W_\alpha}{\rho_\alpha} + \frac{W_\beta}{\rho_\beta}} \tag{24}$$

$$V_\alpha + V_\beta = 1 \tag{25}$$

where V_α= volume fraction of phase A; V_β = volume fraction of phase B; W_α = weight of phase A in composite; W_β = weight of phase B in composite; ρ_α and ρ_β are the densities of phase A and B respectively.[64] The theoretical density of the composite ($\rho_{theoretical}$) can then be found with Equation 26.

$$\rho_{theoretical} = (\rho_\alpha * V_\alpha) + (\rho_\beta * V_\beta) \tag{27}$$

The theoretical density of the composite pellets was calculated and compared to the measured density. Following Equation 28, the percent theoretical density can be obtained. The percent theoretical density is crucial for normalizing data to properly compare impedance and DC conductivity results, which will be discussed in later sections.

$$\%\rho_{theoretical} = \frac{\rho_{measured}}{\rho_{theoretical}} * 100 \quad (28)$$

2.6 Impedance Spectroscopy (IS)

The AC impedance system consisted of a Solarton[ϕ] SI 1260 impedance gain phase analyzer, a Ney[χ] Centurion Qex furnace, and a computer. A custom computer program entitled Z-View[65] was utilized to control the Solartron, furnace, and analyze data. The sintered pellets were coated with platinum[δ] ink. The platinum was cured by heating the coated pellets in a Thermolyne 48000 furnace to 900°C at a ramp rate of 100°C per hour. The pellets were held at temperature for one hour and cooled at 100°C per hour to room temperature. Next, the resistance was checked across the electrode to ensure an adequate coating. If the resistance was not zero, then the pellet was then re-coated.

The coated pellets were then placed inside the furnace resting on the platinum electrode. The second electrode was placed on top of the pellet and held in place with a piece of zirconia grinding media (see Figure 2.4). The zirconia was used to ensure good connection between the electrode and the pellet.

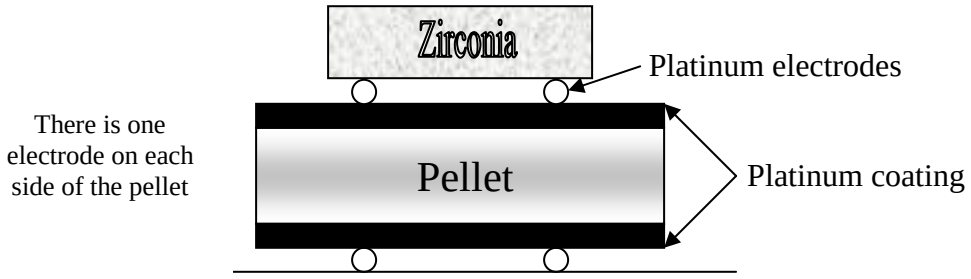

Figure 2.4 Schematic of pellet coated with platinum and electrode attachment.

[ϕ] Solartron Analytical, Unit B1, Armstrong Mall, Southwood Business Park, Farnborough, Hampshire, GU14 0NR, England
[χ] Diversified Equipment Company, Inc., 7213 Lockport Place, Lorton, VA 22079
[δ] Platinum Paste, Lot # M31914A, Engelhard-CLAL, 700 Blair Rd., Carteret, NJ 07008

An image of the set-up is shown in Figure 2.5a. The sample was heated to 700°C at a rate of 10°C per minute, and it dwelled for ten minutes at every 100° to allow adequate time for the impedance spectrum measurements. The dwells from 700°C to 900°C were every 50°, and they were again held for ten minutes. The frequency range was 5 – $5x10^6$ Hz with a logarithmic step to obtain 99 data points, and measured from low to high. The AC voltage was 1 volt. Lead corrections were applied to ensure that instrumental effects were minimal.

The data was transformed into Cole-Cole[66] plots at each measured temperature to find the resistance. In order to find the resistance, the arc intersection with Z′ was read. Depending on the sample and the phase of interest, the proper arc was measured (i.e., bulk, grain, grain boundary). Finally, Arrhenius plots were compiled to compare the results and find the activation energies as necessary.

(a) **(b)**

Figure 2.5 (a) Image of custom IS setup. (b) Image of DC Conductivity system.

2.7 DC Conductivity

DC conductivity was measured to ensure the accuracy of the IS system. The set-up consisted of a Tenma™ laboratory DC power supply[κ], a Ney Centurion Qex furnace, a computer, and two Kiethley 2000 multimeters[ω] (see Figure 2.5b). A fixed voltage of approximately 3.5 volts was applied to the coated pellets in a manner similar to Figure 2.3. Samples were heated with an identical heat treatment as found in Section 2.6. Conductivity was calculated based on resistance and the dimensions of the pellet. Results were compared with IS conductivity values to ensure IS accuracy.

[κ] Tenma™ Laboratory DC Power Supply, model 72-2085, 405 South Pioneer Blvd. Springboro, OH 45066
[ω] Keithley 2000 Multimeter, Keithley Instruments, Inc. 28775 Aurora Road, Cleveland, Ohio 44139

3. Results and Discussion

3.1 Solid-state Synthesis

3.1.1 Precursor Powders

In an effort to clarify the purity and characterize the particle size, three characterization techniques were utilized, including XRD, laser particle size analysis, and SEM. The precursor powders Bi_2O_3, $SrCO_3$, Nb_2O_5, and TiO_2 were first checked for phase purity using XRD. The limit of detection for XRD is ~5%, but the limit depends on the mass absorption coefficient of the phases of interest. There were no detectable impurities or second phases found, thereby it was concluded that the precursor powders were pure. The laser particle size analysis results can be found in Table 3-I.

Table 3-I Laser Particle Size Analysis Precursor Particle Size Results

Precursor Powders	Size (μm)	Standard Deviation
Bi_2O_3	5.5	2.8
Nb_2O_5	20.4	24.3
$SrCO_3$	7.1	7.5
TiO_2	1.8	1.5

The standard deviation of the particle size was based on the distribution in a single measurement. The large differences in standard deviation show that there is a large amount of small particle agglomeration. It should be noted that the refractive indices for Bi_2O_3 and $SrCO_3$ were estimated, therefore the data is suspect. The SEM photomicrographs shown in Figure 3.1 show the precursor powders and their morphology. These powders underwent an ultrasonic treatment for ten minutes to mimic the treatment that the powders received in the laser particle size analyzer.

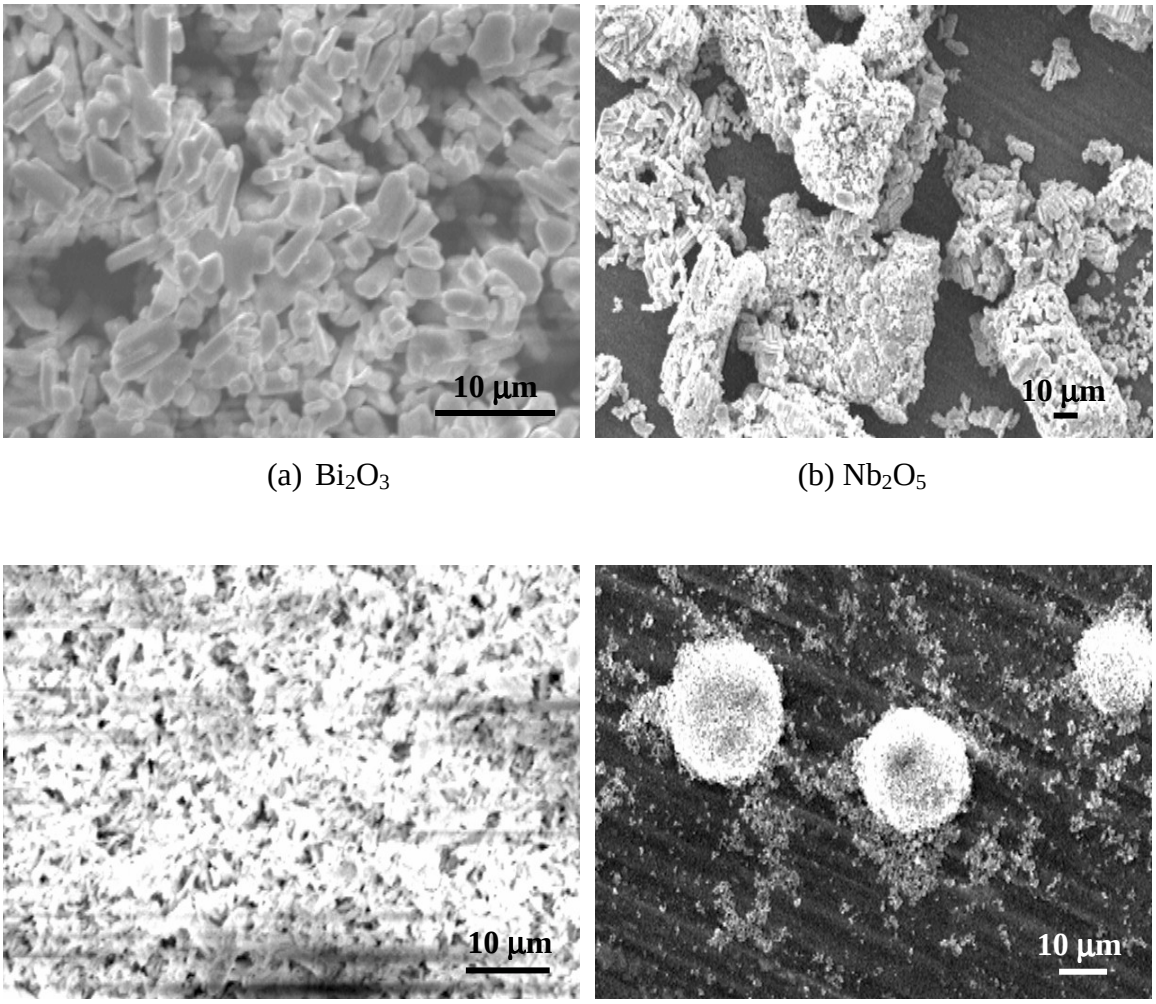

(a) Bi_2O_3 (b) Nb_2O_5

(c) $SrCO_3$ (d) TiO_2

Figure 3.1 Secondary electron photomicrographs of precursor powders after being ultrasonicated for ten minutes.

When comparing the laser particle size analysis results with the SEM photomicrographs, the Bi_2O_3 and the Nb_2O_3 particle size are within the means and standard deviations. The $SrCO_3$ and the TiO_2 photomicrographs depict different size particles then those listed in Table 3-I. The difference in particle sizes for the $SrCO_3$ and TiO_2 was due to the acetone which was used in the preparation of the sample. The acetone caused the $SrCO_3$ to coat the SEM sample stub with a uniform coating and the TiO_2 to agglomerate.

3.1.2 Calcination

The goal of calcining is to eliminate carbonate from the sample (so it does not re-crystallize on cooling) and to form the oxide. In order to check if the carbonate had been eliminated from the $Bi_2Sr_2Nb_2TiO_{12}$ precursor powders, weight loss analysis was done and XRD was performed. The solid state reaction takes on the following chemical process:

$$Bi_2O_3 + Nb_2O_5 + 2SrCO_3 + TiO_2 \rightarrow Bi_2Sr_2Nb_2TiO_{12} + 2CO_2(\uparrow) \qquad (22)$$

The ~27 g batch was prepared according to Table 2-I, and 3.7 g was lost during the calcining step. The calculated loss should be 2.2 g for all of the carbonate to be converted to the carbon dioxide. Because the loss was greater than the calculated loss, then all of the carbonate was converted. The remaining 1.5g loss is attributed to Bi_2O_3 volatization and the combustion of any remaining organics. In addition, a diffraction pattern of the precursor powders was obtained (see Figure 3.2) after calcining. There is no trace of $SrCO_3$ {Powder Diffraction File (PDF)#05-0418} in the diffraction pattern after the dwell at 815°C for ten hours, therefore the calcining was sufficient. This calcining temperature and dwell was used throughout the course of all of the solid-state synthesis.

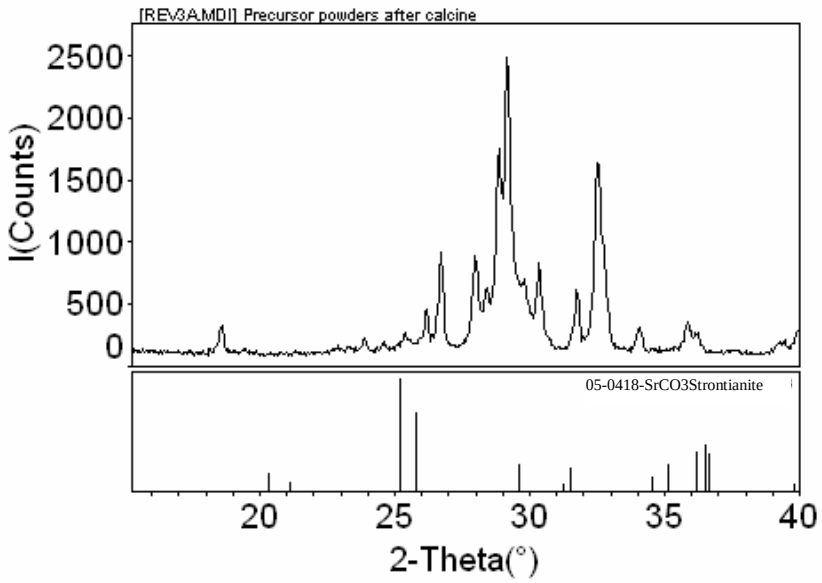

Figure 3.2 Diffraction pattern of $Bi_2Sr_2Nb_2TiO_{12}$ precursor powders after calcination.

3.1.3 Subsequent Heat Treatments

After the precursor powders were calcined, they underwent a series of heat treatments (Table 2-II) to form pure $Bi_2Sr_2Nb_2TiO_{12}$. The percent weight loss on the first firing at 1095°C was approximately two percent, and for subsequent firings the weight loss was usually a fraction of a percent. These results come from roughly five separate "batches" of $Bi_2Sr_2Nb_2TiO_{12}$ throughout the course of this research. The relatively large weight loss at the first step is attributed to excess Bi_2O_3 that may be volatizing. Proof of this came from the "yellowing" of the crucible walls and lids.

At each step in the solid state synthesis, an X-ray powder diffraction pattern was obtained to monitor phase evolution and phase purity. Figure 3.3 shows the phase evolution as a function of each solid-state synthesis step with hkl planes. After the calincing step a combination of two, three, and four layer Aurivillius phases were present along with numerous oxides. The first and second heat treatment at 1095°C yielded a sample that was almost phase pure $Bi_2Sr_2Nb_2TiO_{12}$, but with a trace of the two and four layer phases. These traces are the shoulders on the one hundred percent relative intensity

peak (107). The final heat treatment yields a phase pure sample of $Bi_2Sr_2Nb_2TiO_{12}$. A plot of peak area ratios for the one hundred percent intensity peak of $Bi_2Sr_2Nb_2TiO_{12}$ versus time is shown in Figure 3.4. Peak areas and standard deviations were found by profile fitting the peaks in JADE® using a Pearson-VII profile. Figure 3.5 shows the phase pure pattern with the closest available PDF card (#49-1589) overlayed.

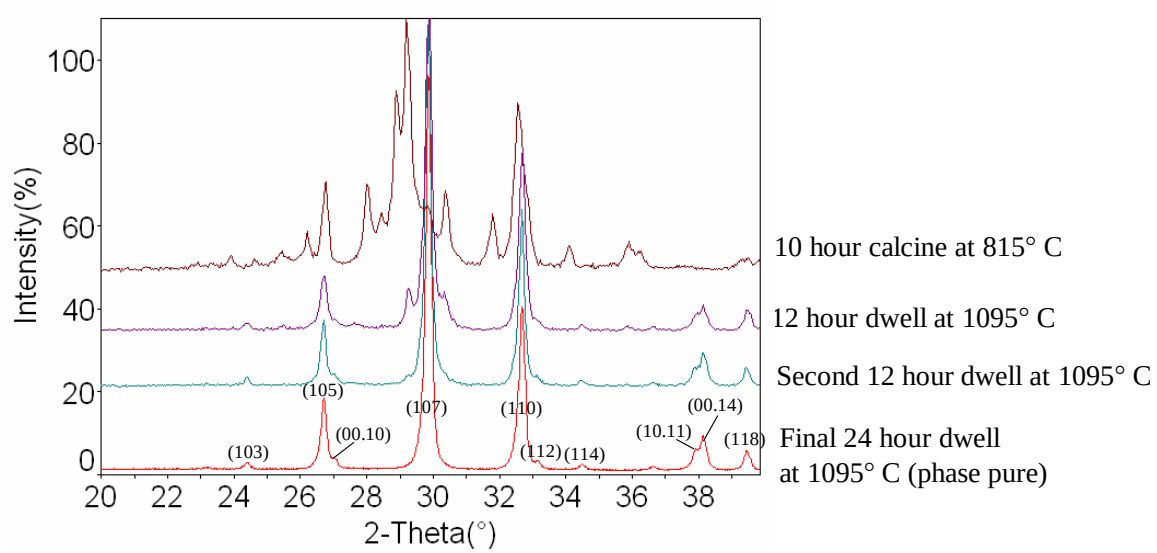

Figure 3.3 XRD pattern of the phase evolution of $Bi_2Sr_2Nb_2TiO_{12}$ as a function of each solid state synthesis step.

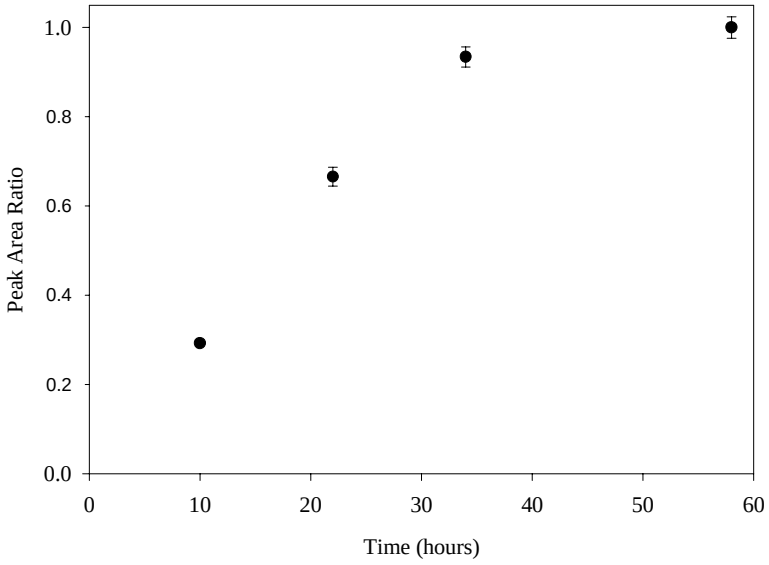

Figure 3.4 Peak area ratios for the one hundred percent intensity peak of $Bi_2Sr_2Nb_2TiO_{12}$.

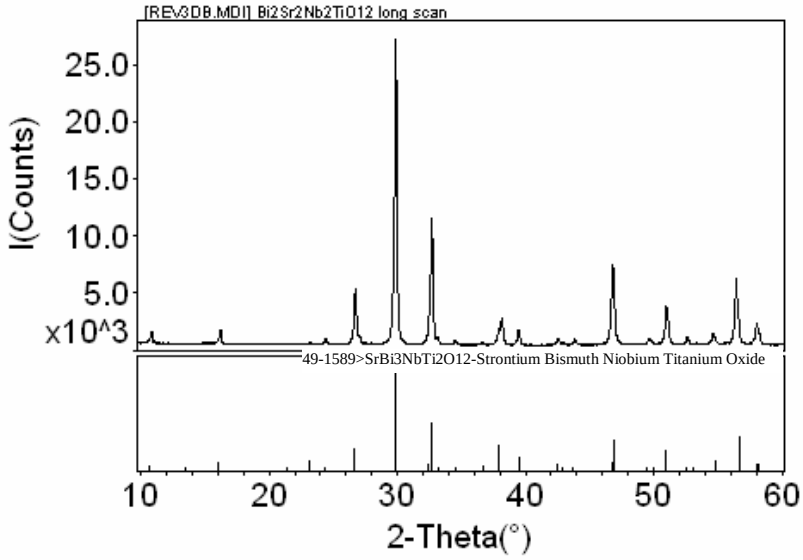

Figure 3.5 Phase pure $Bi_2Sr_2Nb_2TiO_{12}$ XRD pattern with the closest available PDF card (#49-1589) overlayed.

In order to model the XRD pattern of pure $Bi_2Sr_2Nb_2TiO_{12}$, the software package, PowderCell for Windows (PCW) was used (W. Kraus and G. Nolze, Federal Institute for Materials Research and Testing, Berlin, Germany, 1999). Initial unit cell parameters and atoms positions came from Speakman[67] (Table 3-II).

Table 3-II Refined Crystal Structure of $Bi_2Sr_2Nb_2TiO_{12}$ Without Site Mixing (From Speakman[67])

Space-Group No.	139	a	3.89505(8)
Space Group	I 4/m m m	b	3.89505(8)
		c	33.196(1)

Atom	**x**	**y**	**z**
Bi	0	0	0.21342(7)
Sr	0	0	0.0657(1)
Ti	0	0	0.5
Nb	0	0	0.3753(1)
O	0	0.5	0
O	0	0.5	0.25
O	0	0	0.4864(8)
O	0	0	0.3326(8)
O	0	0.5	0.1148(7)

Table 3-III $Bi_2Sr_2Nb_2TiO_{12}$ Unit Cell Parameters Used in PCW

Space-Group No.	139	a	3.875
Space Group	I 4/m m m	b	3.875
		c	32.7

Atom	**x**	**y**	**z**
Bi	0	0	0.215
Sr	0	0	0.0637
Ti	0	0	0.5
Nb	0	0	0.372
O	0	0.5	0
O	0	0.5	0.25
O	0	0	0.4417
O	0	0	0.32
O	0	0.5	0.1193

Speakman's lattice parameters were systematically adjusted, despite having the same composition, to obtain a better correlation with experimental data (Table 3-III). The lattice parameter adjustment was necessary because of a shift in the pattern, and intensity mismatches. In order to model the X-ray diffraction pattern of $Bi_2Sr_2Nb_2TiO_{12}$

the following parameters were used: Cu K_α and $K_{\alpha 2}$ radiation (1.540598Å, 1.544426 Å respectively), α_1/α_2 of 0.497, Bragg-Brentano geometry, step-size = 0.02, and the width of calculated profile of 16 (n*full-width-half-max). The modeled diffraction pattern is shown in Figure 3.6. The intensity mismatch of the (105) line is cause of concern. There could be many problems including: preferred orientation, thermal parameter errors, fractions and/or site occupancy, and incorrect atom positions. One of the problems with PCW is that it cannot model thermal parameters or preferred orientation. Also of concern, was the (00.10) line did not match with the experimental data. Perhaps there was a small impurity phase present. It is clear from Figure 3.6 that the experimental $Bi_2Sr_2Nb_2TiO_{12}$ XRD pattern matches quite well with the modeled XRD pattern, indicating that the sample was phase pure, or nearly phase pure.

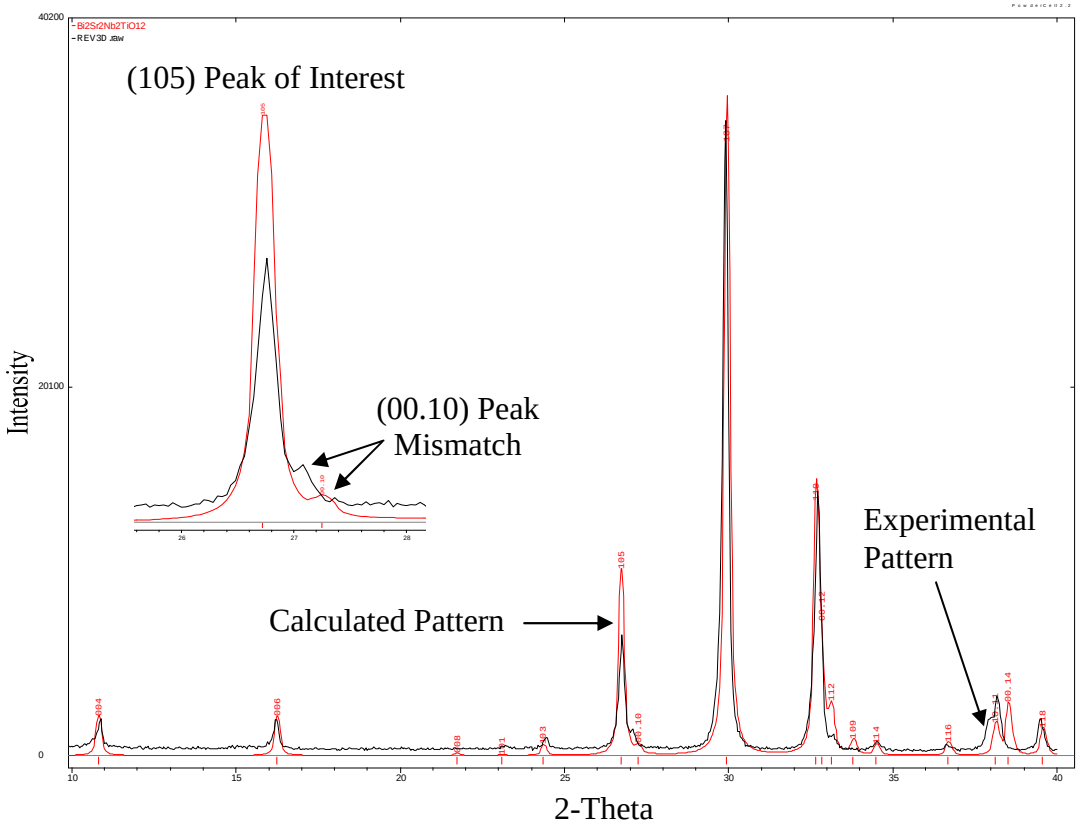

Figure 3.6 Calculated $Bi_2Sr_2Nb_2TiO_{12}$ XRD pattern with experimental XRD pattern overlay. Enlarged region showing intensity mismatch.

3.1.4 Phase Purity: In Depth

The one-hundred percent relative intensity peak (107) of $Bi_2Sr_2Nb_2TiO_{12}$ has symmetry (Figure 3.3) when standard XRD settings (2θ step of 0.02° and a count time of 5 seconds with K_α radiation) are used. At first glance this sample might be considered phase pure, but when longer count times are used (>10 seconds) then a small peak becomes visible on the high angle side of the one-hundred percent peak. This shoulder is attributed to a four-layer Aurivillius phase. The closest four-layer Aurivillius phase in the Powder Diffraction Database is $SrBi_4Ti_4O_{15}$ (PDF#43-973). Figure 3.7 shows a XRD pattern of $Bi_2Sr_2Nb_2TiO_{12}$ with a four-layer Aurivillius impurity phase, and the corresponding PDF card. The SEM (backscattered electron detector) was also utilized to find the four-layer impurity phase, but because it was so small, and had the same elemental components, it could not be found.

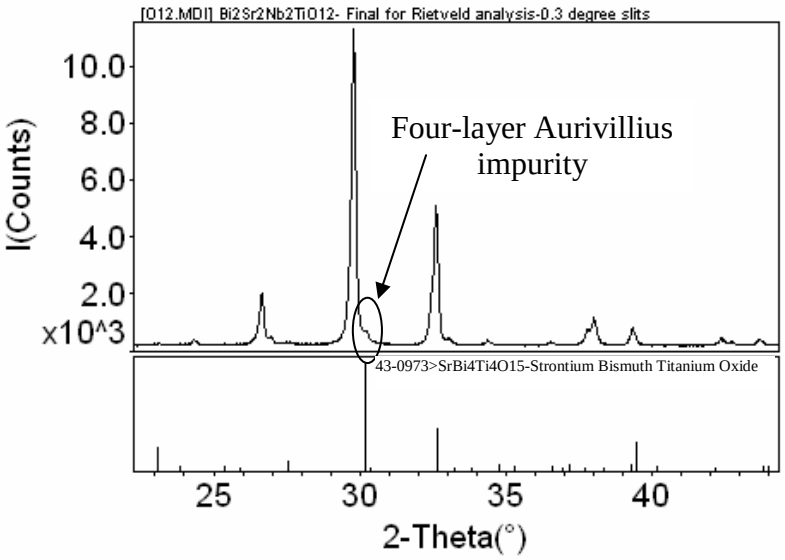

Figure 3.7 XRD pattern for $Bi_2Sr_2Nb_2TiO_{12}$ with current closest PDF card overlayed.

Rietveld analysis was done to model $Bi_2Sr_2Nb_2TiO_{12}$ using the GSAS suite.[57] The input cell and atom positions were obtained from Haluska.[68] The standard model from Haluska was more accurate than Speakman's[67], because the oxygen positions were obtained via neutron powder diffraction. The final Rietveld refinement plot of

$Bi_2Sr_2Nb_2TiO_{12}$ with the four-layer impurity is shown in Figure 3.8. A weighted residual of 0.14 and a χ^2 of 4.5 was obtained. The refined lattice parameters were as follows: a=3.8927(7) Å, and c=33.1960(9) Å for a body centered tetragonal unit cell with a space group of I4/mmm. This agrees well with Kendall's results of a=3.892(1) Å and c= 33.18(1) Å.[35] The atoms positions for the refinement can be found in Table 3-IV. It should be noted that site mixing of the Bi^{3+} and Sr^{2+} was not taken into consideration. Speakman found that without site mixing, the refinement yielded a χ^2 of 5.5 and with site mixing the χ^2 was 5.0.[67] Obviously, neither of the results were excellent, but it does suggest that site mixing does occur.

The results yielded a considerably lower χ^2 than Speakman's. There are a number of reasons for this. First, the oxygen positions had been refined based on neutron diffraction data.[68] Second, large portions of the pattern had to be excluded to obtain adequate results. Specifically, the low angle data was omitted, as well as the data at 31° 2θ which directly relates to the Aurivillius four-layer impurity. The low angle data was removed because of peak asymmetry which proved difficult to model. This peak asymmetry was due to axial divergence in the diffractometer.

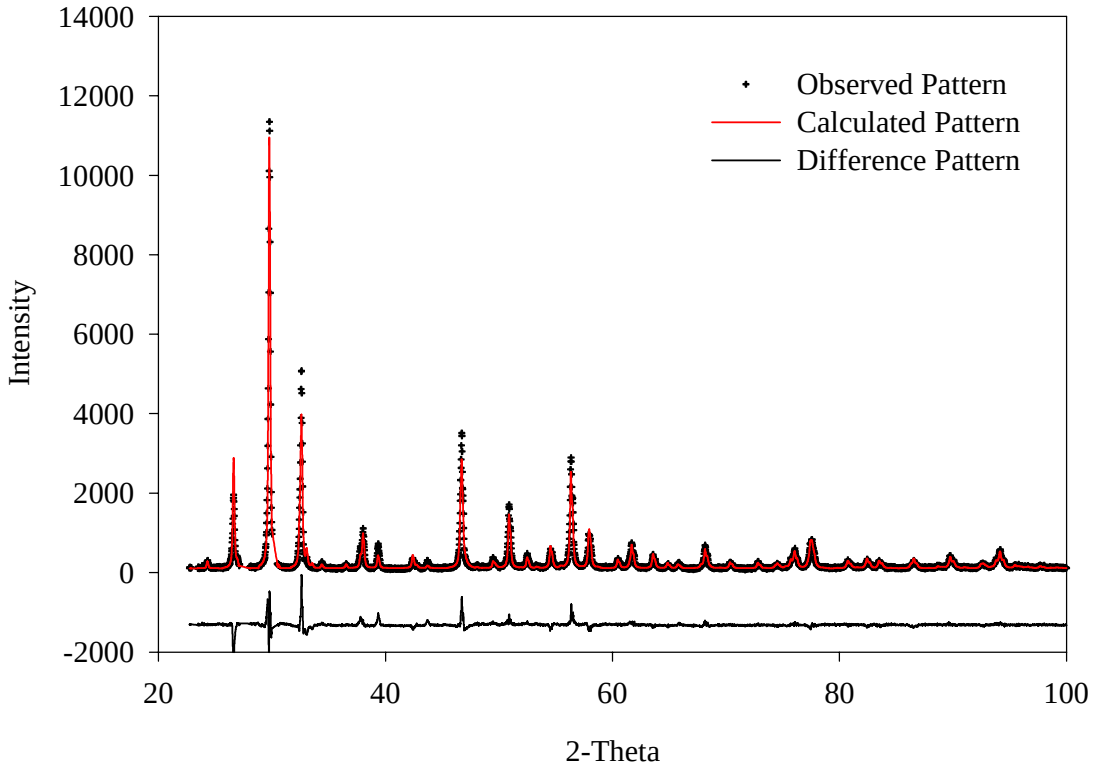

Figure 3.8 Calculated, observed, and difference patterns for $Bi_2Sr_2Nb_2TiO_{12}$ refined with the tetragonal I4/mmm space group.

Table 3-IV Refined Atom Positions for $Bi_2Sr_2Nb_2TiO_{12}$ at 25°C, Space Group I4/m m m, a=3.8927(7) Å, and c=33.1960(9) Å, R_{wp}= 0.135, χ^2=4.1, for 6561 Data Points

Atom	x	y	z
Bi	0	0	0.2137(5)
Sr	0	0	0.0637(9)
Ti	0	0	0.5
Nb	0	0	0.3720(9)
O	0	0.5	0
O	0	0.5	0.25
O	0	0	0.4511(2)
O	0	0	0.3282(7)
O	0	0.5	0.1203(4)

3.2 In-situ formation of $Bi_2Sr_2Nb_2TiO_{12}$

$Bi_2Sr_2Nb_2TiO_{12}$ has been produced in pure form using solid-state synthesis techniques. However, obtaining phase pure $Bi_2Sr_2Nb_2TiO_{12}$ was not possible on the HTXRD; instead a mixture of two, three, and four-layer Aurivillius phases formed. The in-situ evolution XRD pattern of $Bi_2Sr_2Nb_2TiO_{12}$ is shown in Figure 3.9. All phase identification was done with JADE®.[58] The XRD patterns show that a two and four-layer Aurivillius phases form by 650°C from the precursor powders. Between 800°C and 850°C the formation of $SrTiO_3$ occurs. The final composition of the sample at 1250°C is $SrTiO_3$, $SrBi_2Nb_2O_9$, $Bi_2Sr_2Nb_2TiO_{12}$, and $SrBi_4Ti_4O_{15}$, but the major phase is $Bi_2Sr_2Nb_2TiO_{12}$. Partial melting of the sample occurs between 1250°C and 1300°C. Upon cooling to room temperature, the sample was found to contain $SrTiO_3$, Bi_2O_3, $SrBi_2Nb_2O_9$, and $Bi_2Sr_2Nb_2TiO_{12}$; but the $SrBi_4Ti_4O_{15}$ had disappeared. This does not correlate with the solid-state synthesis data which clearly shows the four-layer Aurivillius phase. The phase evolution results are diagrammed pictorially in Table 3-V.

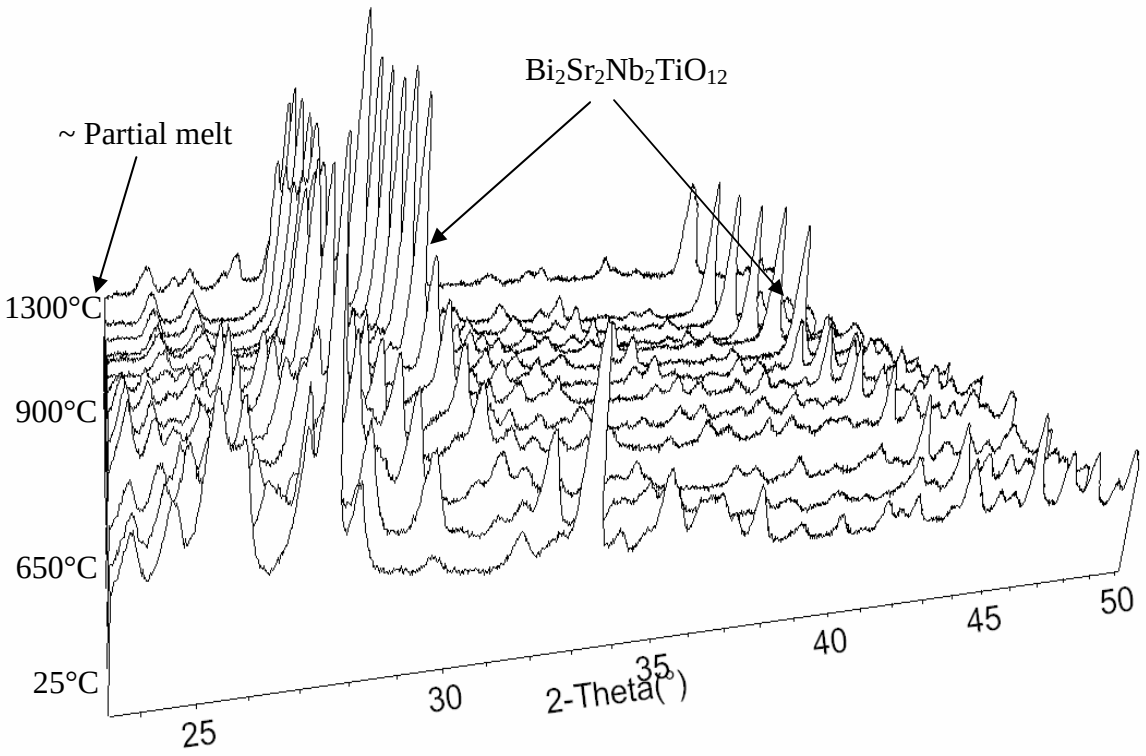

Figure 3.9 Three-dimensional perspective view of HTXRD patterns: in-situ evolution of $Bi_2Sr_2Nb_2TiO_{12}$.

Table 3-V Phase Identification of Formation of $Bi_2Sr_2Nb_2TiO_{12}$ In-situ

	25°C	650°C	750°C	850°C	950°C	1050°C	1150°C	1250°C
Bi_2O_3*	X	X	X	X				
$SrCO_3$	X	X	X					
Nb_2O_3	X	X	X					
TiO_2	X							
$SrTiO_3$				X	X	X	X	X
$SrBi_2Nb_2O_9$ (n=2)		X	X	X	X	X	X	X
$Bi_2Sr_2Nb_2TiO_{12}$ (n=3)			X	X	X	X	X	X
$SrBi_4Ti_4O_{15}$ (n=4)		X	X	X	X	X	X	X
*Goes through muliple phase changes as temperature is increased								

3.3 Critical Phase Information

3.3.1 Melting Temperature of Bi_2O_3

One of the difficulties of incorporating Bi_2O_3 into solid-state synthesis is that its melting temperature is 817°C. The HTXRD was used to investigate the loss of Bi_2O_3 from the precursors as a function of temperature. Figure 3.10 shows a three-dimensional HTXRD pattern of the precursor powders held at 810°C for approximately five hours. The results follow Table 3-V except that $SrTiO_3$ is seen to form over time. The Bi_2O_3 gradually goes through multiple phase changes and incorporates into one of the three Aurivillius phases listed in Table 3-V. The specific loss of Bi_2O_3 could not be seen because of multiple areas of peak overlap. Weight loss of the sample holder was monitored and found to be 0.2%. The weight loss of the sample could not be calculated because of volatilization of the platinum paste used in the sample holder.

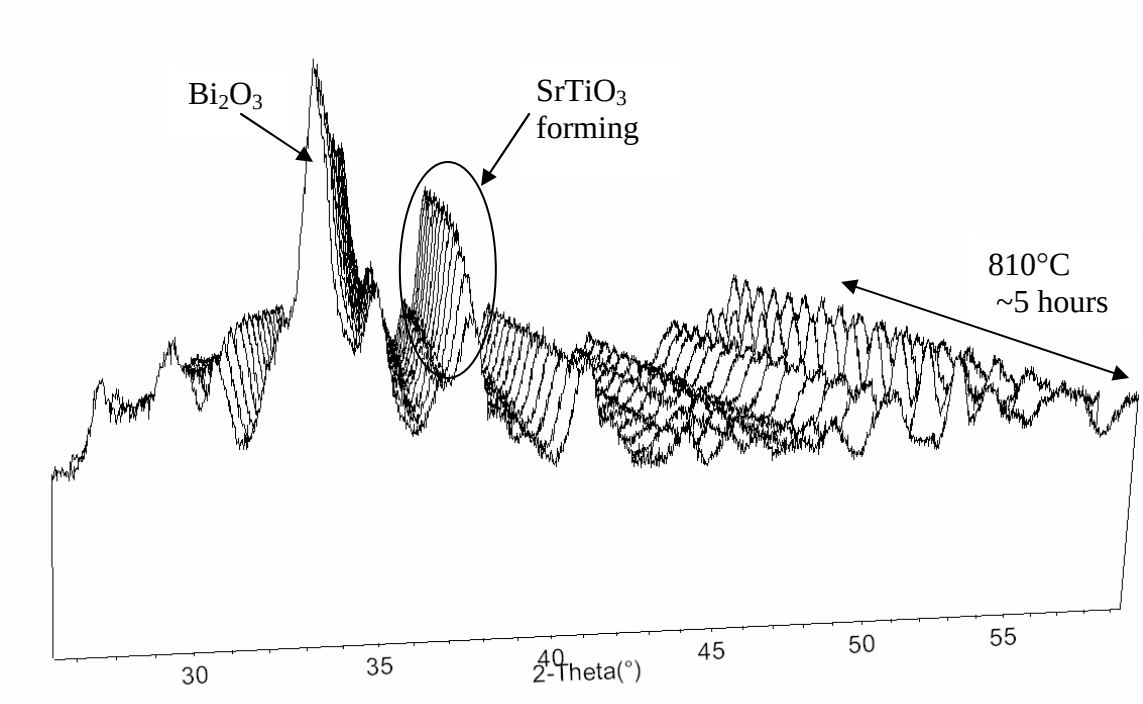

Figure 3.10 Three-dimensional overlay of a ~five hour dwell at 810°C of the $Bi_2Sr_2Nb_2TiO_{12}$ precursor powders. The $SrTiO_3$ 100% peak is circled to show the formation evolution.

3.4 Forming $Bi_2Sr_2Nb_2TiO_{12}$: A Two-Step Synthesis

3.4.1 Formation of $Bi_2SrNb_2O_9$

One of the major problems in the formation of $Bi_2Sr_2Nb_2TiO_{12}$ is the $SrBi_4Ti_4O_{15}$ impurity. The precursor powders for the formation of $Bi_2SrNb_2O_9$ after calcination had mass loss of 5.6%. In order to drive off all of the CO_2, a 4.9% mass loss was necessary, therefore it was assumed that all of the carbonate was lost. The remaining 0.7% mass loss is attributed to the volatilization of Bi_2O_3, and the combustion of any remaining organics (i.e., die lubricants). In order to check if the weight loss findings were accurate, XRD and FTIR were done. The XRD pattern of the precursor powder had no trace of carbonate. The FTIR spectra of the $Bi_2SrNb_2O_9$ precursor powders and $SrCO_3$ can be found in Figure 3.11. The spectra show that there is no remaining carbonate left in the

precursor powders. Figure 3.12 shows the XRD pattern of phase pure $Bi_2SrNb_2O_9$ after solid state synthesis and PDF #49-607.

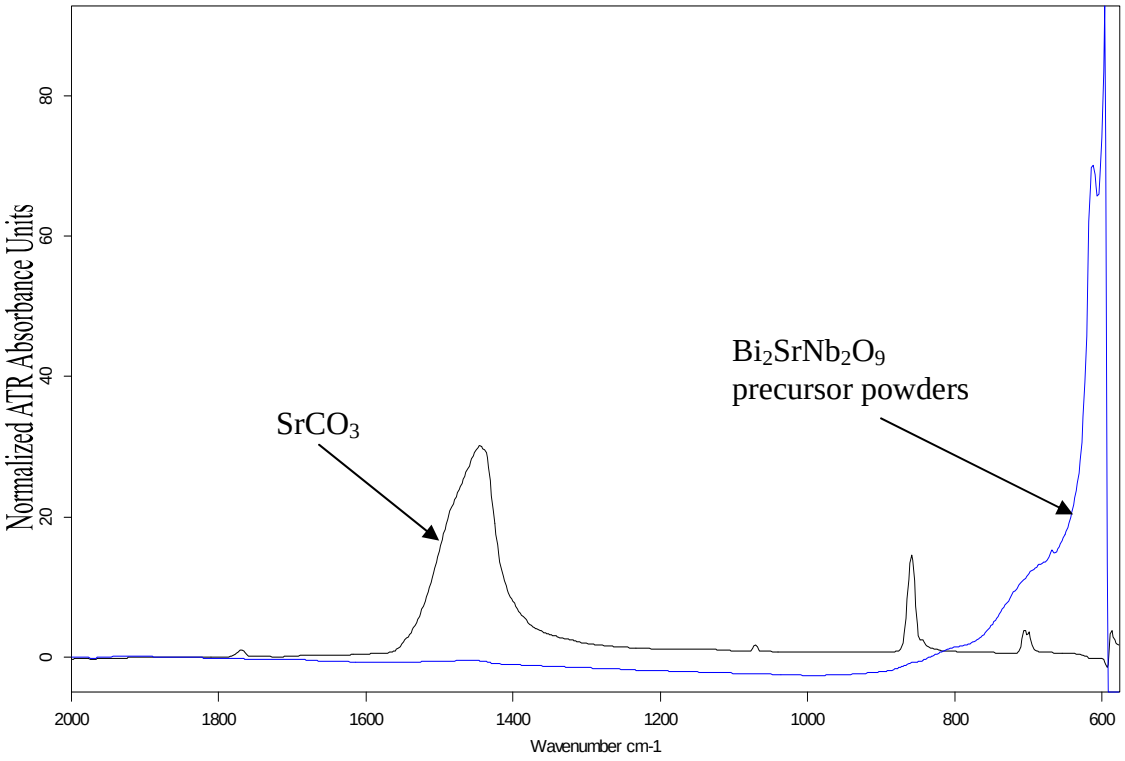

Figure 3.11 FTIR spectra showing the precursor powder after calcining and $SrCO_3$.

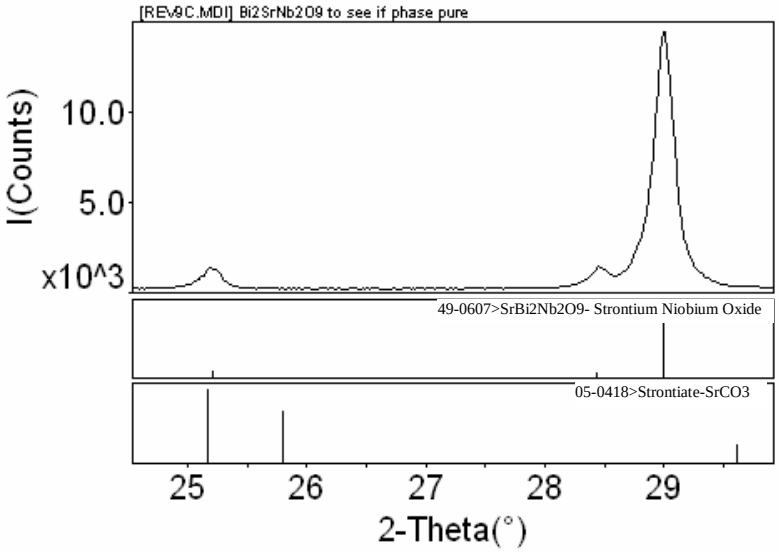

Figure 3.12 XRD pattern of pure $Bi_2SrNb_2O_9$ after solid state synthesis with PDF overlays of $SrBi_2Nb_2O_9$ and $SrCO_3$.

3.4.2 Formation of $Bi_2Sr_2Nb_2TiO_{12}$ from $Bi_2SrNb_2O_9$

The solid state synthesis steps outlined in Table 2-IV were followed. Weight loss at each step was comparable with previous synthesis steps. After completion of the solid state synthesis, a phase pure sample of $Bi_2Sr_2Nb_2TiO_{12}$ was formed. Rietveld analysis was performed with the GSAS suite[57] to determine phase purity, and see if there would be a decrease in the weighted residuals and χ^2 found earlier (section 3.1.4). Figure 3.13 shows the calculated, observed, and difference patterns for $Bi_2Sr_2Nb_2TiO_{12}$ refined with the tetragonal I4/mmm space group.

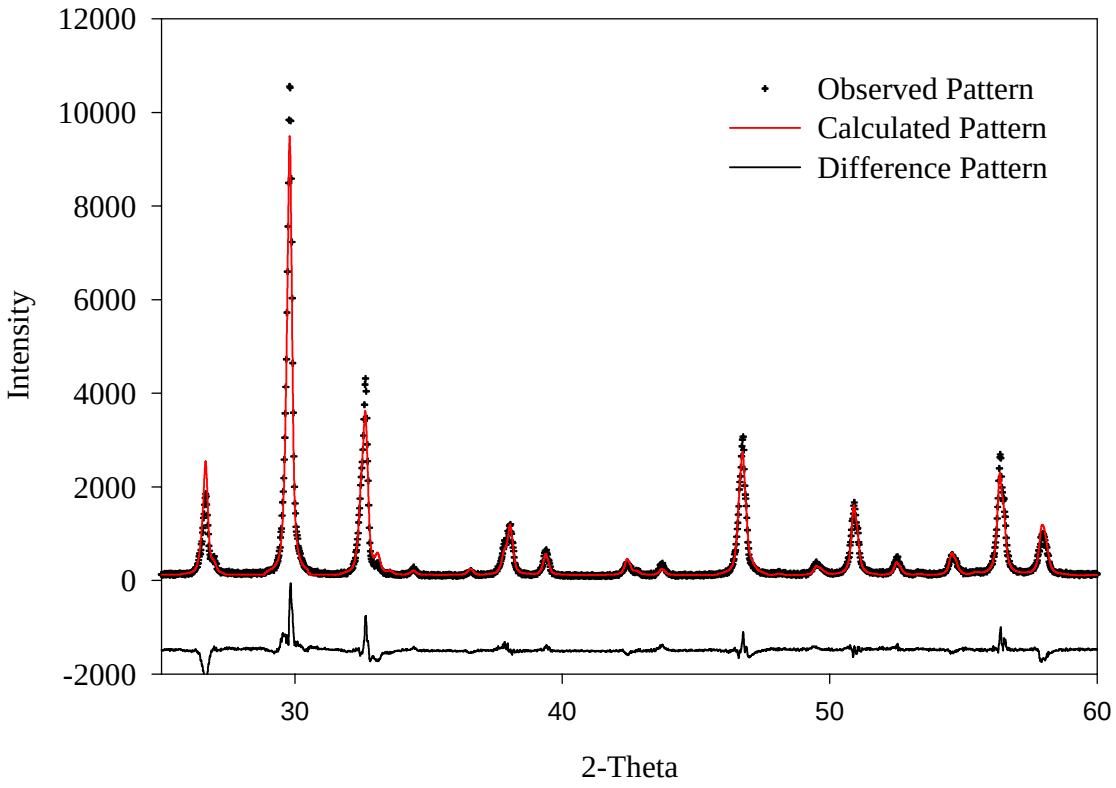

Figure 3.13 Calculated, observed, and difference patterns for $Bi_2Sr_2Nb_2TiO_{12}$ refined with the tetragonal I4/mmm space group.

The same lattice parameters, cell and atom positions were used as previously in Section 3.1.4. The $Bi_2Sr_2Nb_2TiO_{12}$ that was formed via $Bi_2SrNb_2O_9$ had a weighted residual of 0.135 and a χ^2 of 4.1. Inspection of Figure 3.13 shows that the four-layer Aurivillius impurity did not need to be excluded because it was not present, but low angle

peaks needed to be because of the axial divergence problem. Site mixing was not considered once again. One of the inherent problems with this refinement is the intensity mismatch of the peaks at 26.5° and 32.5° 2θ. This could be because of incorrect lattice parameters or perhaps preferred orientation of the (105) and the (110) respectively.

3.5 Sintering Study

The sintering study attempted to model which independent variables had an affect on the dependent variable (Table 2-V). Time did not statistically have an impact on the final density of the pellets for the study. The results were initially examined with thirteen designed experiments and three confirmation experiments. This initial model provided adequate results, but the confirmation experiments were unsatisfactory. The model was over-fit, and displaying less scatter than there really was. The model was developed further by taking fifteen designed experiments and one confirmation experiment from the thirteen designed experiments and three confirmation experiments. This resulted in an R^2 of 0.93 and a $S_{y.x}$ of 0.33. The residual plots and Cook values were checked, and showed no trends. Table 3-VI shows the variables in the model, and Table 3-VII shows the residual and Cook values based on the model.

Table 3-VI Variables Affecting Sintering Study of $Bi_2Sr_2Nb_2TiO_{12}$

Variable	Coefficient	T-value
Y-Intercept	-142	-
Temperature (^oC)	0.286	3.56
Weight % Bi_2O_3 Added	-1.64	-2.63
Temp. * Temp.	-0.000139	-3.54
Weight % * Weight %	-0.111	-3.16
Temp. * Weight %	0.00238	4.13

Table 3-VII Residual and Cook Values of Individual Experiments

Experiment	Residual
15	-0.5036
14	-0.4379
9	0.4033
2	0.3375
8	0.3328
7	-0.2252
5	-0.1952
1	-0.1307
13	0.1293
4	-0.1291
6	0.1211
10	0.1128
11	0.1002
12	0.0593
3	0.0248

Experiment	Cook Value
15	0.6184
14	0.49
9	0.3967
2	0.2644
8	0.2319
7	0.0479
5	0.036
4	0.0348
11	0.0345
6	0.0307
10	0.0266
1	0.0161
13	0.0158
12	0.0033
3	0.0006

The model did not display any high Cook values meaning that most of the designed experiments had equal "strength" in the model. The surface response plot for the model is shown in Figure 3.14. The confirmation experiment fits into the model. The results of the designed experiment, along with the three additional experiments (experiments 17, 18, and 19) are listed in tabular form in Table 3-VIII. If time allowed, further confirmation experiments should be done, especially in the design space that has not been tested. Nonetheless, this model shows the trends in density as a function of temperature, and weight percent Bi_2O_3 added to pure $Bi_2Sr_2Nb_2TiO_{12}$. The model suggest that the following variables yield $Bi_2Sr_2Nb_2TiO_{12}$ with the highest density:

- The addition of approximately four weight percent Bi_2O_3.
- A sintering temperature of 1060°C for greater than ten hours.

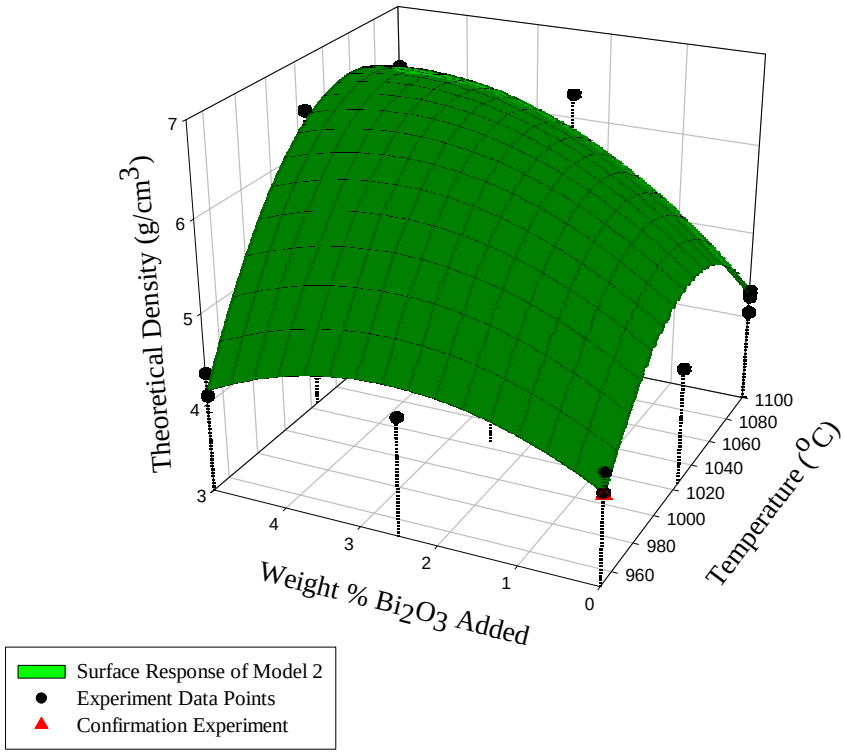

Figure 3.14 Surface response plot of the density of $Bi_2Sr_2Nb_2TiO_{12}$.

Table 3-VIII Results of Density Study

Design Experiment	Temp. °C	Time (hr.)	% Bi_2O_3 Added	Mole % Bi_2O_3	Volume Fraction $Bi_2Sr_2Nb_2TiO_{12}$	Volume Fraction Bi_2O_3	Density (Theoretical)	% Theoretical Density
1	1100	40	0	0	1.00	0.00	6.73	60.35
2	1100	40	2.5	6	0.98	0.02	6.77	92.59
3	1100	40	5	10	0.96	0.04	6.81	92.71
4	950	70	5	10	0.96	0.04	6.81	60.23
5	1100	10	5	10	0.96	0.04	6.81	89.49
6	950	10	5	10	0.96	0.04	6.81	63.91
7	1100	70	5	10	0.96	0.04	6.81	89.03
8	950	70	0	0	1.00	0.00	6.73	63.18
9	1025	40	5	10	0.96	0.04	6.81	94.62
10	950	10	0	0	1.00	0.00	6.73	59.91
11	1025	70	2.5	5	0.98	0.02	6.77	92.03
12	1100	10	0	0	1.00	0.00	6.73	63.18
13	1100	70	0	0	1.00	0.00	6.73	64.22
14	950	10	2.5	5	0.98	0.02	6.77	63.99
15	1025	10	0	0	1.00	0.00	6.73	64.37
16	950	10	0	0	1.00	0.00	6.73	59.46
Additional Experiments								
17	1060	20	10	17	0.93	0.07	6.88	71.59
18	1060	20	20	27	0.87	0.13	7.01	81.66
19	1060	20	30	34	0.81	0.19	7.13	87.92

3.6 Additions of 10, 20, and 30 Weight Percent Bi_2O_3

Three additional experiments were done to see the effect of Bi_2O_3 on the conductivity and structure of the $Bi_2Sr_2Nb_2TiO_{12}$. Pertinent density information of these samples can be found in Table 3-VIII. In order to compare the samples with large amounts of added Bi_2O_3, samples with 5 weight percent Bi_2O_3 added, 2.5 weight percent Bi_2O_3 added, and phase pure $Bi_2Sr_2Nb_2TiO_{12}$ were investigated. Photomicrographs of the samples can be found in Figure 3.15, along with EDS data. Secondary electron detection, backscattered electron detection, and EDS were used to map the microstructure of the samples. Figure 3.15 shows a photomicrograph of phase pure $Bi_2Sr_2Nb_2TiO_{12}$. There are no secondary phases present, but there is a significant amount of porosity visible. This sample (experiment 10) had approximately 60% theoretical density. EDS results show the elemental make-up, excluding oxygen, of the Aurivillius phase: bismuth, strontium, niobium, and titanium. Only qualitative data was available. Experiment 11 (2.5 weight percent Bi_2O_3) was investigated in a similar matter with the SEM. Results were similar to the sample with no added Bi_2O_3. It is assumed that either some of the Bi_2O_3 volatized, or the detectivity is beyond the capabilities of the SEM.

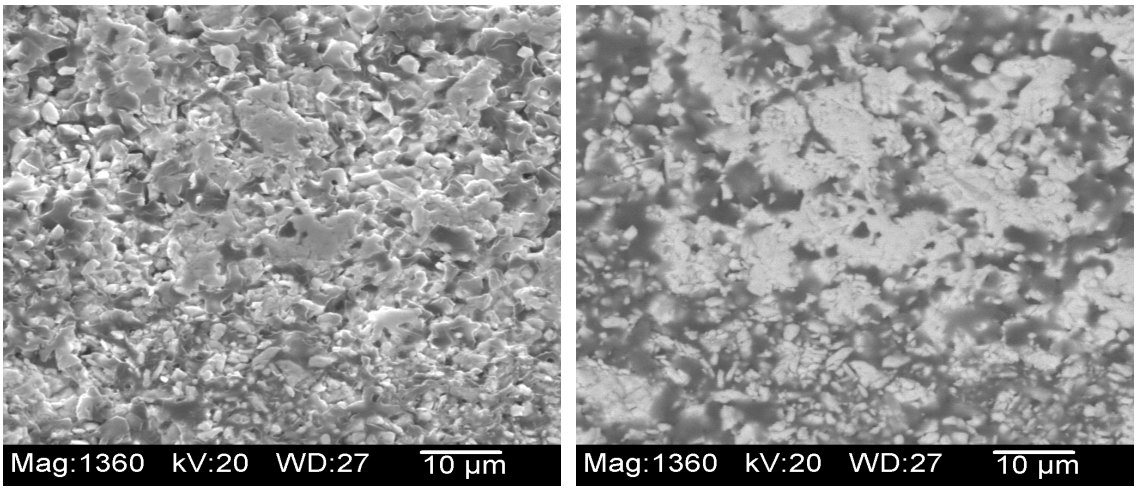

(a) (b)

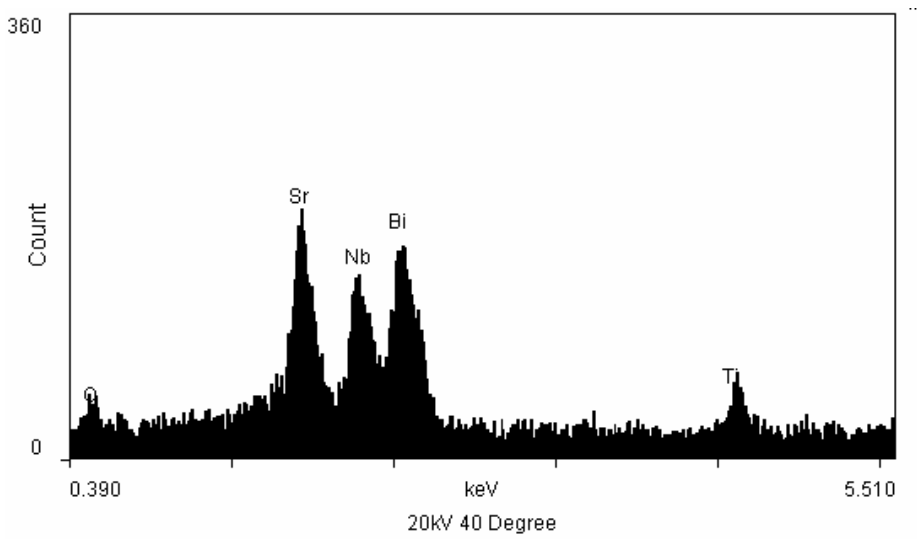

(c)

Figure 3.15 Photomicrograph of polished $Bi_2Sr_2Nb_2TiO_{12}$ using (a) secondary electrons, (b) backscattered electrons. (c) EDS data for $Bi_2Sr_2Nb_2TiO_{12}$ using a count time of 1 minute and a spot size of 100 nm.

The next sample (experiment 6) of interest contained an additional five weight percent Bi_2O_3. The Bi_2O_3 phase was visible in this sample. The photomicrographs in Figure 3.16 show the structure with secondary electrons (Figure 3.16a) and the same structure with backscattered electrons (Figure 3.16b). The bright region in Figure 3.16b is thought to be the Bi_2O_3 phase. EDS analysis was used to confirm this, but the EDS interaction volume was too large, giving erroneous results. The EDS spectra for the bright phase is very similar to Figure 3.15c. The samples with greater than 5 weight percent Bi_2O_3 also had the bright region. Figure 3.17, 3.18, and 3.19 show photomicrographs of polished samples of $Bi_2Sr_2Nb_2TiO_{12}$ with 10 weight percent Bi_2O_3 added, 20 weight percent Bi_2O_3 added, and 30 weight percent Bi_2O_3 added. Figure 3.20 shows the EDS results of $Bi_2Sr_2Nb_2TiO_{12}$ (gray), and the Bi_2O_3 (bright phase). This confirms that the bright phase found in the samples was indeed Bi_2O_3. Rietveld analysis and conductivity will be used in later sections to identify the Bi_2O_3 polymorph.

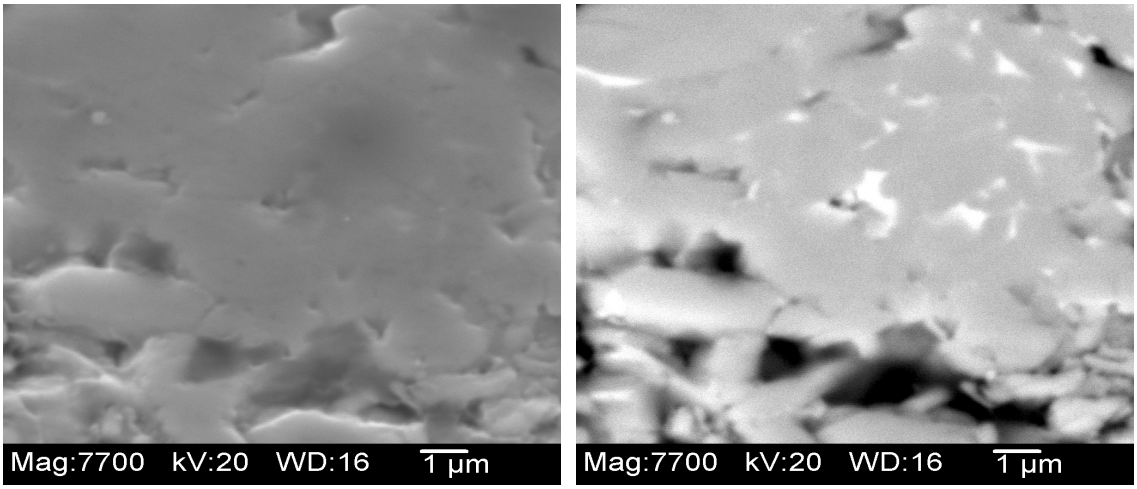

(a) (b)

Figure 3.16 Photomicrographs of polished $Bi_2Sr_2Nb_2TiO_{12}$ with 5 weight % Bi_2O_3 added using (a) secondary electrons, (b) backscattered electrons.

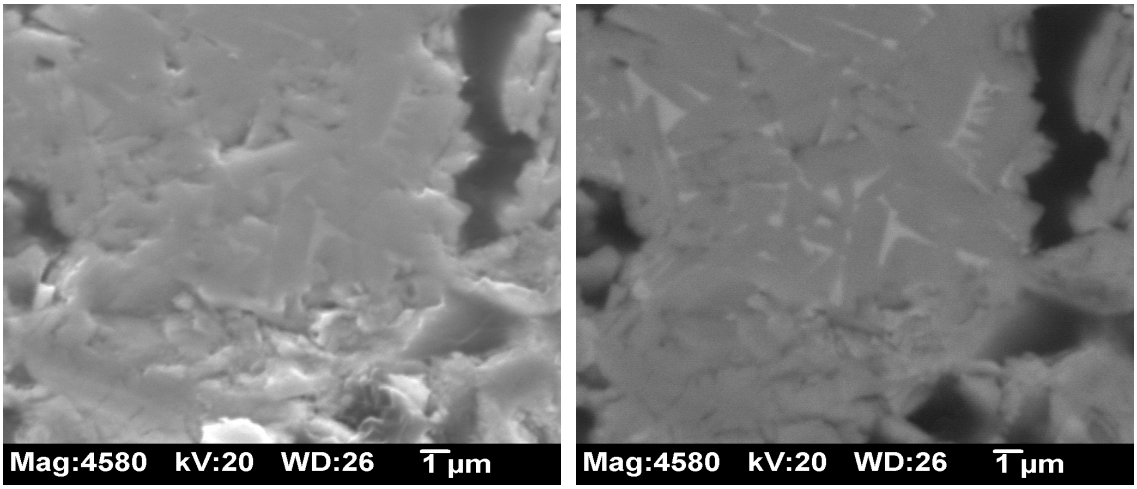

(a) (b)

Figure 3.17 Photomicrographs of polished $Bi_2Sr_2Nb_2TiO_{12}$ with 10 weight % Bi_2O_3 added using (a) secondary electrons, (b) backscattered electrons.

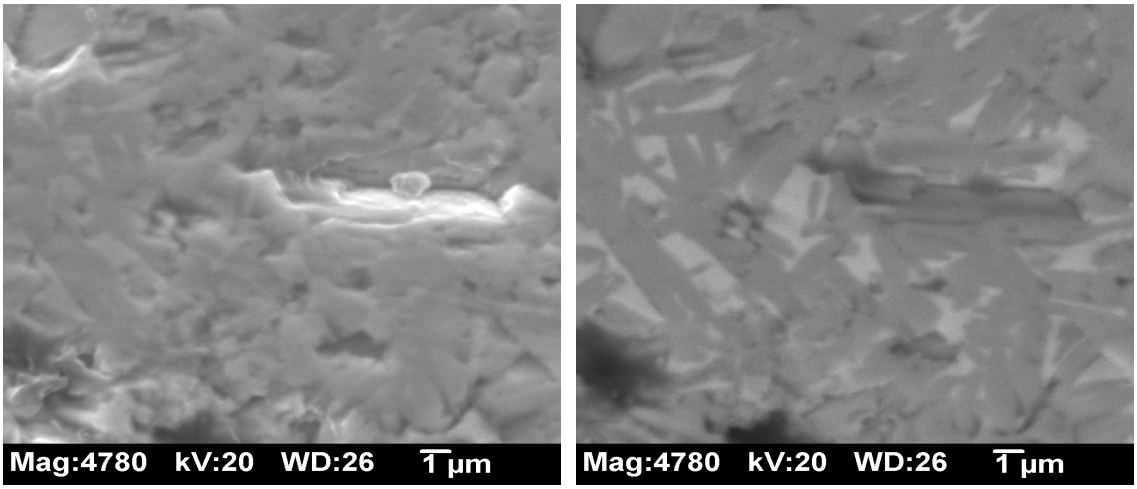

(a) (b)

Figure 3.18 Photomicrographs of polished $Bi_2Sr_2Nb_2TiO_{12}$ with 20 weight % Bi_2O_3 added using (a) secondary electrons, (b) backscattered electrons.

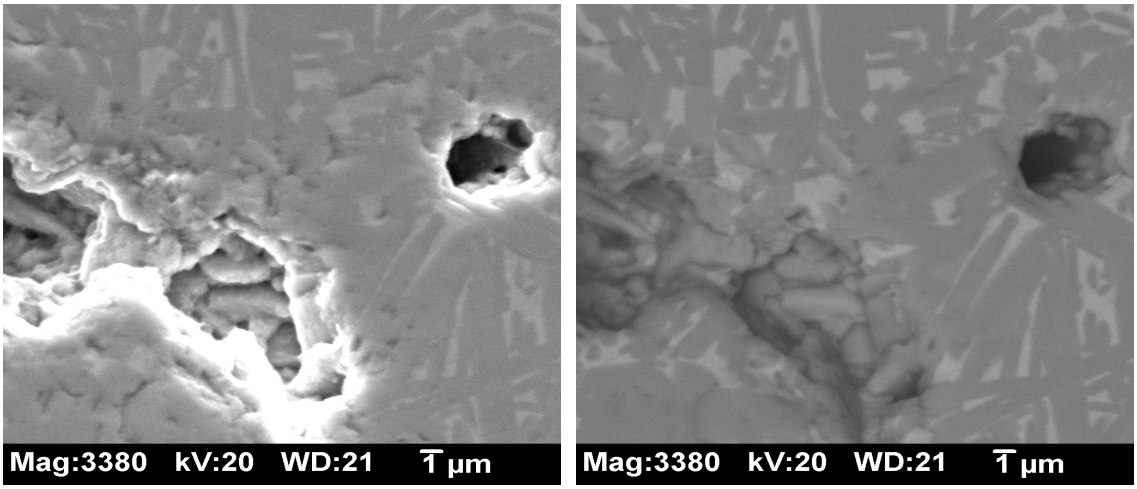

(a) (b)

Figure 3.19 Photomicrographs of polished $Bi_2Sr_2Nb_2TiO_{12}$ with 30 weight % Bi_2O_3 added using (a) secondary electrons, (b) backscattered electrons.

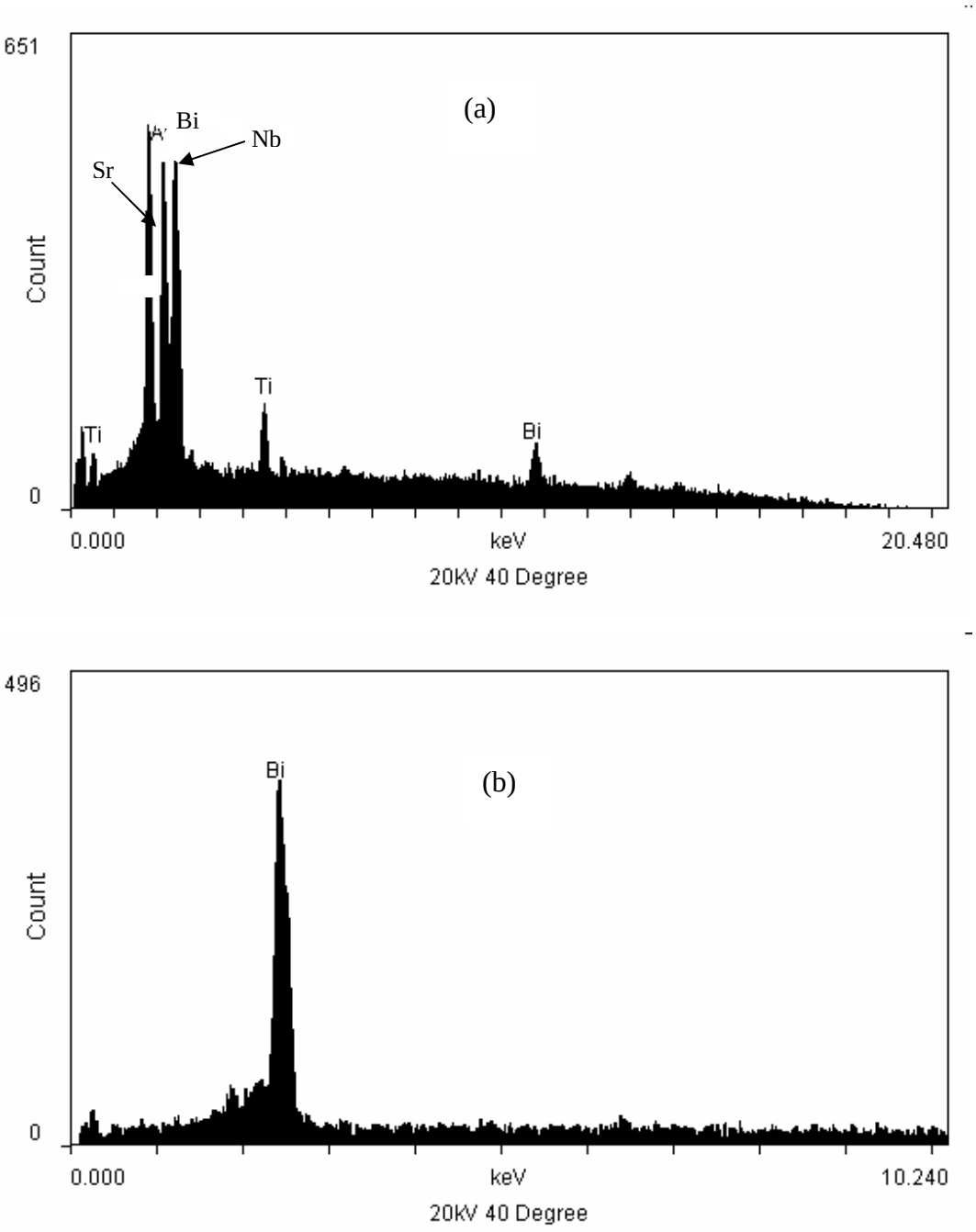

Figure 3.20 (a) EDS spectra of $Bi_2Sr_2Nb_2TiO_{12}$ (gray phase). (b) EDS spectra of Bi_2O_3 (bright phase). Both spectrum were obtained using a count time of one minute and a spot size of 100 nm.

3.7 Bi_2O_3 Polymorphs

There are various polymorphs of Bi_2O_3 that form depending on the environment that it is in. Figure 3.21 shows the characteristic data and transformation temperatures for the different phases of Bi_2O_3 while cooling. The δ-Bi_2O_3 is the high temperature phase, but upon cooling it can form into either an α, β, or γ phase. One of the major goals of this work was linking the Bi_2O_3 with SEM data, XRD data, and IS data. The SEM data in the preceeding section does not isolate the Bi_2O_3 polymorph, rather it gives qualitative data. In an effort to determine exactly which Bi_2O_3 polymorph was present, sample 19 (30 weight percent Bi_2O_3 added) was ground into a powder, and analyzed using XRD. When indexing the resulting pattern, the cubic cursor was used to determine what crystal structure was present in the Bi_2O_3. The structure was face-centered-cubic, coinciding with the δ-Bi_2O_3 phase. Phase identification was done and the Bi_2O_3 phase matched perfectly with δ-Bi_2O_3 (PDF #27-52, Figure 3.22). Rietveld analysis was used to support this finding. The International Crystal Structure DataBase[69] was searched to find the crystal structure of δ-Bi_2O_3.

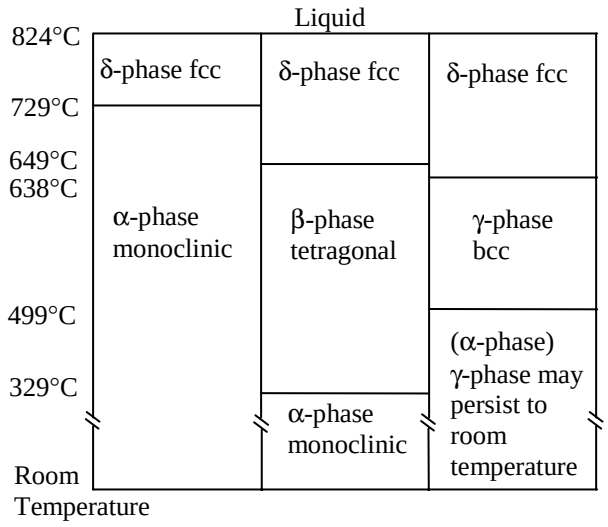

Figure 3.21 Characteristic data and phase transformation temperatures for different phases of Bi_2O_3 while cooling. (From Shuk[70])

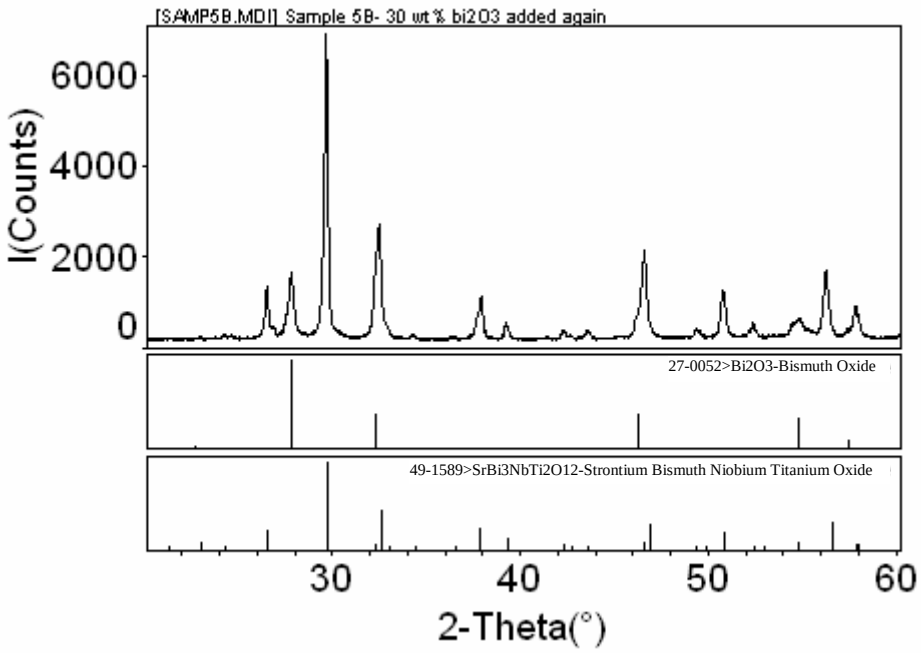

Figure 3.22 XRD pattern of $Bi_2Sr_2Nb_2TiO_{12}$ with 30 weight percent Bi_2O_3 added. PDF #27-52 matches with the Bi_2O_3 peaks, and the current closest PDF #49-1589 for $SrBi_3NbTi_2O_{12}$.

XRD powder diffraction data has suggested that the unknown polymorph is indeed the δ-Bi_2O_3, but Rietveld analysis was done in order to verify the phase of Bi_2O_3 which was present in the $Bi_2Sr_2Nb_2TiO_{12}$ samples. The pattern was measured on the Siemens D-500 X-ray diffractometer from 2°-140° 2θ, 0.02° step, and a 10 second count. The same input cell and atoms positions were used as previously for the $Bi_2Sr_2Nb_2TiO_{12}$ phase. The input cell dimensions for δ-Bi_2O_3 were obtained from the Inorganic Crystal Structure Database[69] (ICSD#2375). The final Rietveld refinement plot of $Bi_2Sr_2Nb_2TiO_{12}$ with 30 weight percent Bi_2O_3 added can be found in Figure 3.23. A weighted residual of 0.14 and a χ^2 of 4.8 was obtained. The refined lattice parameters were as follows for $Bi_2Sr_2Nb_2TiO_{12}$: a=3.8912(1) Å, and c=33.180(1) Å for a body centered tetragonal unit cell and a space group of I4/mmm. The lattice parameters are less than those that were determined previously, but far greater than three standard deviations, so there is a difference. Once again, site mixing of the Bi^{3+} and Sr^{2+} was not taken into consideration.

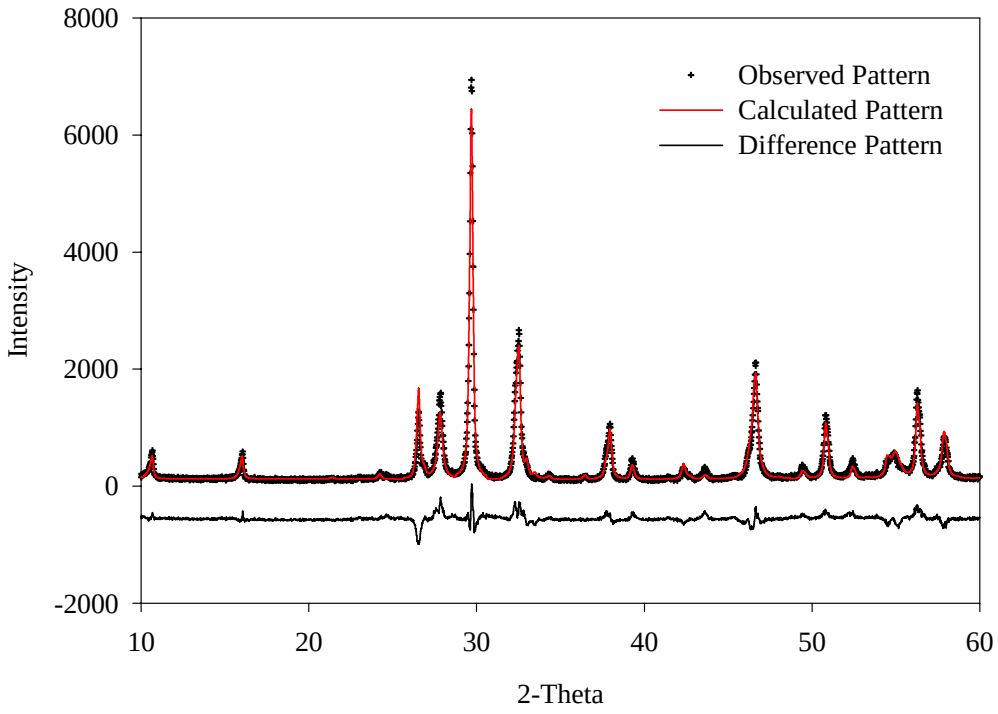

Figure 3.23 Calculated, observed, and difference patterns for $Bi_2Sr_2Nb_2TiO_{12}$ refined with the tetragonal I4/mmm space group and δ-Bi_2O_3 refined with the cubic Fm-3m space group.

The refined lattice parameter for the Bi_2O_3 was: a = 5.5747(4) Å, and the reported value is a = 5.6595(4) Å.[71] Potentially, cations (eg., Sr, Nb, and Ti) could have dissolved into the Bi_2O_3 causing the slight increase in the lattice parameter. The crystal system was cubic with a space group of Fm-3m. Rietveld has the ability to determine the percentage of the different phases. A weight fraction of 0.818(7) was found for $Bi_2Sr_2Nb_2TiO_{12}$, and a Bi_2O_3 weight fraction of 0.181(2). This correlates fairly well with the actual value of 0.3 weight fraction of Bi_2O_2. Some of the Bi_2O_3 was lost during heat treatment, so the resultant weight fractions are reasonable. Peak asymmetry was again a problem, but it modeled better.

This Rietveld analysis shows that the δ-Bi_2O_3 is indeed present within the $Bi_2Sr_2Nb_2TiO_{12}$. Because δ-Bi_2O_3 is not stable at room temperature, the phase is probably a doped Bi_2O_3 system with the fcc δ-Bi_2O_3 form. It is unlikely that the second phase in this sample could be another polymorph of Bi_2O_3 because of the various crystal structures of the multiple polymorphs. Different polymorphs lead to very different XRD

patterns which would not be present in Figure 3.22. Finally, it would be evident from Rietveld analysis if there were significant errors in the second structure.

A DSC was used to try to identify the polymorphs of Bi_2O_3 while cooling. Figure 3.24 displays the resulting pattern. At the melting temperature there is a slight "dip" in the data suggesting that a melt has taken place. While cooling there are a variety of exothermic peaks that cannot be accounted for. The only reasonable explanation is there are sample-pan oxidation effects, or perhaps other material transformations taking place. There appears to be some correlation with the delta to beta phase transition, and the delta to gamma phase transformation, but it isn't satisfactory. The inherent weakness of this experiment was that there was only ~20 mg of Bi_2O_3 present in the sample at best. Furthermore, according to the Rietveld refinement results, there was only 18 weight percent Bi_2O_3 present in the sample meaning only ~14 mg of Bi_2O_3 would be present. Such small amounts of Bi_2O_3 make it nearly impossible to obtain accurate results. Perhaps samples with more Bi_2O_3 would provide more signal, thus more distinct phase transformations.

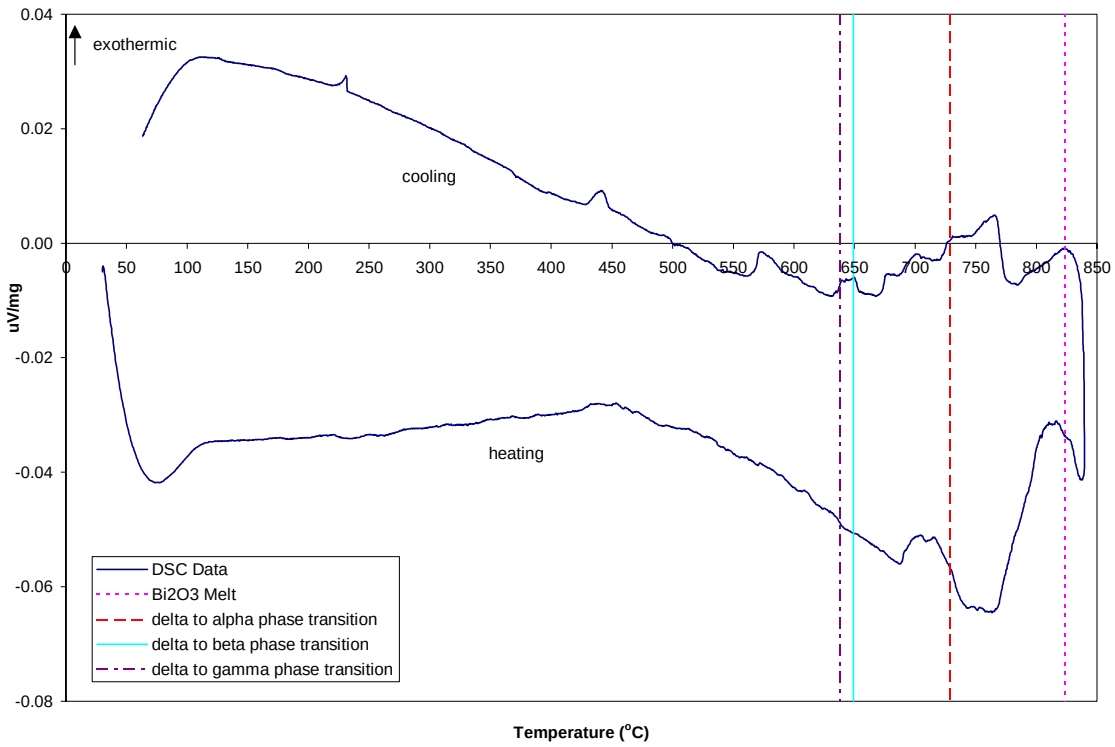

Figure 3.24 DSC results with various Bi_2O_3 phase transformations overlayed to show temperatures of interest.

3.8 Impedance Spectroscopy

Impedance spectroscopy was used to correlate the conductivity of pure $Bi_2Sr_2Nb_2TiO_{12}$ with the $Bi_2Sr_2Nb_2TiO_{12}$ samples that had Bi_2O_3 added to them. Furthermore, grain boundary phenomena were studied in an effort to correlate conductivities with the δ-bismuth oxide phase that had been found with XRD and Rietveld analysis. Cole-Cole plots (Z′ vs. –Z″ on a linear scale) were made at various temperatures so that the conductivity could be calculated. Arcs in Figure 3.25 were similar to the ones found in literature.[35] Most of the samples had one arc on the Cole-Cole plots, but some had multiple arcs denoting the bulk, grain boundary, electrode, or second phases. Examples of multiple arcs are shown in Figure 3.26.

Reading the Cole-Cole plots can be very difficult, and it is usually possible to fit more than one equivalent circuit. For simple, single-arc Cole-Cole plots, the resistance values were taken at the low frequency intercept of the arc and the Z′ axis. The validity of this method was tested using Equivalent Circuit computer software[42], and yielded fits within 2% of tested samples. An example of the equivalent circuit model can be found in Figure 3.27. The resistance values for Cole-Cole plots displaying multiple arcs were read assuming the arcs would mimic Figure 1.8, and can be considered an approximation.

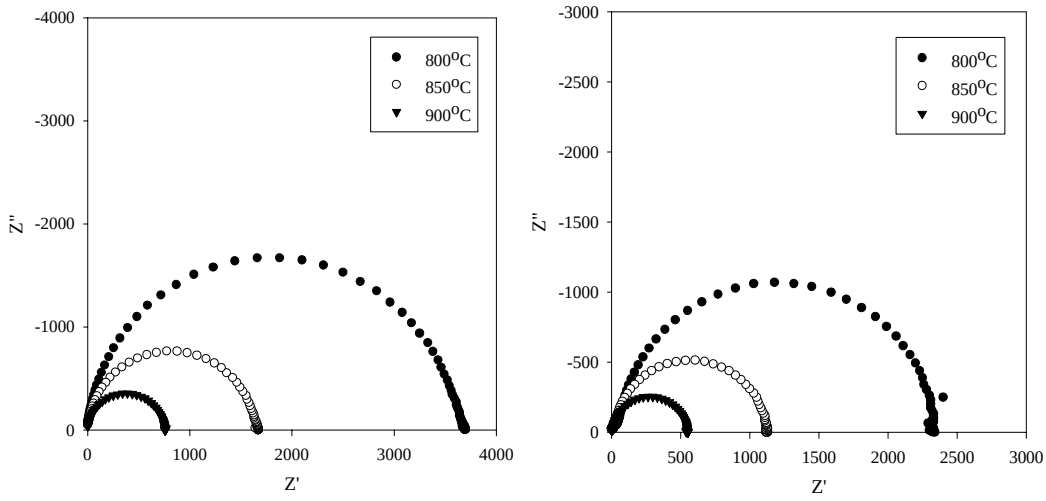

Figure 3.25 Cole-Cole plots for two samples displaying semi-circle arcs at various temperatures. Resistance was read directly from the Z′-axis to find conductivity at said temperatures. (Both samples consist of $Bi_2Sr_2Nb_2TiO_{12}$ and 5 wt.% Bi_2O_3.)

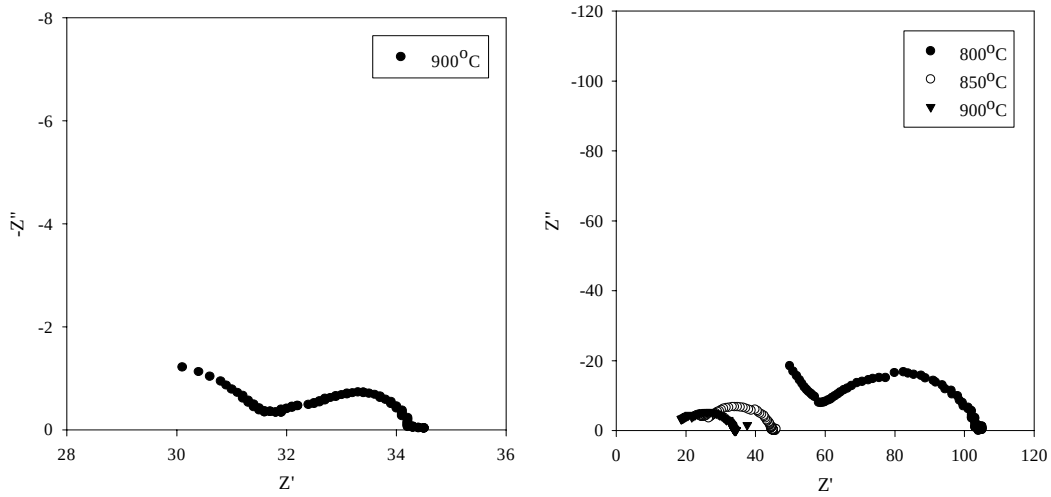

Figure 3.26 Cole-Cole plots of samples displaying multiple arcs. (a) $Bi_2Sr_2Nb_2TiO_{12}$ with 10 wt.% Bi_2O_3 (b) $Bi_2Sr_2Nb_2TiO_{12}$ with 5 wt.% Bi_2O_3.

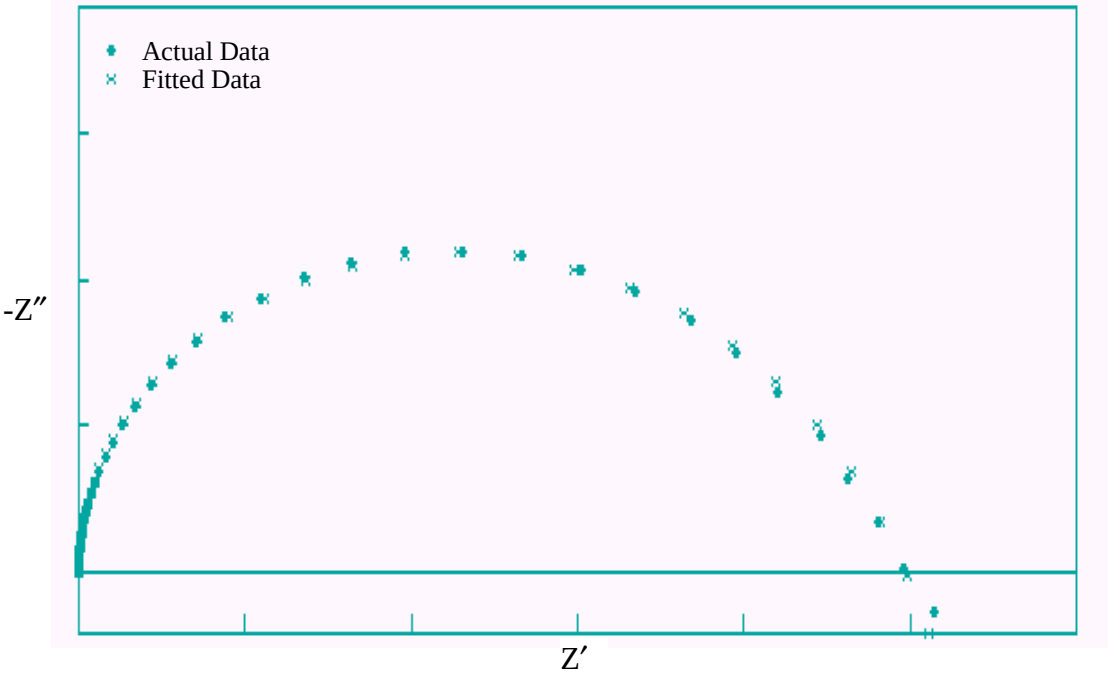

Figure 3.27 Equivalent circuit software model of design experiment 5 at 900°C.

In order to account for differences in the conductivity, the density of the samples needed to be normalized. The density of $Bi_2Sr_2Nb_2TiO_{12}$ was calculated using the lattice parameters found in the initial Rietveld refinement. The samples containing $Bi_2Sr_2Nb_2TiO_{12}$ and Bi_2O_3 were calculated based on the "rule of mixtures" shown in Equation 27. All conductivity values were normalized to the highest density. Experiment 9 had the highest density (94.6 g/cm^3) of all of the samples.

Despite normalizing the conductivity to the density, there were significant differences in the conductivity results. The nature of a designed experimental model is for each of the experiments to have maximum leverage in the design space; therefore repetition of experiments is minimal. Figure 3.28 addresses the conductivity error (one standard deviation) for the only three samples that underwent similar heat treatments. The samples contained the Aurivillius phase with no excess Bi_2O_3 added, and were sintered at 950°C for 10 or 70 hours. The density of the samples that were sintered for 10 hours had a density of 4.0 g/cm^3, while the sample that was sintered for 70 hours had a density of 4.3 g/cm^3. This difference in density did add to the conductivity scatter, but in order to have accurate standard deviation results, at least three experiments were

necessary. The most probable reason for scatter in the conductivity was because the different sintering times did effect the grain size, and hence the conductivity.

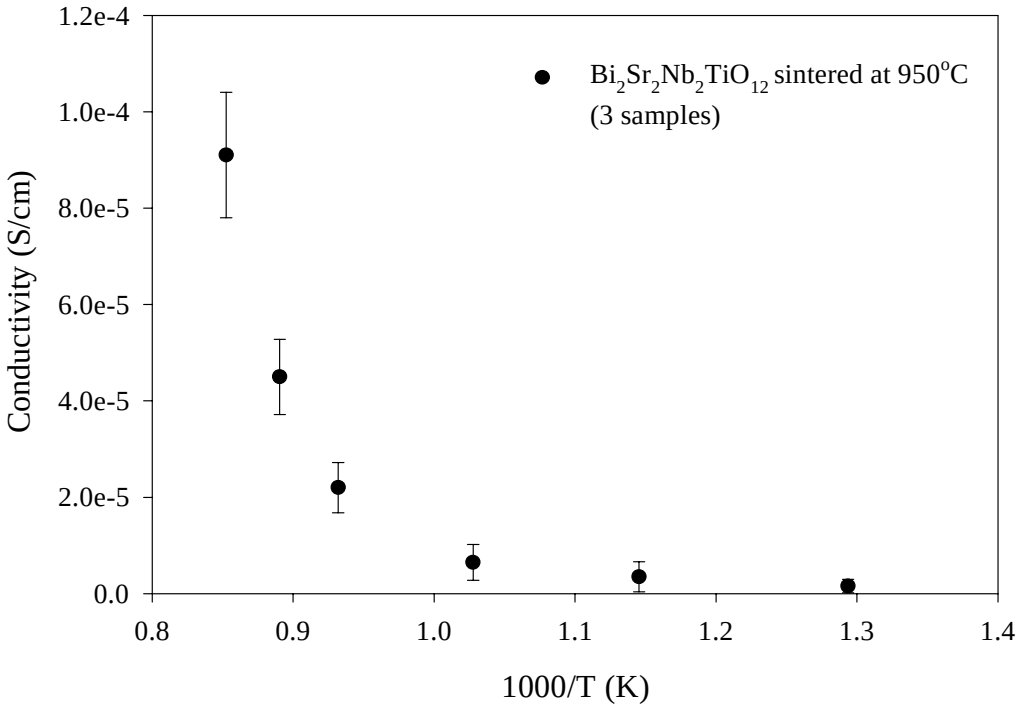

Figure 3.28 Conductivity and standard deviations for the only three samples that underwent similar heat treatments in the design experiment.

One explanation of the larger error was the difference in grain size of the samples due to the difference in sintering times. Another explanation of the large error at higher temperatures was impurities, or concentration changes, at the grain boundaries in the different samples. Such defects lead to considerable effects on the conductivity.[45] Another reason for the larger error at elevated temperatures is that correction files were not accurate. For example, the impedance for one measurement was measured at 900.4°C, while the correction file for 900°C was measured at 918.7°C. The correction files account for changes in resistance that the system undergoes while at elevated temperatures.

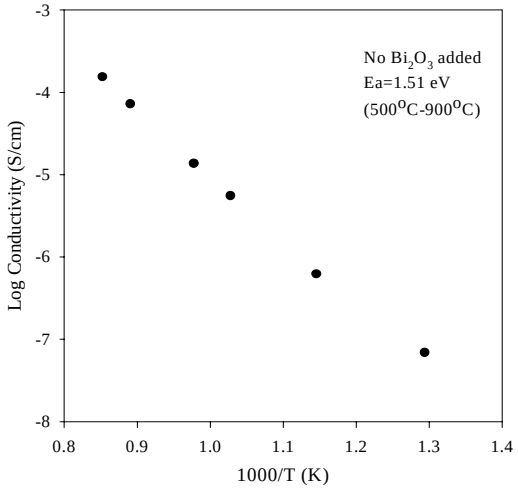
No Bi_2O_3 added
Ea=1.51 eV
(500°C-900°C)
Log Conductivity (S/cm)
1000/T (K)

(a)

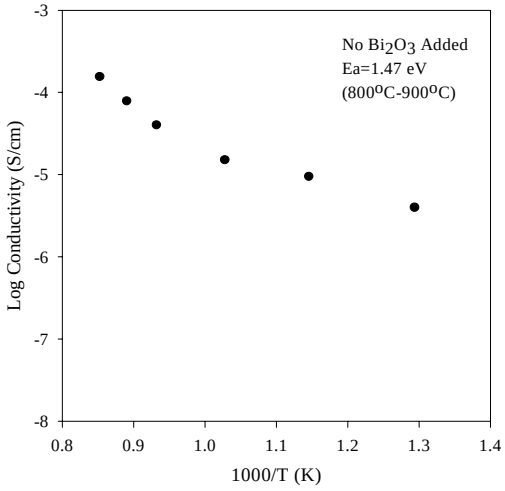
No Bi_2O_3 Added
Ea=1.47 eV
(800°C-900°C)
Log Conductivity (S/cm)
1000/T (K)

(b)

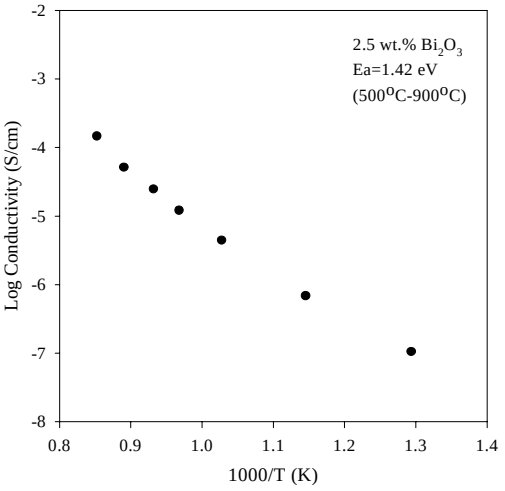
2.5 wt.% Bi_2O_3
Ea=1.42 eV
(500°C-900°C)
Log Conductivity (S/cm)
1000/T (K)

(c)

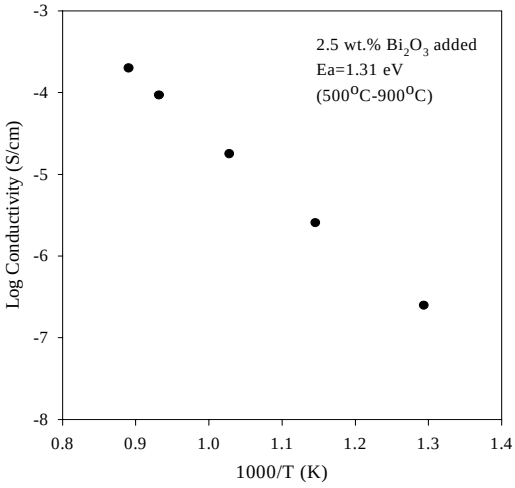
2.5 wt.% Bi_2O_3 added
Ea=1.31 eV
(500°C-900°C)
Log Conductivity (S/cm)
1000/T (K)

(d)

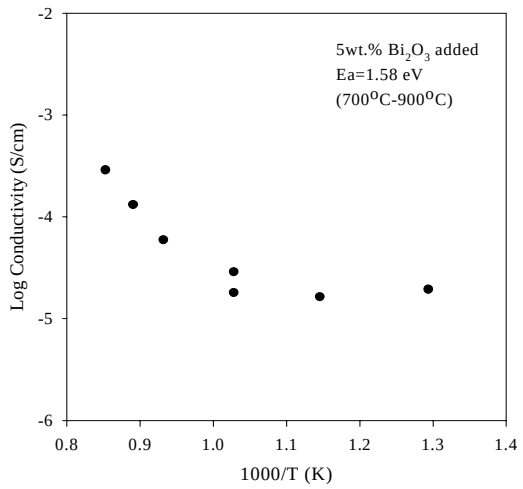

(e)

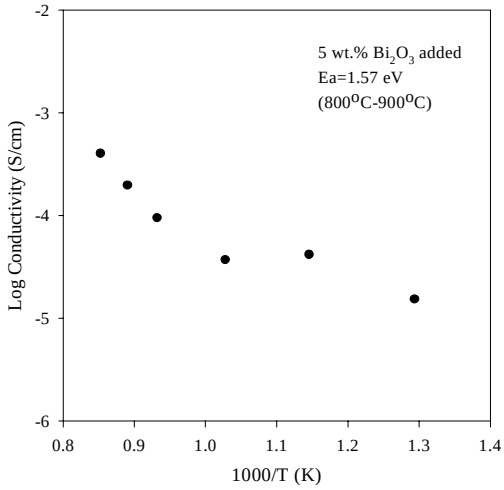

(f)

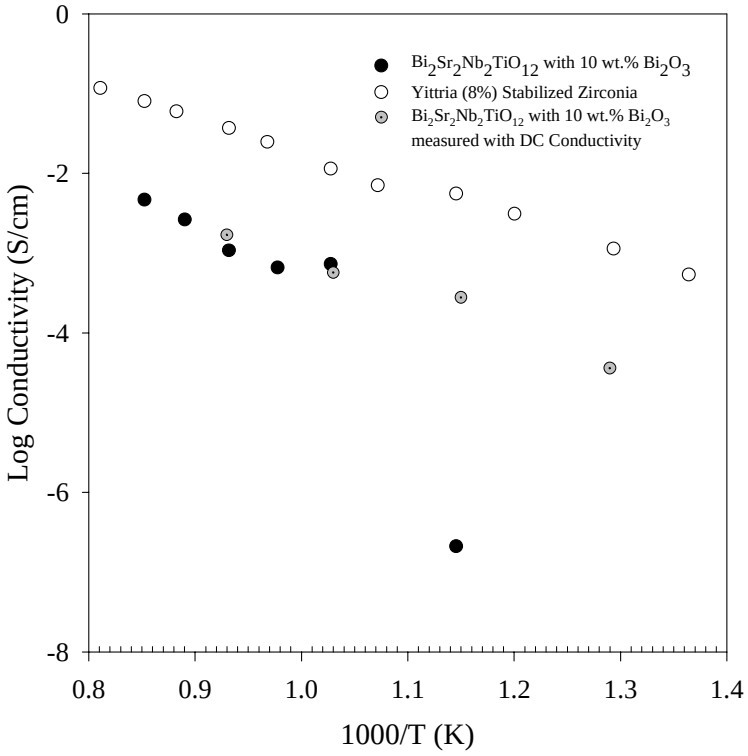

(g)

YSZ (8%)
Ea= 0.83 eV
(500°C-900°C)

$Bi_2Sr_2Nb_2TiO_{12}$
with 10wt.% Bi_2O_3
Ea=0.85 eV
(700°C-900°C)

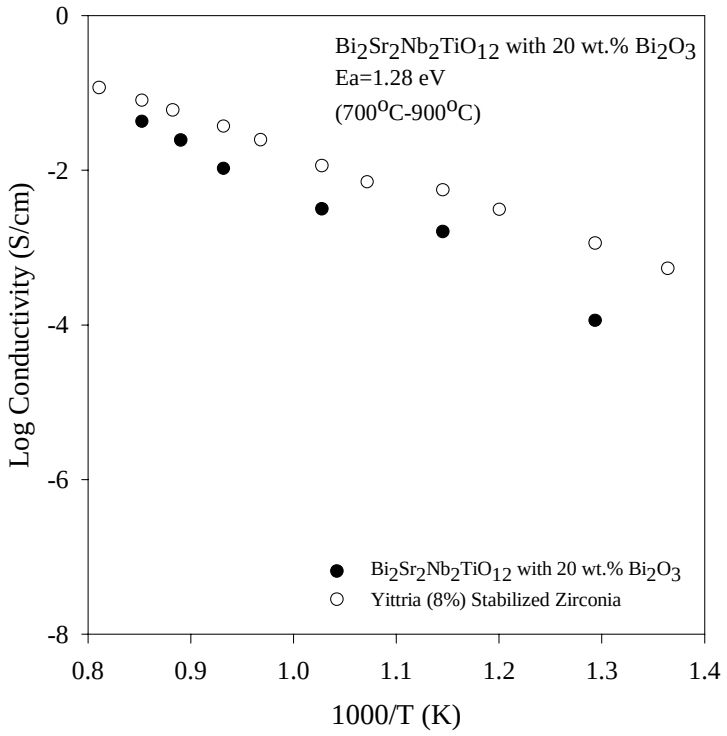

(h)

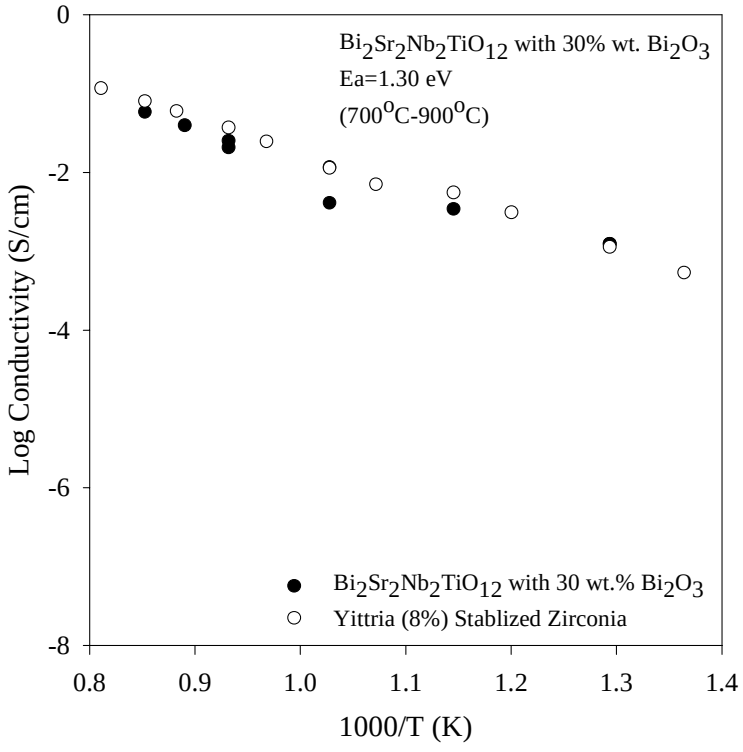

(i)

Figure 3.29 Arrhenius plots of conductivity from AC impedance (a)-(j).

The Arrhenius plots found in Figure 3.29 represent $Bi_2Sr_2Nb_2TiO_{12}$ and samples doped with varying concentrations of Bi_2O_3. The activation energies and temperature ranges are listed on each graph. Samples that consisted of $Bi_2Sr_2Nb_2TiO_{12}$ had E_a values on the order of 1.5 eV when measured at high temperatures. This is a slightly lower activation energy than 1.91 eV found by Kendall and co-workers.[35] The Arrhenius plots for 2.5 weight percent Bi_2O_3 and the Aurivillius phase and pure $Bi_2Sr_2Nb_2TiO_{12}$ were similar. This similarity in conductivities was due to Bi_2O_3 volatilization. The remaining experiments that had more Bi_2O_3 added displayed an overall increase in conductivity depending on the amount of Bi_2O_3. The impedance data for the $Bi_2Sr_2Nb_2TiO_{12}$ with ten weight percent Bi_2O_3 (Figure 3.29 g) suggested a jump in conductivity, but when the conductivity was verified using DC conductivity the jump appeared erroneous. The conductivity of samples containing Bi_2O_3 is less than found in the literature,[72] but this is due to the relatively small amounts of Bi_2O_3 present.

Figure 3.30 shows an Arrhenius plot for $Bi_2Sr_2Nb_2TiO_{12}$ with varying amounts of Bi_2O_3 that underwent similar sintering conditions. The sintering conditions were not identical because the sintering conditions of the experiments that had 10, 20 and 30 weight percent Bi_2O_3 added were based on the ideal from the sintering model (see Figure 3.14). Experiments twelve, two, and five were chosen to reflect the Aurivillius phase, the 2.5 weight percent Bi_2O_3 added, and the five weight percent Bi_2O_3 added respectively (see Table 3-IX). Figure 3.30 proves that the amount of Bi_2O_3 has a direct effect on the conductivity. As the amount of Bi_2O_3 increases, the overall conductivity increases. The IS data suggests the following:

- The addition of 2.5 weight percent Bi_2O_3 does little to influence the conductivity.
- There was an increase in conductivity when Bi_2O_3 was added in amounts greater than five weight percent.

According to the literature,[71-74] δ-Bi_2O_3 does not exist at room temperature, but doped δ-Bi_2O_3 systems do. These doped Bi_2O_3 forms are based on the face centered cubic δ-Bi_2O_3 and show remarkable conductivities.[74] For example, in $(Bi_2O_3)_{1-x}(Y_2O_3)_x$ where x is equal to 0.1 the conductivity values are on the order of 1 S/cm at 700°C.[75] Watanabe found that the δ-Bi_2O_3 phase was only metastable, and was really only a quenched-in phase which slowly converted to a hexagonal phase.[76] Furthermore,

Watanabe showed that the conductivity of the hexagonal phases was approximately one order of magnitude lower than that of the metastable phase.[76] Perhaps this was the reason Say[60] found a decrease in conductivity of $Bi_2Sr_2Nb_2AlO_{11.5}$ with the Bi_2O_3 impurity while thermally cycling. Not only was some of the Bi_2O_3 volatizing, but there might have been a phase change taking place which lowered the conductivity of the sample.

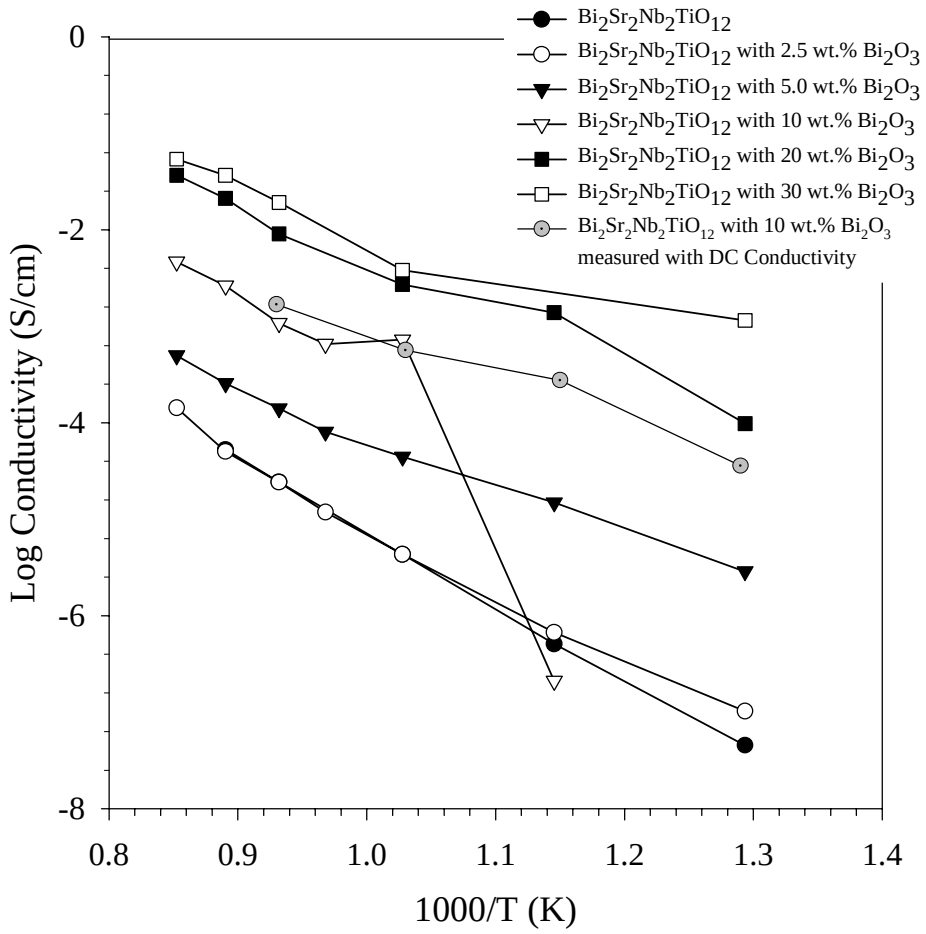

Figure 3.30 Arrhenius plots of conductivity from IS for $Bi_2Sr_2Nb_2TiO_{12}$ with varying amounts of Bi_2O_3 that underwent similar sintering conditions.

Heating and cooling impedance data was collected on a small number of samples to confirm the hysteresis effect. The hysteresis effect has been widely demonstrated in the literature.[60,74,77] The hysteresis effect is a change in transformation temperatures based on heating and cooling of a sample. Because of the number of samples, and large amount of information, the majority of this work focused on the heating of the sample.

3.9 DC Conductivity and RC Circuit check with IS

In order to validate the impedance results a resistor/capacitor (RC) circuit was made and measured with IS. The RC circuit was modeled after Wu *et al*,[41] and consisted of a resistor and a capacitor in parallel representing the grain with a second resistor and capacitor in parallel representing the grain boundary of $SrBi_2Ta2O_9$ at 600°C. It should be noted that the RC circuits were in series with each other. Table 3-X shows the various RC circuit values and the phase they represent. Figure 3.31 shows the Cole-Cole plot of the circuit at room temperature with the equivalent circuit model. The results are nearly identical suggesting that the impedance set-up is accurate (at least at low temperatures).

Table 3-X Values Used for RC Circuit Check of IS Set-up to Mimic $SrBi_2Ta2O_9$ at 600°C

Capacitor of Bulk	Resistor of Bulk	Capacitor of Grain Boundary	Resistor of Grain Boundary
100 pf	6.8 kohm	4.0 nf	2.7 kohm

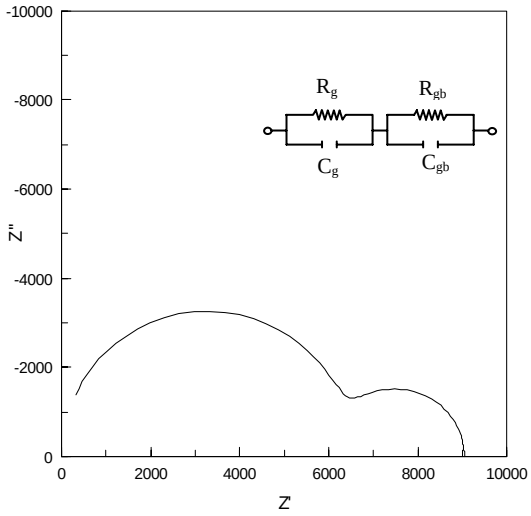

Figure 3.31 Cole-Cole plot of a test circuit representing $SrBi_2Ta2O_9$ at 600°C. The test was done at room temperature with the equivalent circuit model shown.

DC conductivity measurements were made to check and verify the impedance results. A test of the sample of $Bi_2Sr_2Nb_2TiO_{12}$ with 20 weight percent Bi_2O_3 was measured. The results are shown in Figure 32. At low temperatures the results are very similar, but at higher temperatures there is a slight difference, although values are still within the same order of magnitude. A possible explanation for this is a lack of proper correction for the DC conductivity and/or the impedance at elevated temperatures.

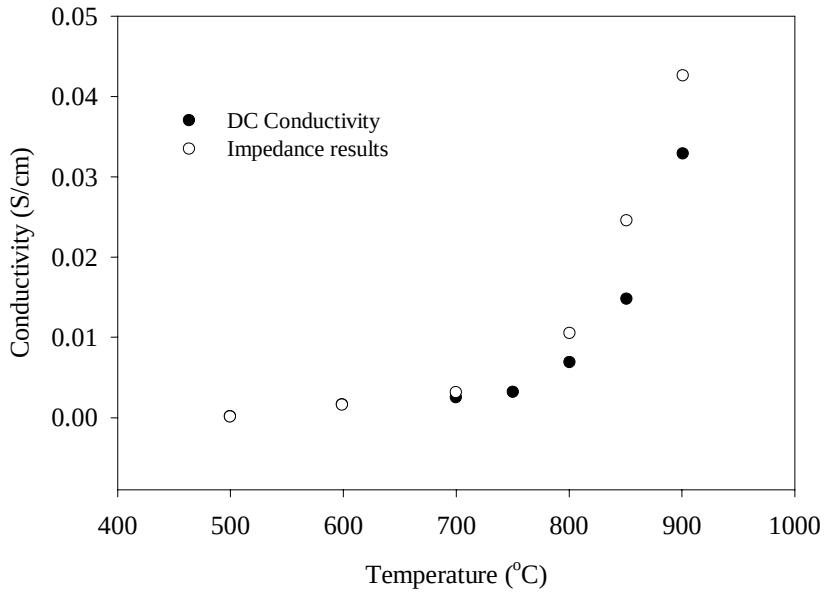

Figure 3.32 Comparison of DC conductivity with conductivity from impedance spectroscopy for a sample of $Bi_2Sr_2Nb_2TiO_{12}$ with 20 weight percent Bi_2O_3.

4. Summary and Conclusions

The Aurivillius phase $Bi_2Sr_2Nb_2TiO_{12}$ has been successfully synthesized by solid-state synthesis. The precursor powders were characterized to ensure that adequate mixing was taking place throughout the solid-state synthesis reactions. Each individual synthesis step was characterized by XRD to monitor phase evolution and map phase formation. Phase pure samples were investigated with SEM to study microstructure. XRD measurements were made for phase identification and crystal structure information. Rietveld refinement was utilized to characterize the Aurivillius unit cell, and to model four-layer Aurivillius impurities. A weighted residual of 0.14 and a χ^2 of 4.5 was obtained. The refined lattice parameters were a=3.8927(7) Å, and c=33.1960(9) Å for a body centered tetragonal unit cell a tetragonal I4/mmm space group.

A statistical design experiment was done in order to determine if the sintered density of $Bi_2Sr_2Nb_2TiO_{12}$ was affected by: (1) sintering temperature, (2) duration of sintering, and (3) the addition of Bi_2O_3 as a sintering accelerator. The results of the experiment were quantified into a design space that had an R^2 of 0.93 and a $S_{y.x}$ of 0.33. Time did not statistically have an impact on the sintering of $Bi_2Sr_2Nb_2TiO_{12}$ within the confines of the design space, but sintering temperature and the addition of Bi_2O_3 as a sintering accelerator did. Conductivity of the samples varied, but this was most likely due to differential grain sizes induced from the different sintering durations. The model suggests that for $Bi_2Sr_2Nb_2TiO_{12}$ an optimum sintering temperature was ~1060°C with approximately four weight percent Bi_2O_3 added.

High temperature XRD was used to provide in-situ measurements. The evolution of $Bi_2Sr_2Nb_2TiO_{12}$ from the precursor powders was monitored in-situ to understand the formation mechanisms. Phase pure $Bi_2Sr_2Nb_2TiO_{12}$ was not formed with the in-situ HTXRD experiment, rather a combination of $SrTiO_3$ with two, three, and four-layer Aurivillius phases formed.

The microstructures of the samples from the statistical design experiment were studied using the SEM. Qualitative phase information was measured using EDS. The samples that had large amounts of Bi_2O_3 added showed large amounts of Bi_2O_3 at the grain boundaries. Rietveld refinement was done for $Bi_2Sr_2Nb_2TiO_{12}$ with 30 weight

percent Bi_2O_3 in an effort to find which polymorph of Bi_2O_3 was present. The δ-Bi_2O_3 structure was used. A weighted residual of 0.14 and a χ^2 of 4.8 was obtained suggesting an accurate refinement.

The conductivities of the samples at various temperatures were measured using impedance spectroscopy and DC conductivity. The densities of the samples needed to be taken into account to reliably calculate the conductivities. They were normalized to 95 percent theoretical density. Theoretical density was calculated via lattice parameters for single phase samples, and with the rule of mixtures for multi-phase samples. Arrhenius plots of conductivity were made of the various samples and activation energies were calculated. The activation energies for pure $Bi_2Sr_2Nb_2TiO_{12}$ were approximately 1.5 eV, whereas the literature value was 1.9 eV.[35]

The addition of Bi_2O_3 greatly enhanced the conductivity values of the $Bi_2Sr_2Nb_2TiO_{12}$ to the magnitude of the current ionic conductor standard, yittria stabilized zirconia. DC conductivity was used to check the validity of the IS, and the results were satisfactory. The $Bi_2Sr_2Nb_2TiO_{12}$ IS data suggests the following: (1) the addition of 2.5 weight percent Bi_2O_3 did not change the conductivity, (2) amounts greater than five weight percent Bi_2O_3 increased conductivity.

5. Further Work

Relating the structure at the atomic level to material properties is a crucial link in understanding the capabilities as well as the deficiencies of the Aurivillius phase as a potential material for solid oxide fuel cell electrolytes. Thermal cycling of the samples should be performed to determine if the δ-Bi_2O_3 is stable within the Aurivillius phase. It is anticipated that throughout thermal cycling the amount of Bi_2O_3 will gradually decrease (Figure 5.1). This decrease will be because of two reasons: (1) the δ-Bi_2O_3 will change from the face-centered-cubic form to hexagonal form causing a decrease in conductivity, and (2) the gradual volatilization of Bi_2O_3 will remove the primary conducting phase causing a decrease in conductivity. In Figure 5.1, the initial decrease in conductivity is due to the crystal structure change of Bi_2O_3. As the sample goes through the thermal cycles to 900°C Bi_2O_3 is gradually lost by volatilization. Approximately one weight percent Bi_2O_3 will volatize after each cycle. The loss will continue until all of the Bi_2O_3 has volatized. The final conductivity will be approximately $1*10^{-4}$ S/cm at 900°C.

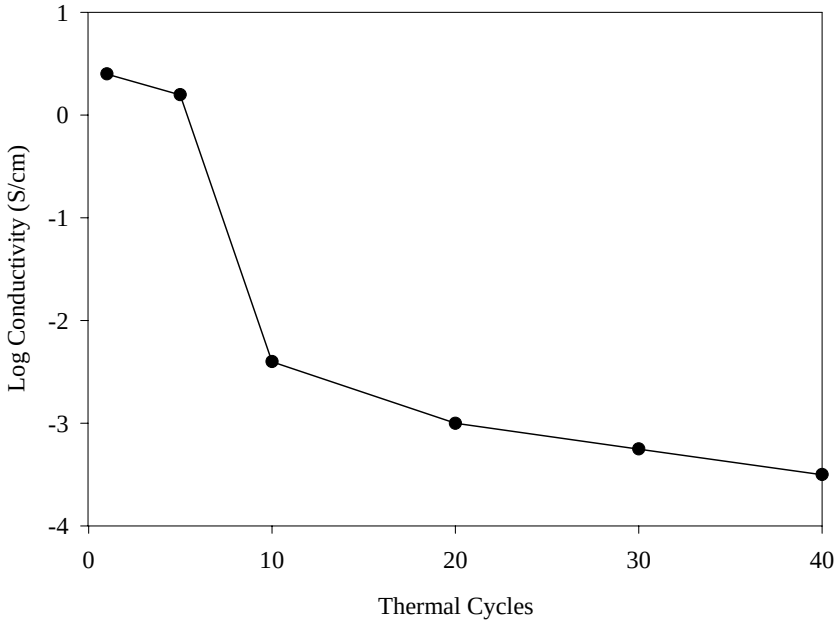

Figure 5.1 Proposed thermal cycling conductivity changes of $Bi_2Sr_2Nb_2TiO_{12}$ with 30 weight percent Bi_2O_3 added at 900°C.

Throughout this research Bi_2O_3 was added to $Bi_2Sr_2Nb_2TiO_{12}$, but more experiments should be done to find the critical amount of Bi_2O_3 to maximize

conductivity. Figure 5.2 displays the proposed conductivities of $Bi_2Sr_2Nb_2TiO_{12}$ with 50 weight percent Bi_2O_3 added compared to the data found in this research.

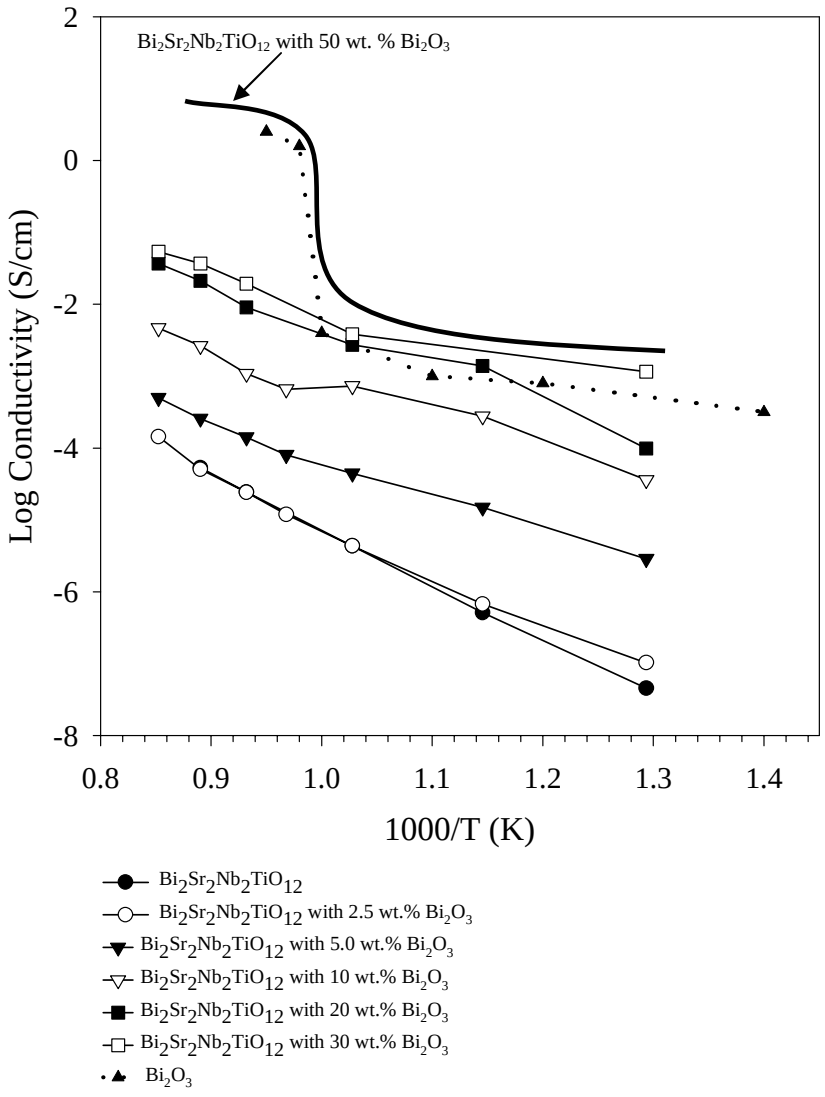

Figure 5.2 Proposed conductivities of $Bi_2Sr_2Nb_2TiO_{12}$ with varying amounts of Bi_2O_3 added (solid line). Lines with points are actual data from IS and DC conductivity. (Bi_2O_3 data from Takahashi[78])

There are other areas in this research that deserve further investigation to more thoroughly explore and confirm the findings thus far. Branches of this study that may pose particular interest are the following:

- Remake $Bi_2Sr_2Nb_2TiO_{12}$ in areas of the sintering statistical design space where little data had been collected. Confirm model's accuracy and/or adjust.
- Re-run IS experiments with new correction files, especially those at 500°C-700°C, such that "proper" correction may be done.
- Transmission electron microscopy to further investigate the δ-Bi_2O_3 phase throughout $Bi_2Sr_2Nb_2TiO_{12}$.
- Confirm the novel new synthesis route of forming $Bi_2Sr_2Nb_2TiO_{12}$ with $Bi_2SrNb_2O_9$.
- Investigate low temperature reactions (<800°C) of precursor powders with HTXRD.
- Try using gold electrodes instead of platinum electrodes in conductivity experiments to isolate electronic conductivity.
- Measure more samples with excess Bi_2O_3 in an effort to correlate grain boundary conductivity with δ-Bi_2O_3.

References

1. B.C.J. Steele, "Materials for Electrochemical Conversion and Storage Systems," *Ceram. Int.,* **19** [4] 269-77 (1993).

2. N.Q. Minh, "Ceramic Fuel Cells," *J. Am. Ceram. Soc.*, **76** [3] 563-88 (1993).

3. S.C. Singhal, "Advances in Solid Oxide Fuel Cell Technology," *Solid State Ionics,* **135** [1-4] 305-13 (2000).

4. W.R. Grove, "On Voltaic Series and the Combination of Gases by Platinum," *Philos. Mag.,* **14** [1] 127-30 (1839).

5. W. Nernst, "Uber die Elektrolytische Leitung Fester Korper bei Sehr Hohen Temperaturen," *Z. Elektrochem.*, **6** 41-3 (1899).

6. E. Baur and H. Preis, "Uber die Brennstoff-Ketten mit Festleitern," *Z. Electrochem.*, **43** 727-32 (1937).

7. *Science and Technology of Fast Ion Conductors;* pp. 23-50. Edited by H.L. Tuller and M. Balkanski. Plenum Press, New York, 1987.

8. K.R. Kendall, C. Navas, J.K. Thomas, and H.-C. zur Loye, "Recent Developments in Oxide Ion Conductors: Aurivillius Phases," *Chem. Mater.*, **8** [3] 642-9 (1996).

9. J.L. Silveira, E.M. Leal, and L.F. Ragonha, Jr., "Analysis of a Molten Carbonate Fuel Cell: Cogeneration to Produce Electricity and Cold Water," *Energy (Oxford, U.K.),* **26** [10] 891-904 (2001).

10. M. Lain, "Membrane Fuel Cells Provide a Breath of Fresh Air," *Membr. Technol.,* **1997** [87] 7-10 (1997).

11. R. Doshi, V.L. Richards, J.D. Carter, X. Wang, and M. Krumpelt, "Development of Solid-oxide Fuel Cells That Operate at 500°C," *J. Electrochem. Soc.*, **146** [4] 1273-8 (1999).

12. J.B. Goodenough, "Ceramic Solid Electrolytes," *Solid State Ionics,* **94** [1-4] 17-25 (1997).

13. B. Aurivillius, "Mixed Bismuth Oxides with Layer Lattices: I. The Structure Type of $CaNb_2Bi_2O_9$," *Ark. Kemi,* **1** [54] 463-80 (1949).

14. B. Aurivillius, "Mixed Bismuth Oxides with Layer Lattices: II. Structure of $Bi_4Ti_3O_{12}$," *Ark. Kemi,* **1** [58] 499-512 (1949).

15. B. Aurivillius, "Mixed Oxides with Layer Lattices: III. Structure of $BaBi_4Ti_4O_{15}$," *Ark. Kemi,* **2** [37] 519 (1950).

16. Y. Shi, S. Feng, and C. Cao, "Hydrothermal Synthesis and Characterization of Bi_2MoO_6 and Bi_2WO_6," *Mater. Lett.,* **44** [3] 215-8 (2000).

17. T. Rentschler, "Substitution of Lead into the Bismuth Oxide Layers of the N=2 and N=3 Aurivillius Phases," *Mater. Res. Bull.,* **32** [3] 351-69 (1997).

18. R.E. Melgarejo, M.S. Tomar, P.S. Dobal, S.K. Flippov, R.S. Katiyar, and K.A. Kuenhold, "{1-x $SrBi_2Ta_2O_{9-x}Bi_3TiTaO_9$} Materials: Structural Behavior and Ferroelectric Response," *Mater. Sci. Eng.,* **B83** [1-3] 89-96 (2001).

19. J. Maier, "Remarks on Application of Fast Ion Conductors," pp. 299-301 in NATO ASI Series, Vol. 199, *Science and Technology of Fast Ion Conductors.* Edited by H.L. Tuller and M. Balkanski. Plenum Press, New York, 1989.

20. H.D. Megaw, *Crystal Structures: A Working Approach;* pp. 217-21. W.B. Saunders, Philadelphia, 1973.

21. S.T. Misture. "Oxygen Ion Conduction in Layered Aurivillius-Derived Ceramics," National Science Foundation Career Grant, Alfred University, Alfred, NY, 1998.

22. J.B. Goodenough, J.E. Ruiz-Diaz, and Y.S. Zhen, "Oxide-Ion Conduction in $Ba_2In_2O_5$ and $Ba_3In_2MO_8$ (M= Ce, Hf, Zr)," *Solid State Ionics,* **44** [1-2] 21-31 (1990).

23. F. Krok, W. Bogusz, P. Kurek, M. Wasiucionek, W. Jakubowski, and J. Dygas, "Influence of Preparation Procedure on Some Physical Properties of BICUVOX," *Mater. Sci. Eng.,* **B21** [1] 70-6 (1993).

24. M.P. Pechini, "Method of Preparing Lead and Alkaline Earth Titanates and Niobates and Coating Method Using the Same to Form a Capacitor," US Pat. 3,330,697, July 11, 1967.

25. O. Schulz and M. Martin, "Preparation and Characterization of $La_{1-x}Sr_xGa_{1-y}Mg_yO_{3-(x+y)/2}$ for the Investigation of Cation Diffusion Processes," *Solid State Ionics,* **135** [1-4] 549-55 (2000).

26. C.P. Udawatte, M. Kakihana, and M. Yoshimura, "Low Temperature Synthesis of Pure $SrSnO_3$ and the $(Ba_xSr_{1-x})SnO_3$ Solid Solution by the Polymerized Complex Method," *Solid State Ionics,* **128** [1-4] 217-26 (2000).

27. W. Wong-Ng, J.A. Kaduk, Q. Huang, and R.S. Roth, "Crystal Structure of the Monoclinic Pervskite $Sr_{3.94}Ca_{1.31}Bi_{2.70}O_{12}$," *Powder Diffr.,* **15** [4] 227-33 (2000).

28. H. Bachhofer, H.v. Philipsborn, W. Hartner, C. Dehm, B. Jobst, A. Kiendl, H. Schroeder, and R. Waser, "Phase Formation and Crystal Growth of Sr-Bi-Ta-O Thin Films Grown by Metalorganic Chemical Vapor Deposition," *J. Mater. Res.,* **16** [10] 2966-73 (2001).

29. T. Kudo and K. Fueki, *Solid State Ionics;* pp. 67-77. VCH, New York, 1990.

30. O. Joubert, A. Jouanneaux, M. Ganne, R.N. Vannier, and G. Mairesse, "Solid Phase Synthesis and Characterization of a New BIMEVOX Series:$Bi_4V_{2-x}M_xO_{11}$ (M=Sbv, Nbv)," *Solid State Ionics,* **73** [3-4] 309-18 (1994).

31. H.S. Shulman, M. Testorf, D. Damjanovic, and N. Setter, "Microstructure, Electrical Conductivity, and Piezoelectric Properites of Bismuth Titanate," *J. Am. Ceram. Soc.,* **79** [12] 3124-8 (1996).

32. R.A. Armstrong and R.E. Newnham, "Bismuth Titanate Solid Solutions," *Mater. Res. Bull.,* **7** [10] 1025-34 (1972).

33. R.E. Newnham, R.W. Wolfe, R.S. Horsey, F.A. Diaz-Colon, and M.I. Kay, "Crystal Structure of (Sr,Ba)$Bi_2Ta_2O_9$," *Mater. Res. Bull.,* **8** [10] 1183-96 (1973).

34. J.B. Goodenough, A. Manthiram, P. Paranthaman, and Y.S. Zhen, "Fast Oxide-Ion Conduction in Intergrowth Structures," *Solid State Ionics,* **52** [1-3] 105-9 (1992).

35. K.R. Kendall, J.K. Thomas, and H.-C. zur Loye, "Synthesis and Ionic Conductivity of a New Series of Modified Aurivillius Phases," *Chem. Mater.,* **7** [1] 50-7 (1995).

36. J.R. Macdonald and W.B. Johnson, "Fundamentals of Impedance Spectroscopy," pp. 1-35 in *Impedance Spectroscopy: Emphasizing Solid Materials and Systems.* Edited by J.R. Macdonald. John Wiley & Sons, New York, 1987.

37. A. Hinton, Introduction to Impedance Spectroscopy, Solartron, Farnborough Hampshire, UK, 1997.

38. D.D. Edwards, J.H. Hwang, S.J. Ford, and T.O. Mason, "Experimental Limitations in Impedance Spectroscopy: Part V Apparatus Contributions and Corrections," *Solid State Ionics,* **99** [1-2] 85-93 (1997).

39. A.R. West, D.C. Sinclair, and N. Hirose, "Characterization of Electrical Materials, Especially Ferroelectrics, by Impedance Spectroscopy," *J. Electroceram.*, **1** [1] 65-71 (1997).

40. D.C. Sinclair and A.R. West, "Impedance and Modulus Spectroscopy of Semiconducting $BaTiO_3$ Postive Temperature Coefficient of Resistance," *J. Appl. Phys.*, **66** [8] 3850-6 (1989).

41. Y. Wu, M.J. Forbess, S. Seraji, S.J. Limmer, and T.P. Chou, "Impedance Study of $SrBi_2Ta_2O_9$ and $SrBi_2(Ta_{0.9}V_{0.1})_2O_9$ Ferroelectrics," *Mater. Sci. Eng.*, **B86** [1] 70-8 (2001).

42. B.A. Boukamp, EQUIVCRT.PAS [Computer Program] University of Twente, Enschede, Netherlands, 1988.

43. A.R. West, *Solid State Chemistry and Its Applications;* pp. 481-2. John Wiley & Sons, New York, 1984.

44. M.S. Peterson, C.A. Say, S.A. Speakman, and S.T. Misture, "High Temperature X-ray Diffraction Study of Reaction Rates of Ceramics," *Advances in X-ray Analysis,* (to be published).

45. W.D. Kingery, H.K. Bowen, and D.R. Uhlmann, *Introduction to Ceramics*, 2nd ed.; p. 448. John Wiley & Sons, New York, 1976.

46. M.N. Rahaman, *Ceramic Processing and Sintering;* pp. 19-25. Marcel Dekker, New York, 1995.

47. J.S. Reed, *Principles of Ceramic Processing*, 2nd ed.; pp. 594-606. John Wiley & Sons, New York, 1995.

48. A. Lisinska-Czekaj, D. Czekaj, M.J.M. Gomes, and M.F. Kuprianov, "Investigations on the Synthesis of Bi_3NbTiO_9 Ceramics," *J. Eur. Ceram. Soc.*, **19** [6-7] 969-72 (1999).

49. C.-H. Lu and Y.-C. Chen, "Sintering and Decomposition of Ferroelectric Layer Perovskites: Strontium Bismuth Tantalate Ceramics," *J. Eur. Ceram. Soc.*, **19** [16] 2909-15 (1999).

50. C.D. Hendrix, "What Every Technologist Should Know About Experimental Design," *CHEMTECH,* **9** [3] 167-74 (1979).

51. D.C. Montgomery, *Design and Analysis of Experiments*, 5th ed.; p. 684. John Wiley & Sons, New York, 1997.

52. IUCr Monographs on Crystallography, Vol. 5, *The Rietveld Method*; pp.1-2. Edited by R.A. Young. Oxford Science Publications, Oxford, England, 1993.

53. L.B. McCusker, R.B.V. Dreele, D.E. Cox, D. Lauer, and P. Scardi, "Rietveld Refinement Guidelines," *J. Appl. Cryst.*, **32** [1] 36-50 (1999).

54. S.T. Misture, "Rietveld Analysis," Short Course Handout, Alfred University, Alfred, NY, 2002.

55. R. Jenkins and R.L. Snyder, Chemical Analysis: A Series of Monographs on Analytical Chemistry and Its Applications, Vol. 138, *Introduction to X-ray Powder Diffractometry*; p. 382. John Wiley & Sons, New York, 1996.

56. *CRC Handbook of Chemistry and Physics*, 76th ed.*;* pp. **4**-45. Editor D.R. Lide. CRC Press, New York, 1995-1996.

57. A.C. Larson and R.B.V. Dreele, GSAS: General Structure Analysis System [Computer Program] Los Alamos National Laboratory, Los Alamos, NM, 1985-2000.

58. JADE 6 [Computer Program] Materials Data, Livermore, CA, 2002.

59. D. A. Earl, CES 434 Class Notes, Alfred University, Alfred, NY, Fall, 2000.

60. C.A. Say, "Electrical and Compositional Study of N=3 Aurivillius Structures for Oxygen Conducting Devices"; M. S. Thesis, Alfred University, Alfred, NY, 2002.

61. "Standard Test Methods for Apparent Porosity, Water Absorption, Apparent Specific Gravity, and Bulk Density of Burned Refractory Brick and Shapes by Boiling Water," ASTM Standard C 20-97. Annual Book of ASTM Standards, Vol. 15.01. American Society for Testing and Materials, West Conshohocken, PA, 2000

62. A. Laarif and F. Theobald, "The Lone Pair Concept and the Conductivity of Bismuth Oxides Bi_2O_3," *Solid State Ionics,* **21** [45] 183-93 (1986).

63. D.A. Skoog, F.J. Holler, and T.A. Nieman, *Principles of Instrumental Analysis*, 5th ed.; p. 805. Saunders College Publishing, Chicago, 1998.

64. W.D. Callister, *Materials Science and Engineering: An Introduction*, 4rth ed.; pp. 382-3. John Wiley & Sons, New York, 1997.

65. F. Williams, Z-Meter [Computer Program] Alfred University, Alfred, NY, 2001.

66. K.S. Cole and R.H. Cole, "Dispersion and Absorption in Dielectrics: I. Alternating Current Characteristics," *J. Chem. Phys.,* **9 [4]** 341-51 (1941).

67. S.A. Speakman, "The Crystal Chemistry of Brownmillerite and N=3 Aurivillius Type Ceramic Conductors for Fuel Cell Applications"; Ph.D. Thesis, Alfred University, Alfred, NY, 2002.

68. M.S. Haluska, "Crystal Structure Refinements of the Three-Layer Aurivillius Ceramics $Bi_2Sr_{2-x}A_xNb_2TiO_{12}$ (A = Ca, Ba, x = 0.5, 1) Using Combined X-ray and Neutron Powder Diffraction," (to be published).

69. FINDIT- Inorganic Crystal Structure Database [Computer Program] Fachinformationszentrum, Karlsruhe, Germany, 2002 .

70. P. Shuk, H.-D. Wiemhofer, U. Guth, W. Gopel, and M. Greenblatt, "Oxide Ion Conducting Electrolytes Based on Bi_2O_3," *Solid State Ionics,* **89** [3-4] 179-96 (1996).

71. H.A. Harwig, "On the Structure of Bismuthsesquioxide: The α, β, γ, and δ Phase," *Z. Anorg. Allg. Chem.,* **444** 151-66 (1978).

72. H.A. Harwig and A.G. Gerards, "Electrical Properties of the α,β,γ, and δ Phases of Bismuth Sesquioxide," *J. Solid State Chem.,* **26** [47] 265-74 (1978).

73. H.A. Harwig and A.G. Gerards, "The Polymorphism of Bismuth Sesquioxide," *Thermochim. Acta.,* **28** [1] 121-31 (1979).

74. N.M. Sammes, G.A. Tompsett, H. Nafe, and F. Aldinger, "Bismuth Based Oxide Electrolytes - Structure and Ionic Conductivity," *J. Eur. Ceram. Soc.,* **19** [10] 1801-26 (1999).

75. T. Takahashi, H. Iwahara, and T. Arao, "High Oxide Ion Conducting in Sintered Oxides of the System Bismuth (III) Oxide-Yttrium Oxide," *J. Appl. Electrochem.,* **5** [3] 187-95 (1975).

76. A. Watanabe, "Is It Possible to Stablize δ-Bi_2O_3 by an Oxide Additive?," *Solid State Ionics,* **40/41** [2] 889-92 (1990).

77. V.B. Modi, "Electrical and Microstructural Characterization of N=3 Type Aurivillius Phases"; M.S. Thesis, Alfred University, Alfred, NY, 2002.

78. T. Takahashi and H. Iwahara, "Oxide Ion Conductors Based on Bismuth Sesquioxide," *Mater. Res. Bull.,* **13** [10] 1447-53 (1978).